

Copper-based Nanostructured Catalysts for Efficient and Selective CO₂ Electroreduction – Synthesis, Catalytic Performance, and Mechanistic Analysis

Vorgelegt von
MSc. Chem. Xingli Wang
ORCID: 0000-0003-2785-9707

an der Fakultät II-Mathematik und Naturwissenschaften
der Technischen Universität Berlin
zur Erlangen des akademischen Grades

Doktorin der Naturwissenschaften
-Dr. rer. nat.

genehmigte Dissertation

Promotionsausschuss:
Vorsitzende: Prof. Dr. Maria Andrea Mroginski
Gutachter: Dr. Frédéric Jaouen (Université de Montpellier)
Gutachter: Prof. Dr. Peter Strasser

Tag der wissenschaftlichen Aussprache: 05. Juni. 2019
Berlin 2020

Acknowledgement

First and foremost, I would like to thank my supervisor, Prof. Dr. Peter Strasser, for offering me the opportunity to work in his group. I appreciate all his contributions of time, ideas to make my Ph.D. study successful.

I also would like to thank Dr. Frédéric Jaouen and Prof. Dr. Maria Andrea Mroginski, the committee of my defense, for the insightful feedback and valuable advice.

It would not have been possible to graduate without the support and guidance that I received from many people. I would like to deliver my sincere thank to Dr. Ana Sofia Varela, who supported and guided me in the beginning of my Ph.D. I am greatly thankful to our CO₂ team, Wen, Tim, Jorge, Cheonghee, Lujin, Yulin, and Trung. My research would have been impossible without the aid and support of you. I would like to thank Jorge for the grate collaboration in DEMS and teaching me how to read/analyze the data, which are one of the most complicated data I have ever processed. Heartfelt thanks go to our *in situ* TEM team, Stefanie and Malte, for every failure and success we got during the experiments. I would like to express my deep gratitude to Henrik, Fabio, Elisabeth, Thomas, Malte, Dr. Isaac Martens (ESRF) and Dr. Jakub Drnec (ESRF) for their kind help with beam time, data processing and useful discussions. I am profoundly grateful to Dr. Katharina Klingan, Shan Jiang and Prof. Holger Dau for the helpful discussions and collaboration in *operando* XAS and *in situ* Raman experiments. I would like to thank Dipl. Ing. Sören Selve, Dr. Ing. Dirk Berger, Dipl. Ing. Ulrich Gernert, Dr. Tore Niermann, Jan from ZELMI and Dr. Marc Heggen from Forschungszentrum Jülich, for their great help and support for microscopy and all discussions. Many thanks to Vera, Camillo, Manuel, Mikaela for their kind help in both scientific work and daily life.

I would like to thank every college of mine in Strasser's group, for the stimulating discussions, for every enjoyable moment we were working together, and for all the fun we have had in the last four years.

Further, I would also like to thank Mrs. Annette Wittebrock and Benjamin Paul for ordering chemicals and lab wares, Benjamin Paul for taking care of SEM, Mrs. Astrid Müller-Klauke for measuring ICP-OES and Mrs. Kluge for managing the gas bottles.

I am also very grateful to all of my BIG-NSE friends Huan Sun, Yanyan, Fang, Shuang, Chengyue, Xiaojia, Weichao, Yuwen, Huan Wang, and Yu Peng.

I especially thank my mom, dad, my grandpa, grandma, and my sister. I would not have made it this far without them. I know I always have my family to count on when times are rough.

I would also like to say a heartfelt thank to my beloved husband, Yu, for passing through many fine times together with me in Germany. He has been a true and great supporter and has unconditionally loved me during my good and bad times. He has faith in me and my intellect even when I felt depressed because I didn't have faith in myself. His support makes me stronger and better than I could be.

Lastly, I am grateful to China Scholarship Council (CSC) and for financing my Ph.D. study.

Abstract

In the past decades, the atmospheric CO₂ emissions increased with the unrestrained combustion of fossil fuels to meet the growing energy demand, leading to serious environmental pollution and climate issues. The electrochemical CO₂ reduction reaction (CO₂RR) is a promising alternative to convert CO₂ into value-added products, and has the potential to contribute to a carbon-neutral energy cycle by using surplus electricity generated from renewable sources (e.g., solar and wind). Among various materials, copper-based catalysts are most studied, given their unique capability to make hydrocarbons in considerable amounts and at reasonable overpotentials.

In this thesis, in-depth understanding of the CO₂ electroreduction process was firstly established by adjusting the local reaction environment of a CuO_x nanoparticle (NP) model catalyst. A tunable product distribution during catalytic CO₂ electroreduction could be achieved by varying areal particle densities and co-feeding CO₂ reactant with CO. With higher areal density and lower mean interparticle distances, a shift in faradic efficiency towards C₂H₄ over CH₄ was observed, which was attributed to enhanced CO_(g) re-adsorption on catalyst surface sites in close proximity. Furthermore, the electroreduction of CO₂ feed with CO-bleeding showed enhanced ethylene production over a broad potential range with various co-feed ratios. The origin of the carbon-atoms in C₂H₄ under co-feed conditions was traced and quantified by a custom-designed *operando* differential electrochemical mass spectrometry (DEMS) flow cell, giving unique mechanistic insight in the CO₂-CO co-feed system. The co-feed mechanism was extended to novel tandem catalysts, in which a CO producer (Ag, or NiNC) works as local CO feeding source and combines with Cu-based catalysts, showing obvious enhancement in ethylene production compared to purely copper-based systems.

Furthermore, a sheet-shaped CuO_x catalyst was designed, developed and systematically investigated. In H-Cell measurements, a high activity for CO₂RR could be observed, followed by tests in a micro flow cell, demonstrating a record C₂H₄ partial current density of 229 mA cm⁻² and a C₂₊ partial current density of ~ 410 mA cm⁻². Moreover, a combination of

operando/(*quasi*) *in situ* XAS, WAXS, DEMS, S/TEM techniques were employed to discover structure-activity-selectivity relations under catalytic CO₂RR operating conditions, delivering perspectives to design novel catalysts to produce hydrocarbons as the value-added products.

Zusammenfassung

CO₂-Emissionen sind in den letzten Dekaden immer rasanter gestiegen, da der erhöhte Energiebedarf der wachsenden Weltwirtschaft vor allem durch fossile Energieträger gedeckt wurde und wird. Dies führt zu immer stärkerer Umweltverschmutzung und hat Auswirkungen auf das weltweite Klima. Die elektrochemische CO₂-Reduktionsreaktion (CO₂RR) bietet hierin eine vielversprechende Chance um CO₂ aus der Atmosphäre oder als direkte Abgasverwertung zu entfernen und in höherwertige Produkte zu wandeln. Wird dazu überschüssige Elektrizität aus erneuerbaren Energien wie z.B. Solarenergie oder Windkraft genutzt, hat die CO₂RR das Potenzial zu einer CO₂-neutralen Energiewirtschaft beizutragen. Unter den bekannten Katalysatoren wurden kupferbasierte Materialien am häufigsten untersucht, da sie die einzigartige Eigenschaft besitzen zu großem Anteil Kohlenwasserstoffe zu produzieren ohne das Überpotential zu stark zu erhöhen.

Diese Arbeit stellt zum ersten Mal ein tieferes Verständnis der CO₂RR her, indem die lokale Umgebung eines CuO_x-Nanopartikel (NP) Modellkatalysators systematisch variiert wurde. Durch Kontrolle der Partikelbeladungsdichte und der Zusammensetzung des Eduktstroms aus CO₂ und CO kann die Produktverteilung gezielt eingestellt werden. Mit steigender Beladungsdichte, d.h. sinkendem Interpartikelabstand, wurde eine Verschiebung der Produkteffizienzen von CH₄ zu C₂H₄ beobachtet, die hier auf verstärkte CO_(g)-Adsorption auf nahe zusammenliegenden Katalysatorzentren zurückgeführt werden konnte. Des Weiteren ermöglicht der co-feed aus CO₂/CO verstärkte Ethylenproduktion in einem breiten Potentialbereich indem das CO₂/CO-Verhältnis angepasst wird. Zur Aufdeckung des Reaktionsmechanismus unter CO₂/CO co-feed wurde die Herkunft der C-Atome im produzierten Ethylen über Isotopenmarkierung in einer eigens dafür designten Flusszelle für *operando* differentielle elektrochemische Massenspektrometrie (DEMS) untersucht und quantifiziert. Der vorgestellte co-feed Mechanismus konnte auf neuartige Tandemkatalysatoren übertragen werden. In diesem wird ein CO-produzierender Katalysator (z.B. Ag oder NiNC) mit einem kupferbasierten Katalysator kombiniert, was ebenfalls zu erhöhter Ethylenproduktion gegenüber rein kupferbasierten Systemen führt.

Außerdem, wurden in dieser Arbeit ein neuartiger, plattenförmiger CuO_x Katalysator entworfen, synthetisiert und systematisch untersucht. Aufgrund herausragender CO₂RR-Aktivität in H-Zellmessungen wurde der Katalysator in einer anwendungsnahen Mikroflusszelle getestet. Dort konnten für C₂H₄ und C₂₊ industrierelevante Rekordproduktstromdichten von 229 mA cm⁻² bzw. ~410 mA cm⁻² gezeigt werden. Weiterhin wurden durch Kombination von *operando/(quasi) in situ* XAS, WAXS, DEMS und S/TEM Techniken Struktur-Aktivitäts-Selektivitätsbeziehungen für die katalytische CO₂RR entdeckt, die neue Wege zum Design von hochaktiven und –selektiven Katalysatoren aufzeigen, um gezielt höherwertige Kohlenwasserstoffe aus CO₂ zu produzieren.

Table of Content

Acknowledgement.....	I
Abstract.....	III
Zusammenfassung.....	V
Chapter 1 Introduction and Motivation.....	1
1.1 Electrochemical CO ₂ Reduction Reaction.....	2
1.2 Electrocatalysts for CO ₂ RR.....	4
1.3 Mechanistic pathways, research progress on Cu-based catalysts for CO ₂ RR.....	5
Chapter 2 Goals and Objectives.....	9
Chapter 3 Aspects and Experimental Procedures.....	13
3.1 Synthesis of shaped copper/copper oxides nanoparticles.....	13
3.1.1 Synthesis of spherical CuO _x nanoparticles (CuO _x NPs).....	14
3.1.2 Synthesis of sheet-like CuO _x nanoparticles (CuO _x NS).....	14
3.1.3 Synthesis of Nickel-Nitrogen-Functionalized Carbon Material (NiNC).....	15
3.2 Physicochemical Characterization.....	15
3.2.1 (Scanning/Transmission) Electron Microscopy.....	16
3.2.2 X-ray Diffraction (XRD).....	18
3.2.3 Inductively Coupled Plasma-Optical Emission Spectroscopy (ICP-OES).....	20
3.3 Electrochemical Characterization.....	21
3.3.1 Electrochemical Methods.....	21
3.3.2 H-Cell configuration.....	22
3.3.3 Micro-Flow-Cell configuration.....	23
3.4 Products quantification.....	24
3.4.1 Online gaseous products quantification.....	24
3.4.2 Liquid products analysis.....	25
3.5 (<i>quasi</i>) <i>in situ/operando</i> Characterization.....	26
3.5.1 (<i>in situ</i>) Synchrotron Wide-Angle X-Ray Scattering (WAXS).....	26
3.5.2 <i>in situ</i> (Scanning/Transmission) Electron Microscopy.....	30
3.5.3 <i>operando</i> Differential electrochemical mass spectrometry (DEMS).....	31

3.3.4 <i>operando</i> X-ray absorption spectroscopy (XAS)	39
Chapter 4 Catalyst particle density controls hydrocarbon product selectivity in CO ₂ electroreduction on CuO _x	43
4.1 Synthesis and characterization	45
4.2 Electrochemical CO ₂ RR over CuO _x catalysts with various areal densities	46
4.3 Discussions	50
4.4 Conclusions	54
Chapter 5 Enhanced Ethylene Yields in the electroreduction of CO ₂ /CO co-feeds on Cu and Cu-Tandem Electrocatalysts: Time-resolved quantitative deconvolution of mechanistic reaction pathways	57
5.1 Synthesis and characterization	59
5.2 Feeding gases control	60
5.2.1 In H-cell design	60
5.2.2 In DEMS flow cell	61
5.3 Electrocatalytic rates and product yields under pure and mixed CO ₂ /CO co-feeds ..	61
5.4 Discussions	64
5.5 Extended co-feed mechanism on bifunctional tandem catalyst design	72
5.6 Conclusions	74
Chapter 6 Sheet-like Copper Oxides with Stable and Selective Ethylene Production for Direct CO ₂ Electroreduction	77
6.1 Synthesis and characterization	79
6.2 Electrochemical CO ₂ RR over sheet-like CuO _x catalysts	81
6.3 Discussions	83
6.4 Conclusions	88
Chapter 7 Achieving high C ₂ H ₄ Evolution at industrial current densities on CuO _x nanosheet derived gas diffusion electrode	89
7.1 CO ₂ RR electrolysis using GDE combined MFC	91
7.2 Discussions	93
7.3 Conclusions	96

Chapter 8 Summary and Outlook.....	97
8.1 Manipulating *CO behavior by local condition	97
8.2 Shaped CuO _x nanoparticles for CO ₂ RR.....	99
8.3 Outlook.....	101
Reference.....	103
Appendix	113
A1. Supplementary Information to Chapter 4.....	113
A2. Supplementary Information to Chapter 5	117
A3. Supplementary Information to Chapter 6	127
A4. Supplementary Information to Chapter 7	137
Table of figures and schemes	140
Table of tables	146
List of Abbreviations.....	147
List of Chemicals.....	149
List of Publications during Ph.D. Study.....	151

Chapter 1 Introduction and Motivation

Population increase, urbanization, living standards upturn, as well as the world-wide industry development, are always accompanying with the increase of energy demand. Fossil fuels, which include coal, oil and natural gas, have been playing a significant role in energy production ever since the industrial revolution.¹⁻⁶ As a significant instance, in the U.S., the largest energy consuming country, 62% of the electricity generation directly relies on fossil fuels. It has been expected, the fossil fuels, serving as the main power source in the last century, and, will continue playing the same role at least for the upcoming decades. We should also keep in mind, combustion of these fossil fuels yields tremendous CO₂ emissions into the nature, which is one of the greenhouse gases that allows radiative forcing and contributes to the global warming.⁷

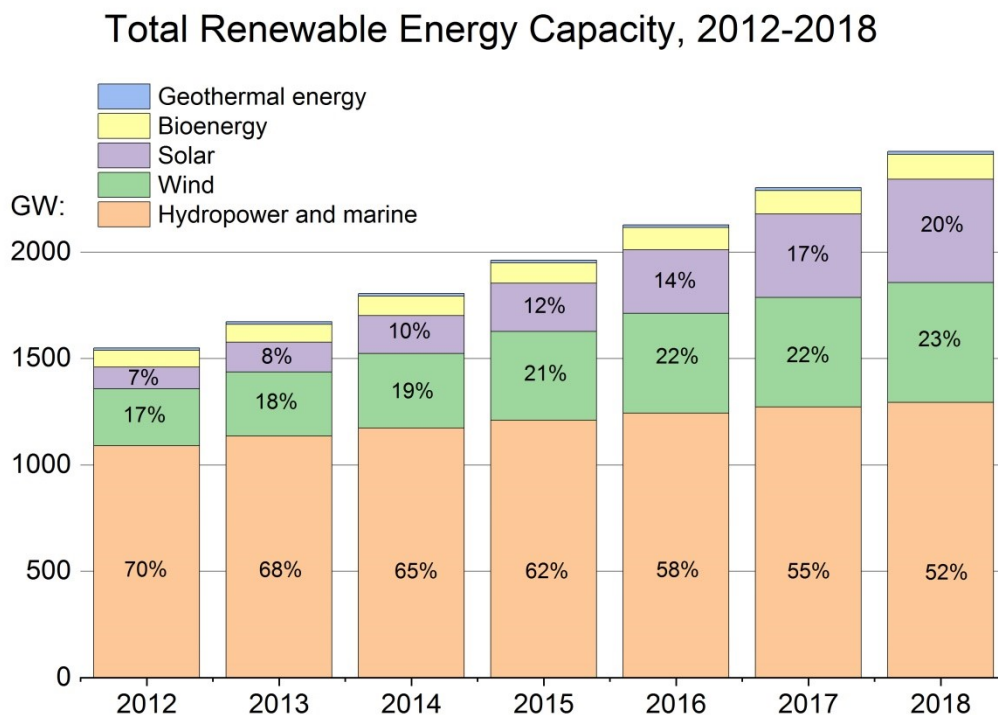


Figure 1.1 Total global renewable energy capacity from Hydropower and marine (orange), Wind (green), Solar (violet), Bioenergy (yellow), Geothermal (blue) sources. Data were taken from ref⁸. Copyright International Renewable Energy Agency.

Thus, low-carbon and high efficiency energy generation are highly desired than ever. The U.S. Energy Information Administration (EIA) estimated that electricity generation from

renewables (i.e. hydropower, solar and wind) would increase to 31% of total generation by 2050, from an 18% share in 2018.⁷ A statistical report from the International Renewable Energy Agency (IRENA) reveals the constitution of global renewable energy capacity varies a lot during the past seven years.⁸ As shown in Figure 1.1, the share of hydropower and marine capacity decreases from 70% in 2012 to 52% in 2018.⁸ Assumptions of declining costs and improving performance make wind and solar increasingly competitive compared with other renewable resources, in particular, the U.S. adds 72 gigawatts of new wind and solar photovoltaic capacity between 2018 and 2021.⁷ However, these resources (solar radiation intensity as well as the wind speed) are normally intermittent and heavily depend on the weather. Thus, how to integrate these intermittent renewable capacities and store them cost-effectively remains a challenge.

Among the different alternatives, electrochemical reduction of CO₂ using the electricity from renewable sources as the driving force is one promising solution.⁹⁻¹⁶ This process could effectively reverse the carbon combustion process, using the CO₂ and water as the feed, delivering carbon-containing fuels and chemicals as the product, schematically realizing a CO₂ neutral process. It is necessary to mention, unlike the Fischer-Tropsch process, operation condition of the electrochemical CO₂ reduction is mild, i.e. room temperature and pressure. The fast response time of electrochemical systems could excellently couple to intermittent renewable energy sources,¹⁷ providing the driving force for such electrochemical transformation. Towards the potential for industrial level utilization, the modular design of electrolyzer enables people to scale up the reaction to kton/day easily,^{18, 19} with properly separating and storing different products yielded from the one-shot reaction. The CO₂RR (electrochemical CO₂ reduction reaction) sector could be populated based on the current manufacture capability.

1.1 Electrochemical CO₂ Reduction Reaction

The studies on CO₂ conversion significantly explode due to the rising of public awareness for environmental protection and the decreasing price of renewable electricity.²⁰⁻³⁶ A general scheme for electrochemical process of CO₂RR is given in Figure 1.2.

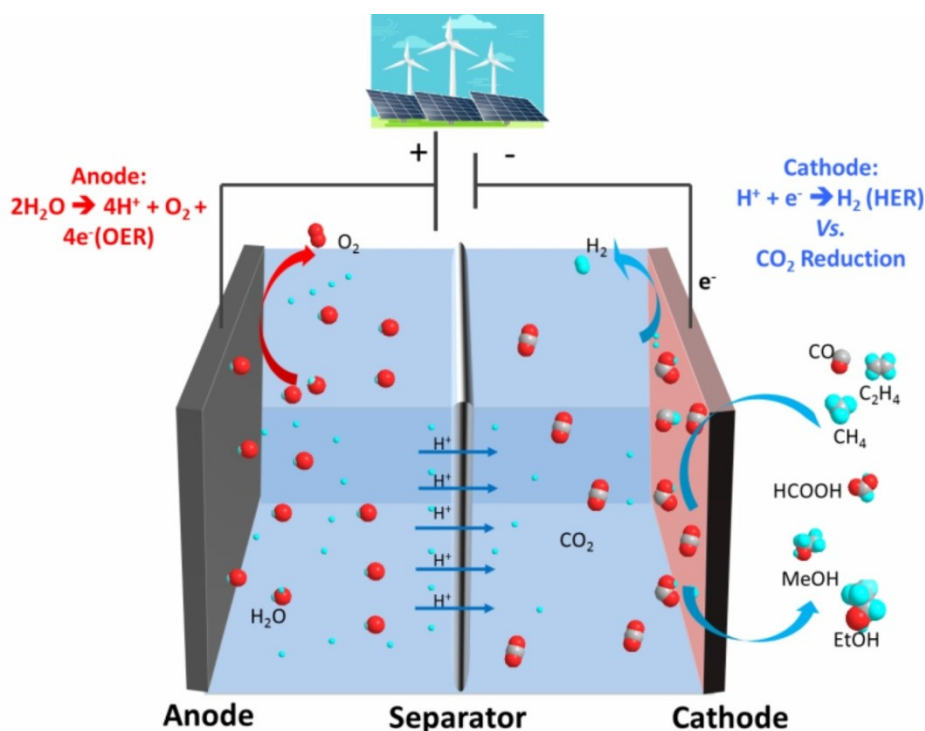


Figure 1.2 General scheme of a typical electrolyzer for CO₂RR.

In a typical CO₂ electrolyzer, the cathode is separated from the anode by a membrane separator. Under external potential, oxygen evolution reaction (OER, [eq. 1-1](#)) occurs on the anode and oxygen is released. Proton, which is another product of water oxidation, could pass the proton-transfer membrane to the cathodic side. Meanwhile, CO₂ gas flows into the cathode chamber and get reduced. As depicted in equations [1-2](#) and [1-3](#), the first possible reduction products, which are thermodynamically more favorable, are HCOOH and CO. Reduction of CO₂ at high overpotentials could also yield alcohols and hydrocarbons ([eq. 1-4](#) to [eq. 1-7](#)). A competitive reduction reaction in the cathodic side is the hydrogen evolution reaction (HER, [eq. 1-8](#)). Choosing the proper catalyst and working condition could suppress the HER to a large extent.





The electrode potentials above are given as SHE at pH 7.

1.2 Electrocatalysts for CO2RR

Two major groups of materials have been screened for catalytically selective CO2RR, namely carbon-based catalysts and metal-based catalysts. Carbon materials have many essential advantages such as high surface area and excellent conductivity. However, the neutral carbon atoms show negligible CO₂-activation ability. Many methods have been developed to improve the catalytic activity and selectivity toward carbon-based materials, for instant, doping of heteroatoms (i.e., nitrogen, boron, and sulfur) into carbon matrix,³⁷⁻⁴² or co-doping non-noble metal atoms and nitrogen atoms (known as M-N-C).^{14, 43, 44} The M-N-C materials, which is regarded as CO maker, has been well studied.⁴⁵⁻⁴⁸ For example, Möller *et al.* found that CO₂ could be selectively converted to CO on nickel and nitrogen-doped porous carbon catalyst (Ni-N-C) at industrial relevant current densities in flow cell setup.⁴⁹

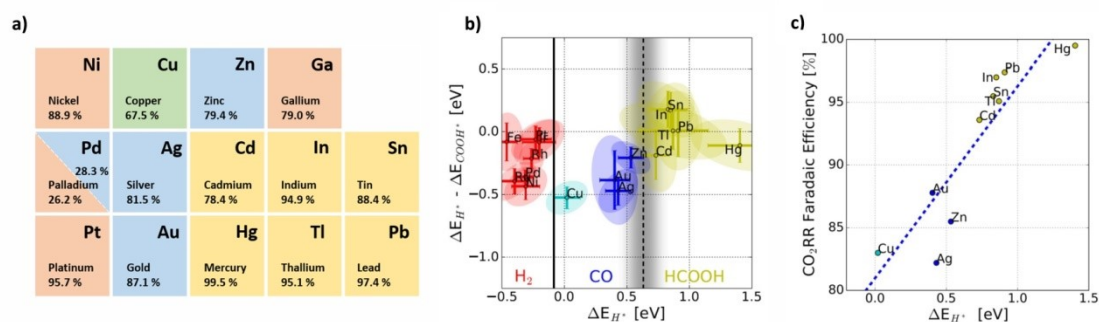


Figure 1.3 Classification of various metals depending on the formation of major products in electrochemical CO₂ reduction. a) Periodic table and faradaic efficiency of major product from experimental data by Hori. H₂ (red), CO (blue), formate (yellow), hydrocarbon (green) b) The experimental product classification of H₂, CO, and HCOOH by the ΔE_{H*}-ΔE_{CO₂H*} and the ΔE_{H*} c) Faradaic efficiency of CO₂ reduction reaction by ΔE_{H*}. a-c) Modified and reproduced from ref⁵¹ with permission. Copyright 2018, John Wiley and Sons.

Pioneered by the Hori, the elemental metallic electrocatalysts for CO₂RR are usually classified with four groups depending on the intermediate affinity and targeting products (see Figure 1.3).^{20, 50, 51} More specifically, for metals (i.e., Pt, Ni, Fe, and Ti) that have high *H affinity and favor HER; for the metals (i.e., Sn, Cd, Hg, In, Tl and Bi) effectively convert CO₂ into formate; for metals (i.e. Au, Ag, Zn, Pd and Ga) that bound CO weakly are known as CO-makers. While copper (Cu) is unique that binds CO neither too strong nor too weak, leading to a considerable amount of valuable ethylene at reasonable overpotentials.⁵²⁻⁷⁰

1.3 Mechanistic pathways, research progress on Cu-based catalysts for CO₂RR

1.3.1 Mechanistic pathways

The unique property of Cu-based catalysts is attributed to the appropriate adsorption energy of CO species (*CO),⁷¹⁻⁷³ which is commonly accepted as a key reactive intermediate on Cu surfaces. Formation of reactive *CO is followed by a protonation pathway to C₁ products, such as CH₄, or by a dimerization pathway to C₂ products, such as C₂H₄.⁷⁴

CO evolution by desorption is known to occur prior to the formation of hydrocarbons and is strong function of the detailed chemisorption properties of CO. Kortlever *et al.* reported that the dimerization step is the rate-determining step in the C₂ pathway.⁷⁴ Huang *et al.* demonstrated the interfacial *CO coverage is a key factor in determining the extent of the C₂H₄ formation.⁷⁵ In their simulation, higher *CO covered surface could decline the energy barrier for *CO dimer, further enhancing the C₂H₄ formation rate.

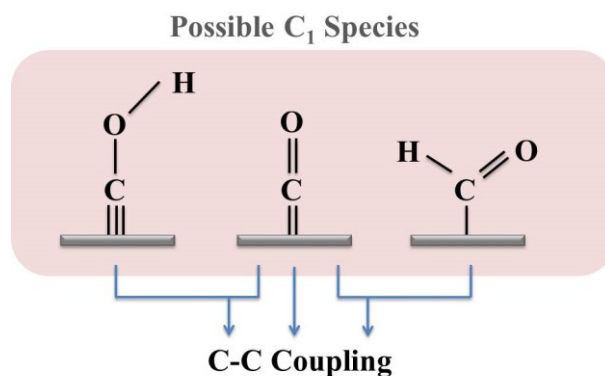


Figure 1.4 Possible C₁ species for C-C coupling.

For the C₂H₄ formation, C-C coupling by different C₁ species is proposed (see Figure 1.4). It is noted that some mechanistic studies are based on CO reduction, since CO₂RR is essentially a self CO co-feeding system. Kortlever *et al.* reported a mechanism consisting of the coupling of two *CO molecules based on DFT results.⁷⁴ This pathway follows: *C₂O₂ → *C₂O₂⁻ → *CO-COH → *CCO → *CHCO → *CHCHO → *CH₂CHO → C₂H₄. Cheng *et al.* demonstrated that the hydrogenation of *CO-COH to *COH-COH is more favored than its dehydration to form *CCO.⁷⁶ Besides *CO-*CO dimerization, Goodpaster *et al.* found that the dimerization of *CO and *CHO, forming *COCHO, is more favorable at high overpotential.^{77, 78} Cheng *et al.* suggested that the coupling of *CO and *COH favors the formation of *CO-COH instead of *COCHO.^{79, 80} Montoya *et al.* demonstrated that the dimerization of hydrogenated species (*CH₂O and *CHO) is kinetically more favorable than *CO dimerization in an electrochemical environment.⁸¹

Many parameters can be used for tuning the product selectivity on Cu electrocatalysts.⁷²⁻⁸⁶ For example, it is found that the products distribution during CO₂RR is sensitive to the exposed Cu facets.⁸⁷⁻⁹¹ With Cu (111) facet, CH₄ formation is enhanced, while (100) facet favors C₂H₄ formation.^{82, 84-86}

1.3.2 Research progress on Cu-based catalysts for CO₂RR

Many investigations have shown that oxide-derived copper catalyst (OD-Cu), which are formed by *in situ* reduction of CuO_x during catalytic CO₂RR, are promising due to their enhanced C₂ products yield.⁹²⁻⁹⁴ It is suggested that several parameters, such as the effects of grain boundaries, local pH, under-coordinated sites, CO coverage, and subsurface oxygen, have been attributed to the enhanced activity and selectivity towards “beyond CO” productd.⁹³⁻¹⁰⁵ (see Figure 1.5)

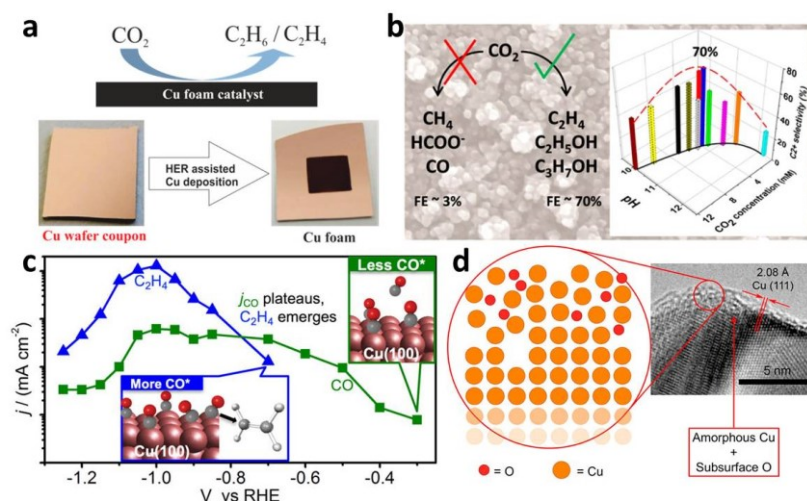


Figure 1.5 a) Tuning the product distribution of CO₂ electroreduction on OD-Cu foam catalysts. b) Optimizing C-C coupling on oxide-derived copper. c) Effects of CO* coverage on the selective formation of ethylene. d) Nature and distribution of stable subsurface oxygen in OD-Cu. a) to d) are adapted from ref^{97, 102, 75 and 112,} respectively, with the permission, copyright American Chemical Society.

Surface roughness and grain boundary

The roughened surfaces of OD-Coppers are composed of a large number of under-coordination sites (edges, steps, and defects) which are more active for CO₂RR. The sites at the grain boundary are suggested to change the binding energies of different adsorbates and decrease the energy barriers for the formation of key intermediates, thus leading to particular products (Figure 1.5a).^{87, 94, 96, 106-108}

Local pH

As CO₂RR involves multi- protons and electrons transfer processes, it is suggested that the local pH near the electrode surface need to be considered.⁶⁰ Xiao *et al.* found that the donation of proton from water nearby for the dehydroxylation to ethylene is more favorable at neutral pH.¹⁰⁹ Lum *et al.* demonstrated a moderate pH near OD-Cu electrode enhanced C₂₊ products, suppressing the formation of C₁ product (Figure 1.5b).¹⁰²

CO coverage

It is also demonstrated that the activation barrier for the dimerization is dependent on the coverage of *CO on the OD-copper surface (Figure 1.5c).^{75, 86} High coverage of adsorbed *CO decreases the energy barrier of the formation of C-C bond and favors the C-C coupling of C₁ intermediates to ethylene.

Subsurface oxygen

Combining experimental and theoretical results, several groups suggested that the presence of subsurface oxygen (Figure 1.5d) favors both CO₂ activation and C-C dimerization, leading to an increased ethylene formation.^{69, 110, 111} Cavalca *et al.* proposed the subsurface oxygen withdraws electrons from the sp- and d-bands of copper, thus the selectively decreases the energy barrier of C-C coupling.¹¹² However, the role of subsurface oxygen in CO₂RR is in debate and needs more careful discussion. Garza *et al.* found that the oxygen in the subsurface of Cu (100) is unstable.^{101, 113} Agreeing with the role of subsurface oxygen, in increasing the coverage of *CO and decreasing *H adsorption, Liu *et al.* suggested that the presence of subsurface oxygen doesn't necessarily change the free-energy activation barrier.¹¹⁴

In summary, although the above parameters are studied for obtaining a selective electrocatalysts, detailed mechanistic studies are still needed for a better catalyst design. Recent advanced *in situ/operando* techniques provide an excellent opportunity to gain catalytic insight on both CO₂RR mechanism and catalyst matrix. Besides, it should be noted that these factors are correlated with each other rather than absolutely independent. For example, changing the surface roughness also accompanying with the change of local pH.¹⁰² Comprehensive consideration is also required in the complex system.

Chapter 2 Goals and Objectives

This work is focused on the electrocatalytic reduction of carbon dioxide (CO₂RR) towards value-add products over copper-based nanoparticles. First goal (1) of this work is to improve the catalytic activity and selectivity of the C₂ products, the second (2) is to expand the state-of-mechanistic understanding, and the final (3) goal is to design novel catalysts with high C₂ products yielding.

Using spherical CuO_x nanoparticles as a model material, the influence on the nanoparticle assembles was firstly investigated. The catalytic activities, as well as the C₂ products distribution, are studied and attributed to the re-adsorption behavior of key *CO intermediate. To further uncover the contribution of the interfacial CO, CO₂ with CO co-feeding system is then investigated using advanced electrochemical methods and *operando* differential electrochemical mass spectrometry (DEMS). Based on the co-feed mechanism, Cu-based tandem catalysts are designed and measured for CO₂RR. Moreover, the shape selected CuO_x-derived nanoparticles are also promising candidates. A detailed understanding of the evolution behavior in both phase and morphology aspects is also the goal. Advanced *in situ* (*operando*) wide-angle X-Ray scattering (WAXS), X-ray absorption spectroscopy and (Scanning/Transmission) Electron Microscopy are used as most directive and best approaches to investigate a chosen CuO_x nanoparticle system under real operating condition.

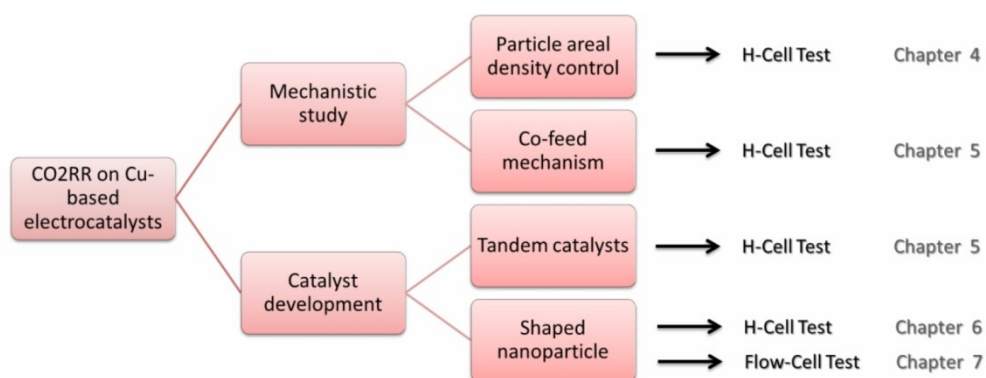


Figure 2.1 Schematic overview of scientific questions and goals dealt with in the course of this work.

In Chapter 3, the experimental procedures used in this work are described in detail, including material synthesis and physicochemical characterizations. The quantification of CO₂RR

products, which are detected by home-build on-line GC, liquid-GC, HPLC for liquid products analysis, is explained as well. Furthermore, the description of advanced *in situ (operando)* methods is shown at the end of this chapter.

In Chapter 4, the relationship between reactive *CO dimerization behavior and areal particle density are investigated on a family of monodispersed copper oxide nanoparticles (CuO_x NPs) during the CO₂RR. Rietveld-refined catalytically active CuO_x NPs are correlated to hydrocarbons production and efficiency under systematic variation of the particle density and hence mean distance inside the 3D catalyst layers. We demonstrate that improved C₂H₄ yields are achieved using high areal particle density (reduced mean-particle distance with the increased real surface area) and attribute this to dynamically favored CO(g) re-adsorption at elevated local interfacial pH.

In Chapter 5, we systematically investigate the effective hydrocarbon production rates during the CO₂RR on Cu-based nanocatalysts under variations of the CO₂/CO feed ratio. The emphasis is placed on the kinetics of the catalytic ethylene formation. The dissolved CO_x species are carefully controlled by the feeds' partial pressure in an H-type cell. To uncover the mechanistic origin of the enhanced ethylene formation rates, we conducted mixed, isotope-labeled (¹²C/¹³C) feed experiments in a newly developed CO₂RR-specific capillary electrochemical cell attached to our differential electrochemical mass spectrometer (DEMS). Using our DEMS technique, we not only trace the chemical-mechanistic origin (from either dissolved CO or CO₂) of the two carbon atoms in the C₂H₄ product molecules, but also succeed in quantifying the relative contribution of the competing mechanistic reaction pathways toward C₂H₄. Even though the focus of this chapter is on the electrochemical kinetics and dominant mechanistic pathways and not on the chemical state dynamics of the Cu-based catalyst, high-energy X-ray diffraction (HE-XRD) and Rietveld refinement were used to clarify the initial population of crystalline Cu phases and their time evolution. Building on more mechanistic insights on local CO co-feeding, we close our report in demonstrating a new family of hybrid carbonous/metal, metal/metal tandem CO₂RR catalyst

concepts that succeed in realizing full local CO self-co-feeding benefits now even under pure CO₂ feeds.

In Chapter 6, the investigation is extended on the new catalyst design. With successfully synthesized sheet-like copper oxide nanoparticles, regular H-cell measurement is firstly applied for CO₂RR. A combination of (*in situ/operando*) grazing incidence wide-angle X-Ray scattering (WAXS), X-ray absorption spectroscopy are used to examine the phase/local atomic structure evolution of highly active CuO_x nanoparticles under operating CO₂RR electrolysis condition. The millisecond-resolved *operando* differential electrochemical mass spectrometry (DEMS) was employed to determine the onset potential shift of the products with gradually self-electroreduced CuO_x electrocatalyst to purely metallic Cu phase. SEM measurement is also performed to check the morphology evolution after CO₂ electroreduction process.

In Chapter 7, further gears the as-prepared CuO_x nanosheet into a Micro-Flow-Cell (MFC) configuration equipped with a Gas Diffusion Electrode (GDE) and manipulated the current density from lab-scale to industry relevant level. Remarkably, the catalyst poses a faradaic efficiency exceeding 33% ethylene at high current (700 mA cm⁻²) with suppressed HER, since the gas diffusion layer allows overcoming the CO₂ reactant transport limitation compared to H-cell design. More importantly, the morphological transformations of free-standing CuO_x nanosheets are also investigated in an electrochemical liquid TEM cell set up, comparing with different devices. The present study corroborates the power of *in situ* electrochemical liquid TEM studies for the understanding of activity-selectivity-morphology relations under catalytic CO₂RR operating conditions at the industry level.

In Chapter 8, summarizes the results of this thesis, and general conclusions are drawn. Additionally, perspectives for further investigations on the catalysts design and device development are given.

Chapter 3 Aspects and Experimental Procedures

Experimental Procedures reproduced in part with permission from [ChemSusChem, 2017, 10, 4642-4649](#) (Copyright of The John Wiley and Sons (2017))¹²⁶ and from [Nat. Nanotechnol., 2019, 14, 1063-1070](#) (Copyright of Springer Nature)¹²⁷. Experimental Procedures reproduced in part from manuscripts under preparation for submission.

A List of Chemicals listing Acronyms, Purity/Concentration and Supplier is attached to the Appendix Section on [page 147](#).

This chapter presents all synthesis routes of a series of shaped Cu-based nanoparticles that are investigated in this work. Following, regarding methodologies for physicochemical characterization as well as the procedures for electrocatalytic performance (activity, selectivity, durability, and scalability) testing will be described. In the final session of this chapter, the experimental details on the performed *in situ* analytical and X-ray/microscopy methods will be given including a brief explanation on the theoretical fundamentals of the most important methods used in this work.

3.1 Synthesis of shaped copper/copper oxides nanoparticles

The development synthesis methods for copper/copper oxides are necessarily needed since copper is not easily reduced due to its low standard reduction potential under mild condition and high oxygen affinity. In order to prepare narrow size-distributed, homogeneously shaped nanoparticles, different synthesis methods, including wet chemistry method and thermal decomposition, are carefully adjusted and applied in this work. Table 3.1 gives an overview of the Cu-based nanoparticles and in the corresponding chapters they are studied. The first set of catalysts are spherical CuO_x nanoparticles (CuO_x NPs), which are used for catalysts areal density study, co-feed mechanistic insight study and as well as hybrid tandem catalysts. The second one is sheet-like CuO_x nanoparticles (CuO_x NS), which are employed for various advanced *operando* studies and flow cell study.

Table 3.1 Overview of different materials used in this work with the corresponding chapters in which their characterization is discussed.

Material	Oxidation States	Chapter
CuO _x nanospheres (CuO _x NPs)	Cu (0, I, II)	4, 5
CuO _x nanosheets (CuO _x NS)	Cu (I, II)	6, 7

3.1.1 Synthesis of spherical CuO_x nanoparticles (CuO_x NPs)

All chemicals are used as commercial ones without further purification. The synthesis was operated at all times under a rigorously protective atmosphere of N₂. In a typical route, 430.35 mg CuBr, 9.7 g trioctylphosphine oxide (TOPO, 90%, Sigma Aldrich), and 10 mL oleylamine (90%) were added in a three-necked flask. The mixture was then heated to 80 °C with magnetic stirring. After being kept at this temperature for additional 15 min, 100 mg Borane tert-butylamine complex (TBAB, 97%, Sigma Aldrich) was added to the resulting homogeneous solution. The mixed solution was heated up to 200 °C and kept at this temperature for 60 min with stirring. As the reaction progressed, the colour of the mixture changed from light blue to red. The resulting red colloidal products were collected by centrifugation, and washed several times with hexane and ethanol. Finally, the products were re-dispersed in hexane and the content of copper was detected by ICP-OES. Or freeze dried and stored as powders under inert atmosphere until use.

3.1.2 Synthesis of sheet-like CuO_x nanoparticles (CuO_x NS)

No purification was performed for chemicals before use. CuO_x nanosheets (CuO_x NS) were obtained by thermal decomposition of the pre-synthesized Cu(OH)₂ intermediate. To prepare the Cu(OH)₂ intermediate, 100 mg Cu(Ac)₂ (Sigma Aldrich) was dissolved in 4 mL DMF (N,N-dimethylformamide, Aldrich)/ Milli-Q water (> 18 mΩ cm), 2.5 mL 1M KOH solution was then added into the solution dropwise into the solution. After 15-min stirring, 500 μL ammonium hydroxide and 500 μL water were added. The resulting homogeneous light blue solution was then transferred to a glass pressure vessel with a capacity of 47 mL. The sealed

vessel was then heated from room temperature to 60 °C in 30 min and stayed at 150 °C for 12 h before cooling to room temperature. The products were precipitated by ethanol, separated via centrifugation at 7350 rpm and further purified twice by ethanol and water. After freeze-drying, the obtained powders were stored as powders under an inert atmosphere until use.

3.1.3 Synthesis of Nickel-Nitrogen-Functionalized Carbon Material (NiNC)

Ni-N-C catalyst synthesis follows analogous procedure presented in ref²². Ketjen EC 600JD (AzkoNobel) was initially dispersed in 0.5 M HCl for one day stirring and vacuum filtered with DI water till neutralized. Afterward, this neutralized carbon powder was leached in concentrated HNO₃ for 8 hours at 90 °C to modify the surface and thereafter vacuumed filtered with DI water to neutral again. The obtained carbon powder will be referred to as carbon support. For the following-up synthesis, the carbon support was sonicated in 50 mL DI-water for 15 minutes.

For NiNC catalyst synthesis, 3 mL of Aniline, 5 g NiCl₂ salt and 5 g Ammonium Persulfate (APS, (NH₄)₂S₂O₈) were added into 500 mL of 1 M HCl, and kept stirred for one hour. 400 mg sonicated carbon support (mentioned above) was added into this suspension and stirred for 48 hours at ambient condition. After that, the suspension was dried in the air at 95 °C for 24 hours. The obtained solid mixture was ball-milled and heat treated (HT) in a furnace under N₂ condition for carbonization. The heating temperature was controlled with a ramping of 30 °C min⁻¹ to 900 °C and kept at this temperature for 60 min. The cooled down material powder was washed in 2 M sulfate acid (AW) for overnight to remove the exposed inorganic species and rinsed to neutral pH by using vacuum filtration. The final NiNC catalyst was obtained with the protocol HT-AW-HT-AW-HT-AW-HT.

3.2 Physicochemical Characterization

Due to the variety of methods used in this work, an overview and experimental description of all physicochemical characterization techniques used in this thesis will be summarized in the following sessions, starting with essential methods such as SEM, TEM/STEM, XRD and

ICP-OES followed by more advanced *operando* analytical techniques such as DEMS, WAXS, XAS etc.. Table 3.2 gives references to the sub-sections with the experimental descriptions and the corresponding chapters in which the results are presented and discussed.

Table 3.2 Overview of Methods for physicochemical characterization used in this thesis with reference to the sections in which they are described. x indicates the application of the method for the corresponding result chapter.

Method		Ch. 4 –	Ch. 5 –	Ch. 6 –	Ch. 7 –
SEM		x	x	x	x
TEM		x	x	x	x
STEM			x		x
XRD		x (laboratory)	x (synchrotron)	x (synchrotron)	
ICP-OES		x			
Elemental mapping			x		
<i>In situ</i>	DEMS	x		x	
	WAXS	x	x	x	
	TEM	x			x (quasi)
	XAS			x	

3.2.1 (Scanning/Transmission) Electron Microscopy

Theoretical Aspects

The electron microscope is capable of much higher magnifications and has a greater resolving power than a light microscope, allowing it to see much smaller objects in finer detail. The minimum separation (d) that can be resolved by any kind of a microscope is given by the following formula:

$$d = \frac{\lambda}{2n \sin\theta} \quad \text{eq. 3-1}$$

Where n is the refractive index (which is 1 in the vacuum of an electron microscope), λ is the wavelength, and θ is the maximum half-angle of the cone of light that can enter the lens.

According to the formula, one can improve resolution by using shorter wavelengths and mediating with larger indices of refraction. Electron microscopy is designed to use extremely short wavelengths of accelerated electrons to form high-resolution images. Figure 3.1 displays how the electron beam interacts with the samples. By using different scattering beam and/or transmitted beam, we could gain information of the sample from different aspects.

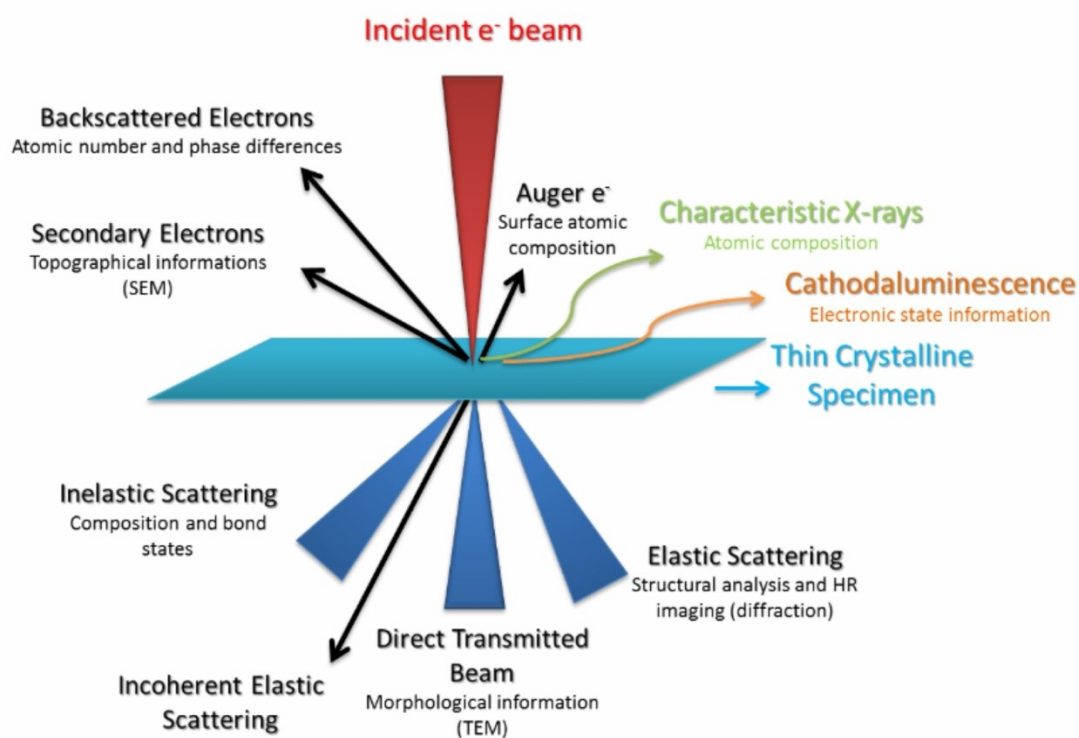


Figure 3.1 lists the interaction between electrons and samples used for different techniques.

3.2.1.1 Scanning electron microscopy (SEM)

SEM is a nondestructive method to obtain the information about morphology, particle size, and surface topography. The SEM was measured using a JEOL 7401F instrument at an acceleration voltage of 10 kV and a working distance of approximately 4.1 mm. Image J was employed to analyze the SEM images.

3.2.1.2 (Scanning) Transmission electron microscopy (S/TEM)

The TEM is used to study nanoparticle morphology. TEM images were obtained using an FEI Tecnai G² 20 S-TWIN equipped with a LaB₆ cathode operating with 200 kV acceleration voltage and a resolution limit of 0.24 nm. A Cu grid (200 mesh) coated with a holey carbon

film was impregnated with the sample solution and air-dried at 60 °C. An FEI TECNAI G² 20 S-TWIN microscope, equipped with a GATAN MS794 P CCD-detector operated at 200 kV was used. The mean particle size was determined from the TEM images by counting at least 200 particles.

The STEM-EDS elemental maps were acquired using an FEI Titan 80-200 (“ChemiSTEM”) electron microscope, equipped with a Cs-probe corrector (CEOS GmbH) and a high-angle annular dark field (HAADF) detector. The microscope was operated at 200 kV. In order to achieve “Z-Contrast” conditions, a probe semi-angle of 25 mrad and an inner collection semi-angle of the detector of 88 mrad were used. Compositional maps were obtained with energy-dispersive X-ray spectroscopy (EDX) using four large-solid-angle symmetrical Si drift detectors. The quantitative analyses were performed on Cu K and O K.

3.2.2. X-ray Diffraction (XRD)

Theoretical Aspects

Similar to other electromagnetic radiation, X-ray can be treated as either a wave or a particle. The wave-particle duality of light is defined as

$$E = h\nu = \frac{hc}{\lambda} \quad \text{eq. 3-2}$$

where $h\nu$ is the energy of the photon with h being Planck's constant, and ν the frequency and λ the wavelength of the wave. For E in eV and λ in nm, $E = 1239.8/\lambda$.

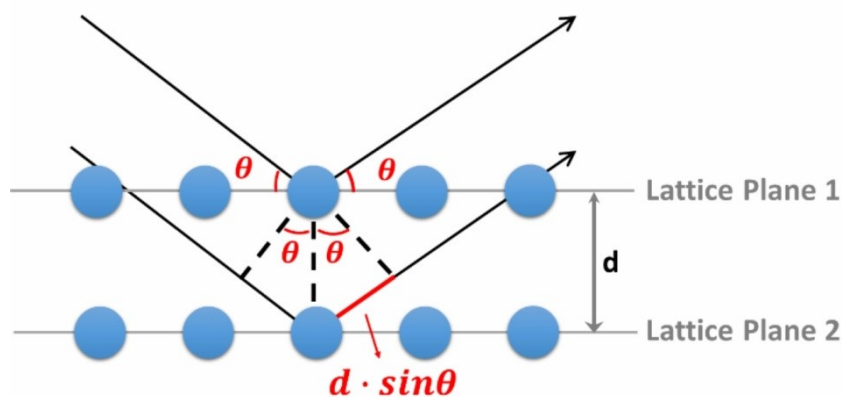


Figure 3.2 Schematic illustration of the Bragg equation.

Diffraction is the effect following the interaction of an electromagnetic wave with an object having a size dimension comparable with the period of the wave. The Bragg diffraction occurs when the reflected beams are in phase and interfere constructively. Schematic illustration of the Bragg equation is shown in Figure 3.2, and expressed mathematically in Bragg's law as following

$$n\lambda = 2d \cdot \sin\theta \quad \text{eq. 3-3}$$

where θ is scattering angle, λ is the wavelength of the incident X-ray wave, and d is the interplanar distance of the lattice planes, while n is a positive integer ($n = 1, 2, \dots$).

Experimental Description

The X-ray diffraction (XRD) technique is a powerful method to obtain the information about the bulk structure of crystalline materials and can provide information on unit cell dimensions. The diffraction patterns are based on constructive interference of monochromatic X-rays and the sample.

The profiles were acquired on a Bruker D8 Advance diffractometer with Cu K α radiation and a Lynx Eye detector (point detector). Samples were analyzed between 30-95° 2 θ , with a step size of 0.04° and collection time of 7s. Data analysis was carried out using MDI Jade 9 and TOPAS 4.2.

Rietveld refinement

Rietveld refinement is a treatment of powder XRD data which is particularly useful in the case of a multiphase material. Information about the structure of different phases, i.e., unit cell dimensions, phase quantities, atomic coordinates/ bond length and so on, can be extracted with this method. It was described by Hugo Rietveld in the 1960s.¹¹⁵ The Rietveld Method involves: 1) recording the diffracted intensities with different crystal phases;) 2 creating a crystal structure model, i.e., symmetry, atomic positions, unit-cell size, site occupancies; 3) varying these and other parameters by least squares refinement to get the best fit between calculated and observed data. Peak shape and the geometry of the diffractometer set-up are also taken into account. The Rietveld refinement is generally used for solving an unknown crystal structure, calculating the amount of disorder or mixing on a Wyckoff site,

quantitatively determining the percentages of different phases in a sample and determining the crystallite sizes.

XRD intensities observed at diffraction (goniometer) angles (2θ) are supposed to be constant with the calculated intensities $(y_{cal})_i$ by using an appropriate model.

$$(y_{cal})_i = \sum_l [S_l \sum_{lk} (M_{lk} A_{lk}(2\theta_i) P_{lk} |(F_{cal})_{lk}|^2 LP(2\theta_i) \phi_{lk}(2\theta_i))] + y_{bkg} \quad \text{eq. 3-4}$$

where,

$(y_{cal})_i$ – Calculated intensity of i^{th} data point of a powder pattern that comprises of l phases

S_l – Scale factor of the l phase

M_{lk} – Multiplicity

$A_{lk}(2\theta_i)$ – Absorption factor

P_{lk} – Preferred orientation factor

$(F_{cal})_{lk}$ – Structure factor for particular reflection

$LP(2\theta_i)$ – Lorentz-Polarization factor

$\phi_{lk}(2\theta_i)$ – Profile function

y_{bkg} – Background intensity of i^{th} data point

While the experimentally observed powder XRD profile is an outcome of the combination of many such scan intensities $((y_{cal})_i)$ that are calculated using these math functions and correction terms. Successful fitting procedures require high quality experimental data and a large q -range, as well as reasonable structure model(s) to minimize residual function at i^{th} data point over all data points N , which can be expressed as:

$$M = \sum_{i=1}^N w_i [(y_{obs})_i - (y_{cal})_i]^2 \quad \text{eq. 3-5}$$

where,

$(y_{obs})_i$ – Measured intensity of i^{th} data point

w_i – The weight of the diffraction pattern's intensity and is given by equation 3-4:

$$w_i = [(y_{cal})_i]^{-1} \quad \text{eq. 3-6}$$

3.2.3 Inductively Coupled Plasma-Optical Emission Spectroscopy (ICP-OES)

Theoretical Aspects

ICP-OES is a method of optical emission spectrometry, which is developed by Fassel *et al.* Iowa State University in the US and by Greenfield *et al.* at Albright & Wilson, Ltd. in the UK in the 1960s.¹¹⁶ It is a powerful tool to determine trace elements in a myriad of sample types. Figure 3.3 shows the Bohr model of an atom, which is depicted as a nucleus and surrounded by electrons in discrete orbitals.

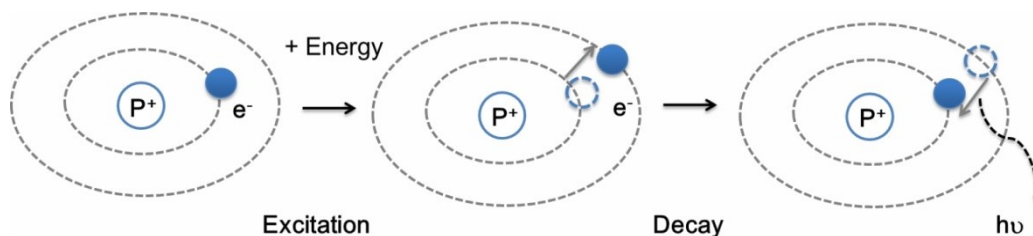


Figure 3.3 Bohr model of an atom. When energy is absorbed by an atom, the electron jumps from its *ground* state orbital to an orbital with higher energy level. For the stabilizing, the atom may decay back to a lower energy state by emitting a photon, $h\nu$.

In ICP-OES measurement, the component elements (atoms) are excited when plasma energy is given to an analysis sample from outside. When the excited atoms return to low energy position, emission rays ($h\nu$) that is corresponding to the photon wavelength are released and measured. The element type is determined based on the position of the photon rays, and the content of each element is determined based on the emission intensity.

Experimental Description

The metal content Cu was analyzed by inductively coupled plasma-optical emission spectroscopy (ICP-OES) using a Varian 715-ES spectrometer with a CCD detector. In Chapter 4, 400 μL catalyst/hexane solution was carried out directly after synthesis and dried in N_2 . Then powders were digested in acid (HNO_3 : H_2SO_4 : HCl in a 1:1:1 ratio) and kept for overnight. The samples were diluted with Milli-Q water ($> 18 \text{ m}\Omega \text{ cm}$) to reach an appropriate emission intensity. Standards with a known concentration were co-analyzed with the samples.

3.3 Electrochemical Characterization

3.3.1 Electrochemical Methods

RHE Potential:

$$E_{RHE} = E_{Ref} + E_{Ag/AgCl} + 0.059 * pH + R * I \quad eq.3-7$$

E_{RHE} : RHE potential / V

E_{Ref} : Applied WE potential against the Ag/AgCl reference electrode / V

$E_{Ag/AgCl}$: Potential of the reference electrode measured against NHE (0.21 V) / V

pH: pH-value of the electrolyte

R: Ohmic resistance between working and reference electrode / Ω

I: Total measured current / A

3.3.2 H-Cell configuration

The Schematic illustration and photograph of H-type cell are shown in Figure 3.4. In the operating condition, the reduction reaction of CO_2 and/or CO happens in the working part and oxygen evolution reaction occurs in the counter compartment. Three-electrode system was applied for H-type configuration. Polished glassy carbon or carbon paper are used as working electrodes and measured with a Biologic SP 300 potentiostat. A platinum mesh 100 (Sigma-Aldrich 99.9%) was used as a counter electrode (CE) and a leak-free Ag/AgCl electrode as a reference electrode (Multi Channel Systems MCS GmbH). A certain amount of catalyst ink (a solution of 2 mg catalyst, 50 μ L of 5 % Nafion, 150 μ L of isopropanol and 800 μ L of ultrapure water) was drop-coated on 1 cm^2 of working electrode to vary the catalyst loading for each study.

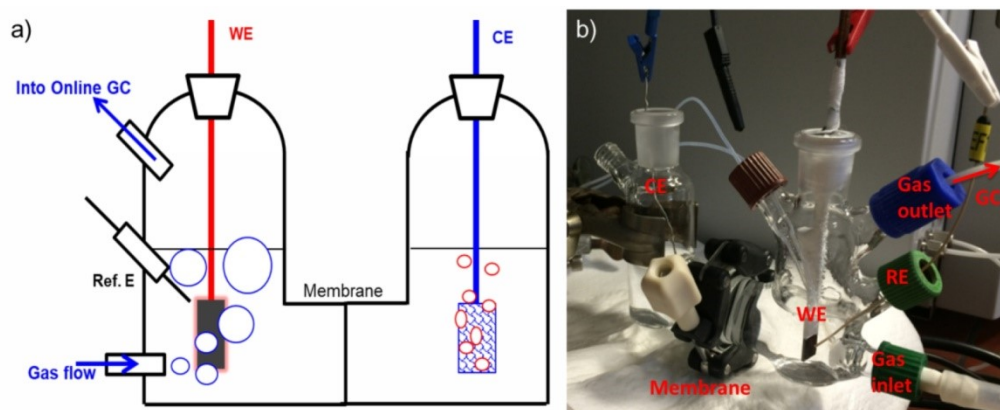


Figure 3.4 a) Schematic and b) photograph of H-type two compartments cell divided by a polymer membrane.

The working/counter compartment was filled with 40 mL of electrolyte, respectively. Before and during the electrochemical reaction the working compartment was purged continuously with various feeds (30 sccm in total) from the bottom of the cell and the gas atmosphere was controlled with an *in situ* mass flow controller. Every measurement was started with a linear voltammetric sweep, performed with a scan rate of -5 mV/s between $E = +0.05 V_{\text{RHE}}$ and the working potential (between $-0.78 V_{\text{RHE}}$ and $-1.0 V_{\text{RHE}}$) followed by a chronoamperometric step for a certain time. All reported potentials are corrected for ohmic drop determined by electrochemical impedance spectroscopy (EIS). EC-Lab software was used to automatically correct 50% of the Ohmic drop, the remaining 50% was corrected manually. For each measurement, a fresh electrolyte was used to ensure that adsorbates from previous experiments did not influence the result.

3.3.3 Micro-Flow-Cell configuration

The micro-flow-cell (MFC) is used for measuring the samples at high current densities, which were performed in a commercial cell supplied by ElectroCell. The catalyst ink (a solution of 6 mg catalyst, a certain amount of 5 % Nafion, isopropanol and ultrapure water) was spray-coated on the microporous layer (MPL) of a Freudenberg C2 gas diffusion layer (GDL). A geometric area of 3 cm^2 was coated to achieve a final metal loading of $\sim 1 \text{ mg cm}^{-2}$. Additionally 30 wt% of Nafion was used as a binder and for ionic conductivity of the catalyst layer. 1 M KHCO_3 (500 mL, Sigma-Aldrich, BioUltra, $\geq 99.5\%$) was used as anolyte and catholyte, which were separated by an anion exchange membrane (Selemion AMV, AGC Engineering Co., LTD.).

Both electrolytes were cycled through each respective compartment at 100 mL min^{-1} by using a peristaltic pump (PMP Ecoline, Cole-Parmer). The CO_2 (4.5N) was supplied at a rate of 50 mL min^{-1} to the cathode and was flown from the back of the GDL through the catalyst layer. Measurements were performed galvanostatically for 2 h at each respective current during the catalytic tests, changing the current from low to high values. Each galvanostatic step was followed by a PEIS measurement to account for the ohmic drop in the calculation of RHE potentials.

3.4 Products quantification

As reported in the literature, more than 16 products are formed on Cu electrocatalyst during CO₂RR, including both gaseous products and liquid products. Table 3.3 is summarized the products which are detectable in our lab and their corresponding detection method.

Table 3.3 Summary of the detectable products in the H₂O/CO₂RR electrolysis and the corresponding detection methods.

Products	Detection Method	Detection limitation
H ₂	GC	1ppm
CO	GC	1ppm
CH ₄	GC	1ppm
C ₂ H ₄	GC	1ppm
HCOO ⁻	HPLC	0.1mM
CH ₃ COO ⁻	HPLC	0.1mM
EtOH	Liquid GC	1ppm
PrOH	Liquid GC	1ppm
Aldehyde	Liquid GC	1ppm

3.4.1 Online gaseous products quantification

Gas samples were analyzed with a gas chromatograph (Shimadzu GC 2014) equipped with a thermal conductivity detector (TCD) and a flame ionization detector (FID). Argon (Air liquid 5.0) was employed as the carrier gas. The gaseous compounds H₂, N₂, O₂, CH₄ and CO were separated in a molecular sieve column (Alltech, part no. 57732, 1.65 m × 1/8 in., molecular sieve 13X, 60/80 mesh) while for C₂-C₃ hydrocarbons and CO₂ in a HayeSep column (Alltech, part no. 14487, 3.5 m × 1/8 in., HayeSep D, 80/100 mesh).

The production rate towards the gas products was calculated taking into account the concentration obtained for the gas chromatography analysis and the feed flow (30 sccm) according to the following equation:

$$\dot{n} = \frac{\dot{V} * C}{A * V_M} \quad \text{eq.3-8}$$

\dot{n} : Generation rate of the product / mol s⁻¹ cm⁻²

\dot{V} : CO₂ gas flow rate / L s⁻¹

C: Volume/Molar fraction of detected product by GC (assuming ideal gas) / Vol%

A: Geometric area of the electrode / cm²

V_M: Gas Molar Volume / 22.4 L mol⁻¹

The measured molar production rate was used to calculate the Faradaic efficiency and the average current density measured during the last minute of reaction:

$$FE = \frac{\dot{n} * z * F}{j_{total}} * 100\% \quad \text{eq.3-9}$$

\dot{n} : Molar production rate of product per unit area / mol s⁻¹ cm⁻²

FE: Faradaic Efficiency of the product / %

z: number of transferred electrons per mol of product

F: Faraday constant / 96500 C mol⁻¹

j_{total} : Total current density during CO₂ bulk electrolysis / mA cm⁻²

3.4.2 Liquid products analysis

2 mL of the electrolyte after reaction was analyzed by high performance liquid chromatograph (HPLC Agilent 1200, Zimmer Chromatography® Column, RID detector) to measure formic acid concentration and analyzed by liquid injection gas chromatography (Shimadzu GC 2010 plus, Fused-Silica-Capillary Column, REF 723060.30, FID Detector) for alcohol products. Therefore, the production rate was calculated considering the total charge transfer, according to the following equation:

$$\dot{n}_x = \frac{V * \Delta C_x}{A * \Delta t} \quad \text{eq.3-10}$$

\dot{n}_x : Generation rate of the product x / nmol s⁻¹ cm⁻²

V: Volume of the electrolyte / mL

ΔC_x : Accumulated concentration of the product x detected by HPLC or liquid GC / mmol L⁻¹

A: Geometric area of the electrode / cm²

Δt : Reaction time at const. current or potential / s

Faradaic efficiency of liquid products is calculated by the following equation:

$$FE_x = \frac{V * \Delta C_x * z_x}{\Delta Q} * 100\% \quad \text{eq. 3-11}$$

FE_x : Faradaic Efficiency of the product x / %

V: Volume of the electrolyte / mL

ΔC_x : Accumulated concentration of product x detected by HPLC or liquid GC / mmol L⁻¹

z_x : electrons transferred for reduction to product x

ΔQ : Total charge transfer during the electrolysis at const. potential or current / C

The partial current density,

$$j_x = \frac{FE_x * j_{total}}{100} \quad \text{eq. 3-12}$$

j_x : Partial current density / mA*cm⁻²

FE_x : Faradaic Efficiency of the product x / %

j_{total} : Total current density / mA*cm⁻²

3.5 (*quasi*) *in situ/operando* Characterization

In this thesis, various *in situ/operando* methods were applied to analyze both catalysts properties and clear products evolution under operating electrochemical reaction conditions. These methods will be described in the following sections, beginning with *in situ* X-ray based setup and methods, followed by the electron microscopy.

3.5.1 (*in situ*) Synchrotron Wide-Angle X-Ray Scattering (WAXS)

In this work, *operando* synchrotron WAXS was used to determine the phase evolution of as-prepared CuO_x nanoparticles under operating CO₂ electroreduction condition. Synchrotron facilities could provide higher energy due to the fact that an electron accelerator could produce high-flux radiation with excellent properties. Such measurements allow to reach larger q, and thus 2θ, a wider range of the diffraction pattern, which is necessary for advanced data analysis (Rietveld refinement and pair distribution function (PDF) analysis) revealing the fine structural details. Moreover, comparing to lab source X-ray diffractometer with a point

detector, the large area detector (Pilatus 3X CdTe 2M) has advantages in accuracy for detecting the materials with preferred orientation and considerably shorter acquisition times. Azimuthally integrated line profiles provide us additional information for texture strain. Results from *ex situ* WAXS measurement on CuO_x NPs are discussed in Chapter 5, and *in situ* WAXS measurements on CuO_x NS during CO₂RR are presented in chapter 6.

Theoretical Aspects

The structural investigation by X-ray scattering mainly depends on elastic scattering, without any change of energy/wavelength of incoming/measured beam. Figure 3.5 shows the geometry defining when a fraction of the incident beam (wavelength λ) is scattered by the sample in the experiment.

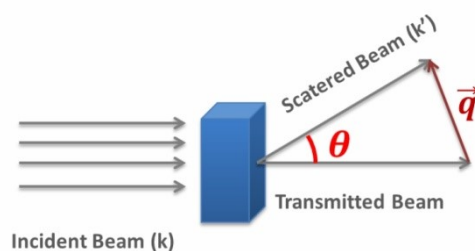


Figure 3.5 Geometry defining the incident beam and scattered beam with scattering vector \vec{q} .

The measured intensity of the scattered beam $I(\vec{q})$ corresponds to the square of the Fourier transform of the scattering length density distribution. The scattering vector \vec{q} is defined as the difference between the wave-vector of the incident and the scattered beam (Figure 3.5).

$$|\vec{q}| = q = \frac{4\pi \sin \theta}{\lambda} \quad \text{eq. 3-13}$$

In the wide angle range, the observed scattering intensities are related to the interplanar spacing between the crystallographic planes (d) in the crystal, which can be expressed by a modified Bragg equation,

$$d = \frac{\lambda}{2 \sin \theta} = \frac{2\pi}{q} \quad \text{eq. 3-14}$$

Experimental Description

(*in situ*) synchrotron WAXS measurements were performed at ID31 at the European Synchrotron Radiation Facility (ESRF) in Grenoble, France, at relatively high energy of ~ 70 keV. The working distance between the sample and the detector was calibrated using a CeO₂

standard (NIST SRM 674b). The diffraction patterns were corrected by the empty beam. The dry sample was prepared by placing a small amount of catalyst powder (1 mg) between two layers of Kapton tape for *ex situ* WAXS measurement. The samples for *in situ* measurements were prepared by drop-casting CuO_x electrocatalysts ink (a solution of 50 μ L 5 % Nafion and 800 μ L ultrapure water (18.2 M Ω cm, PureLab Plus System, Elga) and 150 μ L isopropanol) onto the glassy carbon cylinder (diameter, 2.5 mm) which was polished with 1/0.05 μ m Al₂O₃ suspension and cleaned with ultrapure water before. The catalyst loading was kept as 20 μ g cm⁻² to avoid overloaded current density. Rietveld refinement was performed using the TOPAS® software package (Bruker).

Figure 3.6a shows a schematic illustration of the setup as employed for the *in situ* experiments operated at a synchrotron in this work. The side view and top view of the test station was presented in Figure 3.6b and Figure 3.6c, respectively. The experimental setup consists of an electrochemical cell with a three electrode configuration. The Ag/AgCl (3M KCl, World Precision Instruments) reference electrode was placed in vicinity to the working electrode via a polytetrafluoroethylene (PTFE) capillary. A Pt mesh and a glassy carbon cylinder were used as counter electrode and a working electrode. The electrochemical cell was then covered by an X-ray transparent, chemically-inert and -resistant Prolene foil (Chemplex®, 4 μ m). A PTFE tubing beside the reference electrode allows the pre-CO₂-saturated electrolyte flowing inside the sealed cell. The outlet of the electrolyte shares the glass tubing with the counter electrode. The working electrode is placed on a PCTFE rod and is held by a slight under pressure which is ensured by a membrane pump. A demister unit is applied between the sample holder and membrane pump to safe the pump from flooding in case of electrolyte leakage. The sealing between sample and sample holder is realized by Viton® O-Ring and the sample is contacted from the backside using a Ti wire.

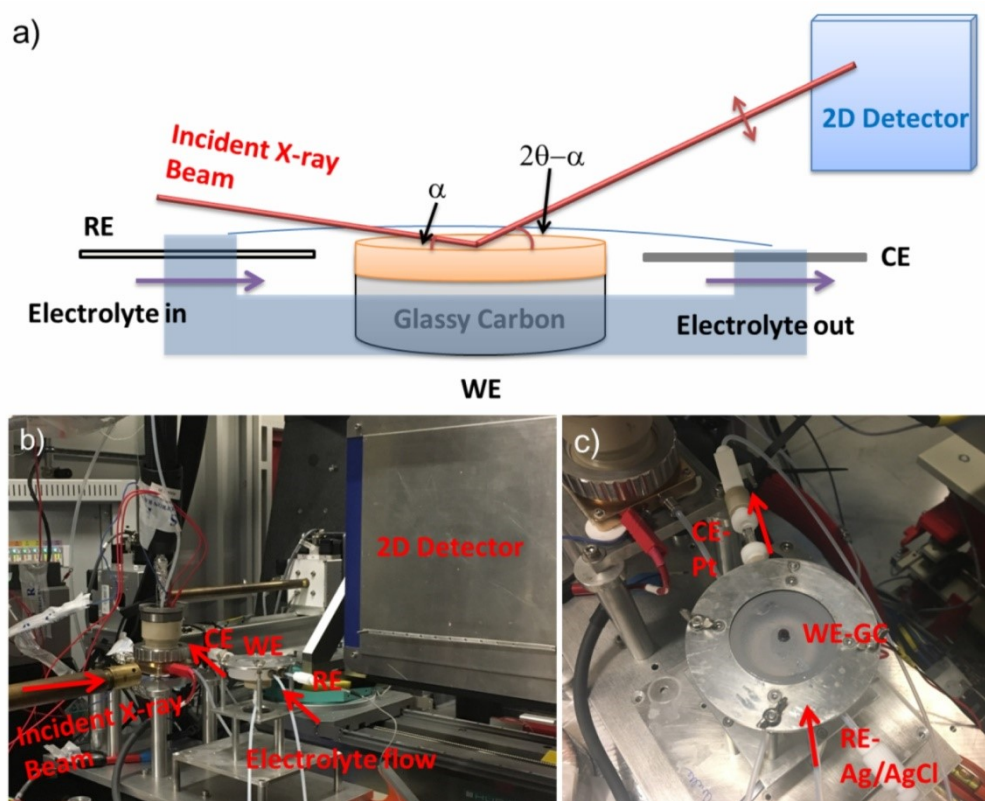


Figure 3.6 a) Schematic illustration of the *in situ* WAXS setup under electrochemical condition using at a synchrotron facility, showing the incident and scattered X-rays, the 2D detector and the grazing incidence cell. b) The side view and c) the top view of the test station at the European Synchrotron Radiation Facility (ESRF).

During characterization, the electrolyte was continuously pumped through the cell using a peristaltic pump. We used CO_2 -saturated 0.1M KHCO_3 as the electrolyte. The height of the working electrode should be carefully adjusted to minimize the scattering and attenuation of X-ray by the water molecules.

We collected WAXS spectra within 30 s data acquisition time. The experimental protocol was the following:

1. Diffraction pattern of dry film
2. Diffraction pattern with electrolyte
3. LSV with 5mV/s from -0.02 to -0.84 V_{RHE}

Diffraction patterns were taken between 0 min to 130 min every 10 min while -0.84 V_{RHE} was applied. Beam damage was controlled after each experiment.

3.5.2 *in situ* (Scanning/Transmission) Electron Microscopy

In this thesis, conventional Transmission Electron Microscopy (TEM) was used in order to check the morphology/size distribution of as-prepared nanoparticles. The liquid electrochemical TEM was employed for investigating the particles evolution, combining with the *ex situ* test cell.

The results using liquid electrochemical TEM techniques and *ex situ* test cell are presented in Chapter 7.

Experimental Description

Poseidon Select electrochemical cell holder (Protochips) was used to load the samples into the microscope and maintain the liquid environment (see Figure 3.7) for the experiment. By using E-chips, electrochemistry measurement can be performed on a three-electrode system. Both big and small E-chips are delivered with a protective photoresist coating to prevent damage to the SiN membrane. Acetone and methanol were used to remove the protective photoresist coating. The three electrodes are placed on the big chip with glassy carbon as working electrode, Pt as reference electrode and Pt as the counter electrode. The CuO_x catalyst nanoparticles were dispersed in ethanol and drop cast onto the center of the big E chip with electrodes, which were plasma cleaned before use.

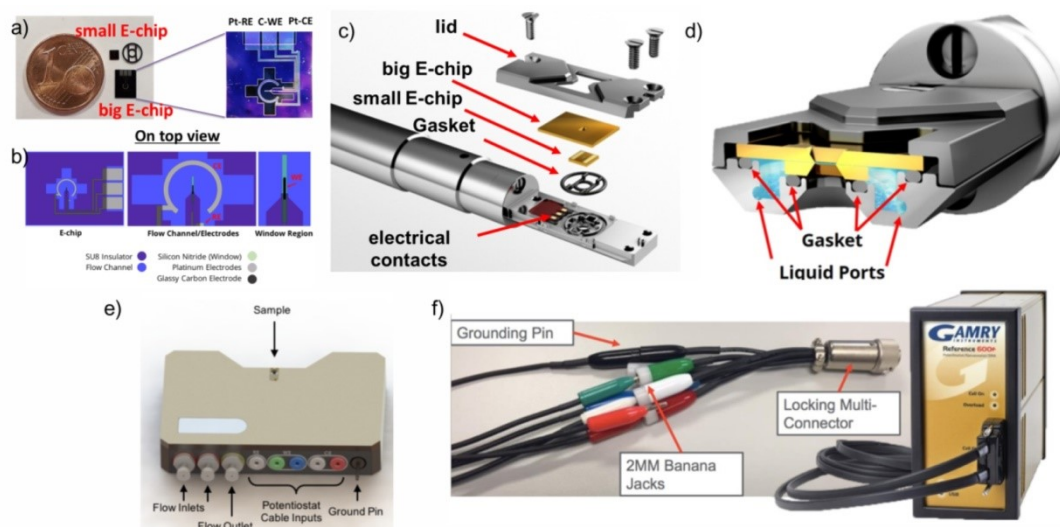


Figure 3.7 a) Photograph and dimension of the electrochemistry chips with enlarged big E-chip, in comparison to 1 euro cent. b) Chip design and three-electrode system applied on

the big E-chip, showing the glassy carbon working electrode in the center, surrounded by the Pt reference electrode (grey) and the Pt counter electrode (light grey). c) Assembling of the liquid E Chem holder with gasket, big/small E-chips and lid. d) Side view of the chip with the corresponding bottom chip and the electrolyte layer between the chips. e) *ex situ* cell with same chip assemble, flow mode and electrochemical connection. f) Gamry potentiostat for the liquid E Chem holder and *ex situ* cell. Images are partly adapted from “Workflow & Training Poseidon Select Version 1.2; Copyright 2017, Protochips, Inc.” with permission from Protochips.

After assembling, solution of 0.1 M Na₂HPO₄/NaH₂PO₄ (pH=6.9) (Sigma Aldrich with milli-Q water) was delivered by an external Hamilton syringe pump through the microfluidic tubing into the tip of the Poseidon Select TEM holder at 30-300 μL h⁻¹. Then the flow rate was decreased to 30-50 μL h⁻¹ for vacuum check and real experiments. Microscopy was performed using an FEI TECNAI G² 20 S-TWIN microscope with a GATAN MS794 P CCD-detector at 200 kV. Experiments taken with *ex situ* cell used the same procedure.

After using, a cleaning step needs to be performed. All lines were purged with water for overnight and rinsed by ethanol. Dry air was used to purge the lines and flush the holder tip.

The chip design in *ex situ* cell is the same as *in situ* liquid holder. Thus, the chips used in the *ex situ* cell can be re-checked in microscopy with liquid EChem holder after rinsing.

Specifications of Pt Ref (E-Chip ECT-45CR-10)

Calculation of potential setting in Gamry:

$$E_{\text{Apply}} = E_{\text{RHE}} + E_{\text{adj}} \quad \text{eq. 3- 15}$$

$$E_{\text{adj}} = E_{0-\text{Pt}} + 0.059\text{V} * \text{pH} \quad [E_{0-\text{Pt}} = -1.18 \text{ V}] \quad \text{eq. 3- 16}$$

Since the current is quite low in both *ex situ* cell and liquid E Chem holder, no IR correction was considered.

3.5.3 *operando* Differential electrochemical mass spectrometry (DEMS)

For *operando* differential electrochemical mass spectrometry (DEMS) measurements, inks of as-prepared CuO_x electrocatalysts ink were prepared with a solution of 50 μL 5 % Nafion and 800 μL ultrapure water (18.2 MΩcm, PureLab Plus System, Elga) and 150 μL iso-propanol. The ink was sonicated and subsequently certain amount of catalyst ink was deposited onto the glassy carbon cylinder (diameter, 5 mm) which was polished with 1/0.05 μm Al₂O₃

suspension and cleaned with ultrapure water before. The final catalyst loading was $100 \mu\text{g cm}^{-2}$. In this thesis, *operando* DEMS measurements are used for 1) investigating the co-feed mechanism on CuO_x NPs with ($^{12}\text{C}/^{13}\text{C}$) isotope labeling feeds; 2) determining the onset potential for major products on electrochemically self-reducing CuO_x NS. This part of work is collaborated with Jorge Ferreira de Araújo, from the Technical University of Berlin.

Results from *operando* DEMS measurements on CuO_x NPs for co-feed study are presented in chapter 5 and on CuO_x NS for tracing products onset potential is included in chapter 6.

Experimental Description

Operando Differential electrochemical mass spectrometry (DEMS) was done using a custom-made TU Berlin electrochemical capillary DEMS flow cell (See Figure 3.8). DEMS capillary flow cell is characterized by having a well-defined electrolyte profile flow over the working electrode. The reaction products are transported into the interface liquid vacuum throughout a 0.15 mm glass capillary. The collection of high concentrated aliquot near catalyst surface and enhanced liquid-vacuum interface allows a fast and at high-intensity detection of gaseous products. The high performance with DEMS capillary flow cell results in the distributed flow over the hydrophobic membrane compartment also known as the cyclonic flow. The interface liquid/vacuum promoted by PTFE hydrophobic membrane with a pore size of 20 and thickness of $50 \mu\text{m}$ (Cobetter®, Cat. No. PF-002HS) are commercially available at Hangzhou Cobetter Filtration Equipment Co., Ltd. The reaction products after been vaporized into the vacuum chamber from the flow cell were detected using a Prisma™ quadrupole mass spectrometer (QMS 200, Pfeiffer-Vacuum). The vacuum chamber was composed of two turbomolecular pumps (HiPace 80) that perform an ultimate pressure 10^{-6} mbar at MS detectors. Each turbomolecular pump has an independent baking system helped a by membrane and oil pump (coupled with a molecular sieves oil trap).

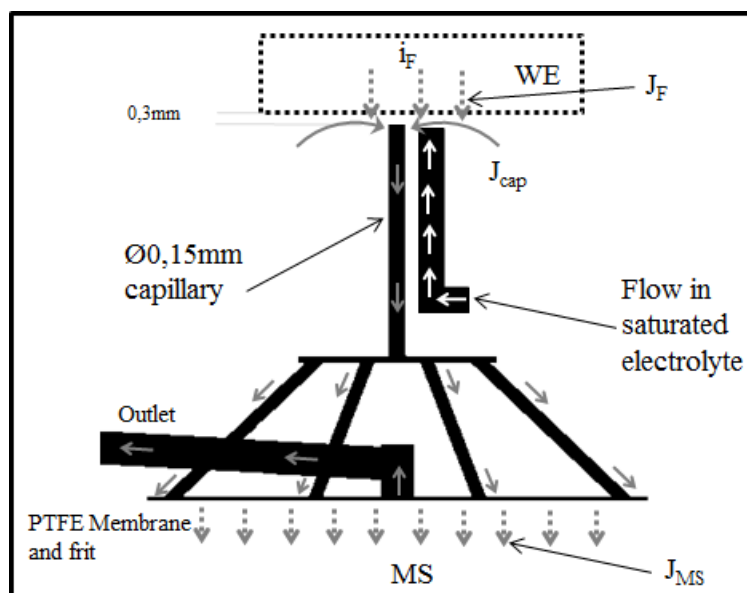


Figure 3.8 Schematic DEMS setup - custom-made TU Berlin electrochemical capillary DEMS flow cell.

At the reaction compartment, the flow in of electrolyte should be pre-saturated with gas feeds. Schematic view of the saturation setup used for this thesis is presented in Figure 3.9. The system is composed of one/two saturation stack for different feed gases (CO_2 and/or CO). The degasification electrolyte is pumped into the stacks and saturated in parallel and independently from each gas. After the saturation stack, the electrolyte saturated with CO_2 and/or CO is mixed up at the desired ratio before entering the electrochemical flow cell. In co-feed mechanism study (in Chapter 5), the pure CO_2 measurement was performed similarly but instead of CO was replaced by Argon feed.

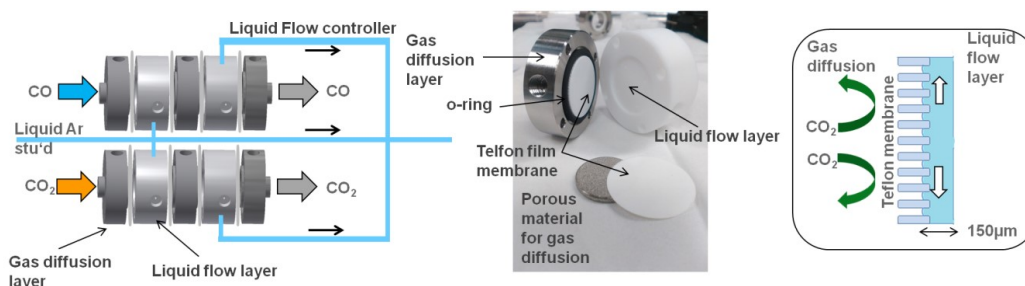


Figure 3.9 Schematic view and photography of feed gas control system at DEMS setup - saturation of electrolyte in the flow stream.

Isotopes labeled gas was also conducted during the co-feed mechanism study. The volume of isotopes gas could be minimized in a closed system (high ratio of saturated on electrolyte for

a volume of gas). To avoid mass fragment overlapping with CO₂ fragmentation, we choose to label ¹³C on CO instead of CO₂ to have a true comparison with pure CO₂ feeding and to avoid carbon mixing with CO₂ as KHCO₃-derived. Pure ¹³CO measurement was not performed due to ubiquitous of CO₂ as KHCO₃-derived in bicarbonate solutions. We tracked the origin carbon sources by labeling one of the carbon within co-feed species (¹³CO) maintaining constant the CO₂ to CO ratio. Our DEMS isotopes experiments are performed in gas feed ratio of 1 to 3, namely CO₂/CO and CO₂/¹³CO.

Onset potential determination methodology

The onset potential is defined as the potential where ion current signal reaches 1% from the highest detected signal of a correspondent product between all gas feeding systems during a cathodic voltammetric scan of 5 mV/s.

DEMS-based deconvolution of reactive pathways

The following calculation based on DEMS results is used for co-feed mechanism study. Detailed discussion of ethylene pathways in the co-feed condition is included in Chapter 5.

The three reactive pathways toward ethylene via the dimerization of two *CO adsorbates derived from CO₂ only, CO only, and of CO₂ and CO (cross-coupling) are denoted throughout as “CO₂-CO₂”, “CO-CO”, and “CO₂-CO”, respectively. While these name labels do not include isotope labels at the carbon atoms, we emphasize that our experimental measurements and subsequent analysis included and considered isotope labeled ¹³CO in the feed. A typical mass spectrum of ethylene gas directly dissolved in 0.1 M KHCO₃ and measured at DEMS setup is presented in Figure 3.10.

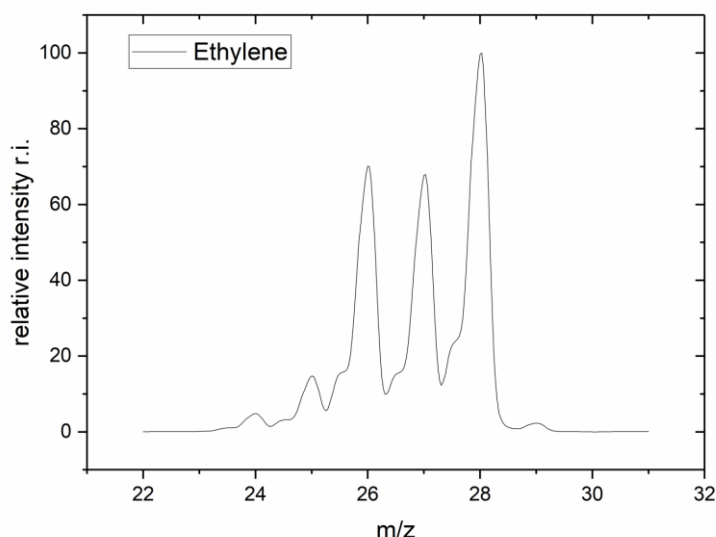


Figure 3.10 A typical mass spectrum of ethylene gas directly dissolved in 0.1 M KHCO_3 and measured at DEMS setup.

To arrive at a DEMS based kinetic deconvolution we focused on the hydrogen-abstracted molecular ethylene fragment, denoted as $(M - H^+)$ henceforth. Its chemical sum formula identity is C_2H_3^+ . Under isotope labeling, the three distinct $(M - H^+)$ fragments of interest are then $^{13}\text{CCH}_3^+$ for the “ $\text{CO}_2\text{-CO}$ ” mechanism ($m/z = 28$), $^{12}\text{C}_2\text{H}_3^+$ for the “ $\text{CO}_2\text{-CO}_2$ ” ($m/z = 27$), and $^{13}\text{C}_2\text{H}_3^+$ for the “ CO-CO ” ($m/z = 29$). The relative contribution of each CO dimerization pathways was evaluated based on the distribution of specific isotope-labeled fragments. The ion mass intensities of interest, $I_{m/z=27}$, $I_{m/z=28}$, and $I_{m/z=29}$, were, in part, deconvoluted from direct measurements or, in case of ion mass overlaps of different fragments, from relative intensity relations provided.

More specifically, the evaluation of the relative contributions of each mechanism started with the experimentally measured ion current intensities $I_{m/z=26}(\text{CO}_2\text{-CO}_2)(\text{CO}_2\text{-CO})(\text{CO-CO})$, $I_{m/z=27}(\text{CO}_2\text{-CO}_2)(\text{CO}_2\text{-CO})$ and $I_{m/z=30}(\text{CO-CO})$, which, as shown by the subscripts, involved various fragment overlaps from the three dimerization pathways. The extraction of $I_{m/z=27}$, $I_{m/z=28}$, and $I_{m/z=29}$ was achieved using the following analysis:

Mass 27 ($\text{CO}_2\text{-CO}_2$)

We note that the mass $m/z = 27$ is composed of 50% of the $\text{CO}_2\text{-CO}_2$ and 50% of $\text{CO}_2\text{-}^{13}\text{CO}$ mechanism (see Table 3.4).

Table 3.4 All main possible fragments of ethylene including CO and CO₂ species. Relative intensity (R.I.) of various mass fragments and their structural assignment (Assgn.) for ethylene (C₂H₄, ¹³CH₂CH₂ and ¹³CH₂¹³CH₂), carbon dioxide, carbon monoxide and ¹³C-carbon monoxide (CO₂ and CO and ¹³CO).

	Ethylene		^{13/12} C-Ethylene		¹³ C-Ethylene		carbon dioxide		carbon monoxide		¹³ C- carbon monoxide	
Molecule	C ₂ H ₄		¹³ CH ₂ CH ₂		¹³ CH ₂ ¹³ CH ₂		CO ₂		CO		¹³ CO	
	C ₂ H ₄ m/z 28		C ₂ H ₄ m/z 29		C ₂ H ₄ m/z 30		m/z 44		m/z 28		m/z 29	
Masses	R.I.	Assgn.	R.I.	Assgn.	R.I.	Assgn.	R.I.	Assgn.	R.I.	Assgn.	R.I.	Assgn.
24	5	C ₂ ⁺										
25	15	C ₂ H ⁺	5	¹³ CC ⁺								
26	70	C ₂ H ₂ ⁺	15	¹³ CCH ⁺	5	¹³ C ₂ ⁺						
27	68	C ₂ H ₃ ⁺	70	¹³ CCH ₂ ⁺	15	¹³ C ₂ H ⁺						
28	100	M ⁺	68	¹³ CHCH ₂ ⁺	70	¹³ C ₂ H ₂ ⁺	10	CO ⁺	100	M ⁺		
29			100	M ⁺	68	¹³ C ₂ H ₃ ⁺	0.1	¹³ CO ⁺	1.2	¹³ CO ⁺	100	M ⁺
30					100	M ⁺			0.4	C ¹⁸ O ⁺		
44							100	M ⁺				
45							1.2	¹³ CO ₂ ⁺				

The latter results from control experiments that evidenced a 50% decrease of the m/z=26 signal intensity upon addition of labeled ¹³CO. To evaluate the contribution of CO₂-CO to m/z=26, that is I_{m/z 26 (CO₂-CO)}, we used the fragment relation intensity factor 0.21 from our experimental ethylene mass spectrum analysis (Table 3.5).

Table 3.5 Resume of the main ethylene fragments used for the DEMS based deconvolution of the contribution of each reaction pathways with relative intensity (r.i.) and fragment assignments (Assgn.) of the three ^{13}C dimerization mechanisms resulting in ethylene formation (C_2H_4 , $^{13}\text{CH}_2\text{CH}_2$ and $^{13}\text{CH}_2^{13}\text{CH}_2$). The three mechanisms are denoted as “CO₂-CO₂” if both carbon atoms of ethylene derive from $^{12}\text{CO}_2$, ”CO₂-CO” in case of mixed origin and “CO-CO” if both carbon atoms derive from ^{13}CO .

	CO ₂ -CO ₂		CO ₂ -CO		CO-CO	
Molecule	C_2H_4		$^{13}\text{CH}_2\text{CH}_2$		$^{13}\text{CH}_2^{13}\text{CH}_2$	
	C ₂ H ₄ m/z 28		C ₂ H ₄ m/z 29		C ₂ H ₄ m/z 30	
Masses	R.I.	Assgn.	R.I.	Assgn.	R.I.	Assgn.
26	70	C_2H_2^+	15	$^{13}\text{CCH}^+$	5	$^{13}\text{C}_2^+$
27	68	C_2H_3^+	70	$^{13}\text{CCH}_2^+$	15	$^{13}\text{C}_2\text{H}^+$
30					100	M^+

With $I_{m/z\ 26}(\text{CO-CO})$ being directed deconvoluted from experimental $I_{m/z\ 30}(\text{CO-CO})$, we are now able to deconvolute $I_{m/z\ 26}$ by simple subtraction of $I_{m/z\ 26}(\text{CO-CO})$, resulting in $I_{m/z\ 26}(\text{CO}_2\text{-CO}_2)$.

$$I_{m/z\ 27}(\text{CO}_2\text{-CO})^* = (I_{m/z\ 27}(\text{CO}_2\text{-CO}_2)(\text{CO}_2\text{-CO})(\text{CO-CO}) - I_{m/z\ 30}(\text{CO-CO}) \times 0.15) / 2$$

$$I_{m/z\ 26}(\text{CO}_2\text{-CO})^* = 0.21 \times (I_{m/z\ 27}(\text{CO}_2\text{-CO})^*)$$

$$I_{m/z\ 26}(\text{CO-CO}) = I_{m/z\ 30}(\text{CO-CO}) \times 0.05$$

Then,

$$I_{m/z\ 26} \rightarrow I_{m/z\ 26}(\text{CO}_2\text{-CO}_2)$$

$$I_{m/z\ 26}(\text{CO}_2\text{-CO}_2) = I_{m/z\ 26} - I_{m/z\ 26}(\text{CO}_2\text{-CO})^* - I_{m/z\ 26}(\text{CO-CO})$$

$$I_{m/z\ 27}(\text{CO}_2\text{-CO}_2) = I_{m/z\ 26}(\text{CO}_2\text{-CO}_2) \times 0.97$$

The calculated $I_{m/z=27}(\text{CO}_2\text{-CO}_2)$ represents ion mass signal at $m/z=27$ from the ethylene molecule (M) with loss of hydrogen atom; we denoted as $M - \text{H}^+$.

Mass 28 (CO₂-CO) correction intensity

Having already calculated the mass intensity $I_{m/z=26}(\text{CO}_2\text{-CO}_2)$ and using the fragment intensity factor 0.97. Now we discard the assumption of 50% CO₂-CO₂ and 50% CO₂-CO as for $I_{m/z=26}(\text{CO}_2\text{-CO}_2)$ we deconvolute the signal mass 27 (CO₂-CO) using the previously determined $I_{m/z=27}(\text{CO}_2\text{-CO}_2)$. Finally, we determine $I_{m/z=28}(\text{CO}_2\text{-CO})$ using an extrapolation based on ethylene fragment relative intensity signal.

$$I_{m/z=27}(\text{CO}_2\text{-CO}) = I_{m/z=27}(\text{CO}_2\text{-CO}_2) (\text{CO}_2\text{-CO}) (\text{CO-CO}) - I_{m/z=27}(\text{CO}_2\text{-CO}_2) - I_{m/z=27}(\text{CO-CO})$$

$$I_{m/z=27}(\text{CO-CO}) = I_{m/z=30}(\text{CO-CO}) \times 0.15$$

$$I_{m/z=28}(\text{CO}_2\text{-CO}) = I_{m/z=27}(\text{CO}_2\text{-CO}) \times 0.97$$

The calculated $I_{m/z=28}(\text{CO}_2\text{-CO})$ represents ion mass signal at $m/z=27+1$ (¹³C) from the ethylene molecule (M) with loss of hydrogen atom, we denoted as $M - \text{H}^+$.

Mass 29 (CO-CO) correction intensity

The signal at $m/z=30$ is exclusive to the mechanism (CO-CO), allowing us to directly determine mass 29 based on ethylene fragment relative intensity signal from the experimental measured $I_{m/z=30}(\text{CO-CO})$, then $I_{m/z=29}(\text{CO-CO})$ was determined. The relation factor is 0.68.

$$I_{m/z=29}(\text{CO-CO}) = I_{m/z=30}(\text{CO-CO}) \times 0.68$$

The calculated $I_{m/z=29}(\text{CO-CO})$ represents ion mass signal at $m/z=27+2$ ($2 \times ^{13}\text{C}$) from the ethylene molecule (M) with loss of hydrogen atom, we denoted as $M - \text{H}^+$.

3.5.4 *operando* X-ray absorption spectroscopy (XAS)

The reduction behavior and local atomic information of CuO_x NS during CO₂RR are followed by *operando* XAS at the Cu K-edge. This part of work is collaborated with Dr. Katharina Klingan, from the Free University of Berlin.

Results from *operando* XAS measurement on CuO_x NS are presented in Chapter 6.

Experimental Description

A few of materials are used as references. Reference powders of CuO (nanopowder, particle size < 50 nm, surface area 29 m²/g, Sigma Aldrich) and Cu(OH)₂ (Sigma Aldrich) were mixed and grinded with boron nitride and measured at 20 °C in absorption mode at the Cu K-edge with ionization chambers before and after the samples. Energy calibration was done by measuring simultaneously a Cu foil (0.001 mm, 99.999%, Goodfellow) and shifting the energy axis to the first fitted maximum of the derivative of the absorption of the Cu foil. The metal foil reference was measured in absorption mode as well.

CuO_x NS catalysts were prepared on 2x2.5 cm glassy carbon sheets (250 μm thickness, Sigradur K) and mounted in an in-house made electrochemical Teflon cell. *Operando* spectra of CuO_x NS samples were collected in fluorescence geometry from the backside of the glassy carbon electrode. We used a 13 element Si-drift energy resolving detector (RaySpec) which we equipped with an Al-shielding having a 25x25 mm Ni foil (0.00125 mm, 99.999%, Goodfellow) in front to suppress scattered light.

The electrochemical cell was controlled by an SP-300 potentiostat (Biologic). We used an Ag/AgCl reference electrode and a Pt coil as a counter electrode. The CuO_x area exposed to the electrode was 1.96 cm². The 0.1 M KHCO₃ electrolyte was purged throughout the experiment with ≈ 20 mL/min⁻¹. All potentials were compensated for 85% ohmic drop (R≈40 Ω).

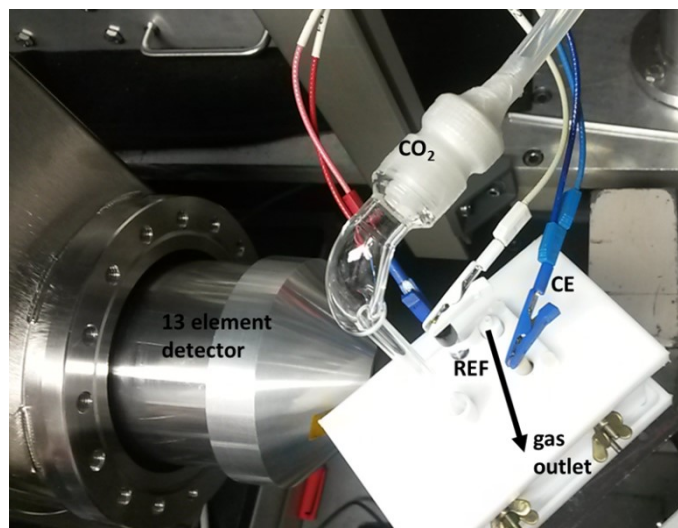


Figure 3.11 Photograph of *operando* XAS test station at Bessy (photo taken by Dr. Katharina Klingan).

We collected EXAFS spectra to $k_{12.2}$ within 6 min data acquisition time. The experimental protocol was the following:

1. Spectrum of dry film
2. Spectrum of film at open circuit potential (OCP)
3. LSV with 5 mV/s from -0.02 to $-0.84 V_{RHE}$
4. Spectra taken between 0 min to 130 min every 10 min while $-0.84 V_{RHE}$ was applied

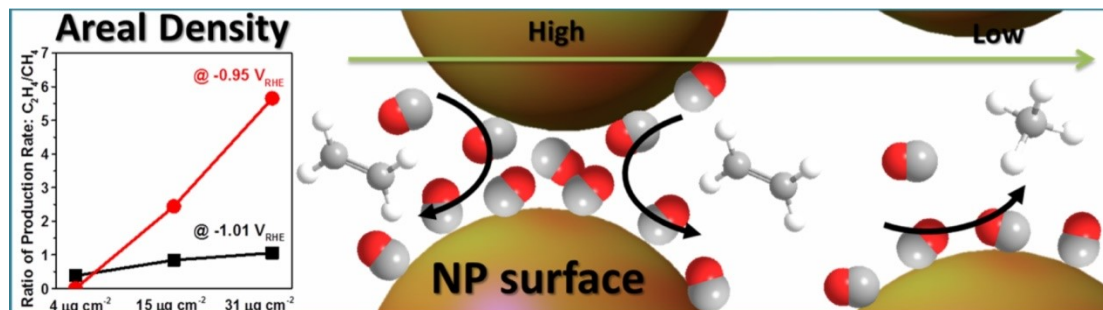
During 4. the beam shutter was closed after each spectrum (after 6 min data acquisition time) and three different sample spots have been used to protect the sample from radiation damage. The experimental protocol was repeated two times, and the three individual data sets have been averaged accordingly. Energy calibration was done by measuring before and after the experimental protocol a Cu foil and shifting the energy axis to the first inflection point of the fluorescence spectrum of Cu foil.

EXAFS simulations

The extracted spectra were weighted by k^3 and simulated in k -space. All EXAFS simulations were performed using in-house software (SimXLite) after calculation of phase functions with the FEFF program (version 8.4, self-consistent field option activated). Phase functions were calculated using geometries from open-access cif files of Cu, CuO, Cu(OH)₂, and the extracted cif files of CuO_x NS and Cu(OH)₂ from experimental XRD data. As usual, the EXAFS phase functions did not depend strongly on the details of the used model. Cosine windows covering 10% at the low- k and high- k side of the spectra were applied before

calculation of the Fourier transforms. An amplitude reduction factor (S_0^2) of 0.8 was used. The data range used in the simulation was 34.3-461.1 eV (3-11 \AA^{-1}). The Debye-Waller parameters for all shells were fixed to avoid overparameterization, and to emphasize the changes in coordination number of the samples. The fixed Debye-Waller parameters have been chosen as followed: CuO powder reference, Cu metal reference, and CuO_x NS (at OCP) spectra have been simulated with fixed coordination numbers. The so obtained Debye-Waller parameters have been used for the simulation of the respective shells. The EXAFS simulation was optimized by a minimization of the error sum obtained by summation of the squared deviations between measured and simulated values (least-squares fit). The fit was performed using the Levenberg-Marquardt method with numerical derivatives. The error ranges of the fit parameters were estimated from the covariance matrix of the fit, and indicate the 68 % confidence intervals of the corresponding fit parameters. The fit error was calculated as in reference¹¹⁷ For calculation of the Fourier-filtered error (described in reference¹¹⁸), the range from 1 to 6.5 \AA on the reduced distance scale was used.

Chapter 4 Catalyst particle density controls hydrocarbon product selectivity in CO₂ electroreduction on CuO_x



A key challenge of the carbon dioxide electroreduction (CO₂RR) on Cu-based nanoparticles is its low faradic selectivity towards higher-value products such as ethylene. Here, we demonstrate a facile method for tuning the hydrocarbon selectivities on CuO_x nanoparticle ensembles by varying the nanoparticle areal density. The sensitive dependence of the experimental ethylene selectivity on catalyst particle areal density is attributed to a diffusional interparticle coupling which controls the de- and re-absorption of CO and thus the effective coverage of CO_{ad} intermediates. Thus, higher areal density constitutes dynamically favored conditions for CO re-adsorption and *CO dimerization leading to ethylene formation independent of pH and applied overpotential.

Chapter 4 and its supplementary information section (Appendix A1) were reproduced with permission from [ChemSusChem, 2017, 10, 4642-4649](#). Copyright of The John Wiley and Sons (2017).¹²⁶

Xingli Wang, Ana Sofia Varela, Arno Bergmann, Stefanie Kühl and Peter Strasser, “Catalyst particle density controls hydrocarbon product selectivity in CO₂ electroreduction on CuO_x”, ChemSusChem, 2017, 10, 4642-4649.

P.S., X.W and A.S.V. conceived and designed the experiments. X.W. performed the experiments and analyzed the data, A.B. helped the Rietveld refinement of XRD patterns; S.K. recorded TEM images; X.W. and P.S. wrote the manuscript; all authors contributed to the discussions.

4.1 Synthesis and characterization

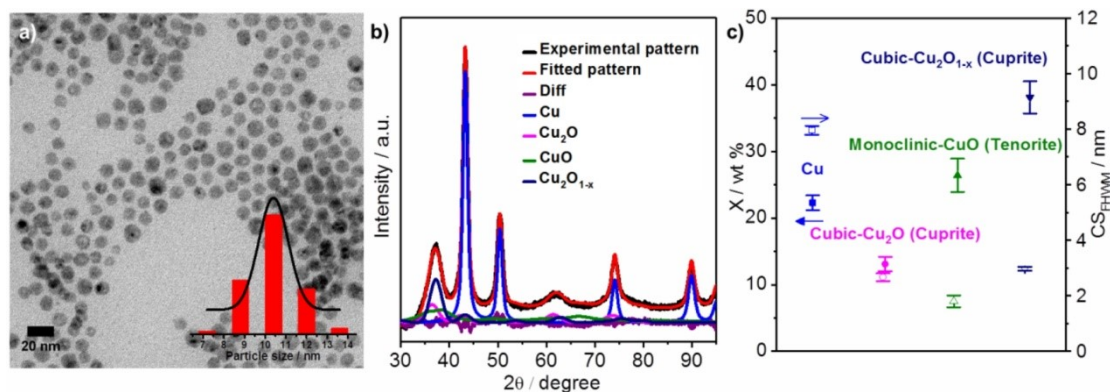


Figure 4.1 Physiochemical characterization of as-prepared CuO_x NPs. a) Representative TEM images of CuO_x nanoparticles. The inset shows the size distribution of CuO_x nanoparticles. b) Powder X-ray diffraction (XRD) of the CuO_x NPs catalysts between 30° to 95° degree. c) Weight fractions of solid phases (solid symbols, left axis of ordinates) and evaluated crystallite size (hollow symbols, the right axis of ordinates) for each phase.

We used a liquid-phase method to reduce Cu²⁺ precursors in organic solvents to obtain catalytically active copper oxide nanoparticles (CuO_x NPs) with controlled shape and narrow size distribution. Figure 4.1a shows representative TEM images of the as-prepared CuO_x NPs. The analysis revealed a monodisperse spherical morphology with an average diameter of 10.4±0.97nm. To avoid agglomeration of the as-prepared CuO_x NPs, they were stored as a suspension in hexane at room temperature. The TEM analysis of aged particle suspensions (Figure A1.1) indicated that the morphology (NP size: 10.23±1.02nm) and monodispersity remained stable for at least seven consecutive days.

To learn more about the type, number and ratio of the individual Cu oxide phases present in the NP ensemble, X-ray diffraction and Rietveld refinement were used. A typical XRD pattern of CuO_x NPs is shown in Figure A1.2 suggesting the presence of three crystal phases, namely metallic Cu, CuO and Cu₂O (see crystal structures of these phases in Figure A1.3). Rietveld refinement was employed to fit the experimental pattern, calculate phase fractions, lattice constants and oxygen occupancies (see Figure 4.1b, c). The results indicated the coexistence of 22.3±1.1wt% fcc structured metallic Cu, 13.1±1.1wt% cubic-Cu₂O, 26.4±2.5wt% monoclinic-CuO, as well as 38.1±2.4wt% of oxygen-defective Cu₂O_{1-x}. While the particle preparation was kept strictly air-free, the XRD analysis was performed under air

and thus we suspect that oxygen exposure of the metallic Cu particle surfaces may have contributed to the formation of the observed mix of passivating oxides. To explain the formation of the non-stoichiometric oxide, we note that adsorbed oxygen atoms on the surface of metal nanoparticles can enable the generation of oxidic surface compounds and facilitate metal ion diffusion across the particles, even at low temperature. The diffusion of Cu ions toward the particle bulk or surface may thus lead to non-stoichiometry and structural distortion of the crystal parameters. In the case of cubic $\text{Cu}_2\text{O}_{1-x}$ structure, revealed oxygen occupancy of only 0.593 ($\text{Cu}_2\text{O}_{0.593}$), indicating an incomplete diffusion of oxygen atoms inside the unit cells. Crystallite size and coherence length evaluations of the individual Cu, Cu_2O , CuO and $\text{Cu}_2\text{O}_{1-x}$ phases (Figure 4.1c) revealed the presence of $\sim 8\text{nm}$ metallic Cu, as well as 2-3nm cubic Cu_2O , monoclinic CuO and cubic $\text{Cu}_2\text{O}_{0.593}$ crystallites.

4.2 Electrochemical CO₂RR over CuO_x catalysts with various areal densities

To investigate their intrinsic catalytic CO₂ reduction activity under varying areal catalyst densities (reported in terms of catalyst mass per cm² geometric electrode surface area), the CuO_x NPs were coated on a flat supporting glassy carbon working electrode using three different loadings. All samples were tested in a two-compartment membrane-separated cell ("H-cell"), a three-electrode setup using CO₂-saturated 0.1M KHCO₃ as reactant and electrolyte. The electrolyte was kept under CO₂ bubbling throughout the experiments at a constant flow of 30sccm (standard cubic centimeter per minute).

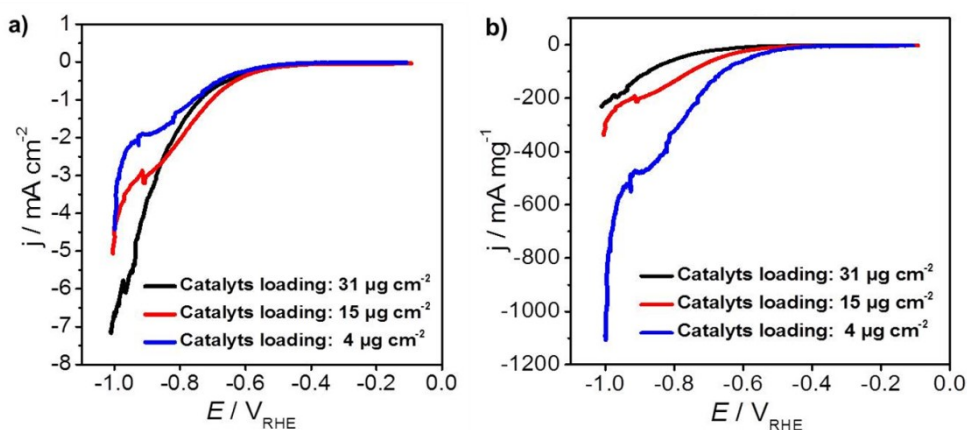
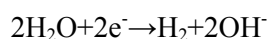
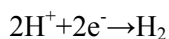


Figure 4.2 Catalytic activity represented by linear sweep voltammograms taken at 5 mV/s in CO₂-saturated 0.1 M KHCO₃ for 4 μg cm⁻², 15 μg cm⁻², 31 μg cm⁻² CuO_x NPs areal densities, catalyst layers were supported on glassy carbon. Catalytic activity expressed in terms of a)

geometric area-normalized current densities and b) catalyst NP mass-normalized current densities.

The current densities normalized by geometric surface areas of the supporting electrode are reported in Figure 4.2a. For all catalyst densities, reductive catalytic currents associated with hydrogen evolution and CO₂ reduction emerged at potentials more negative than -0.6V_{RHE} (RHE: reversible hydrogen electrode) with an apparent exponential potential dependence. Around -0.9V_{RHE}, the small and medium areal-particle-density scans exhibited somewhat declining j-E slopes (activity shoulder) before all three potentiodynamic scans return to rapid exponential growth. At potentials more negative than -0.8V_{RHE}, bubble formation and detachment of H₂, CH₄, and C₂H₄ gases started to become significant and caused a noisy current signal. Although geometric current densities represent the performance of the electrode layer structures, real surface area-normalized or catalyst mass-normalized current densities are more suitable to compare electrocatalyst performance on an intrinsic materials characteristic. For monodisperse-size-distributed and homogeneous NP catalysts, mass- and real surface area-based performance data are equivalent. This is why we shall consider intrinsic catalytic activities and faradaic product yields on a catalyst-mass basis. Figure 4.2b shows the corresponding mass-normalized current density scans from -0.1 to 1.0V_{RHE}. Now the scans suggested an inverted activity trend with the highest areal density (31 μg cm⁻²) displaying the lowest catalyst mass-based current density. This evidences that the interfacial charge transfer did not linearly scale with catalyst areal density. In other words, at higher catalyst loadings, processes and conditions emerge that limit interfacial charge transfer. We associate these with mass-transport limitations of CO₂ to the electrified catalyst NP surface possibly linked to local pH increases owing to the hydrogen evolution reaction from protons or water, as discussed below, according to:



To get insight in the Faradic competition between hydrogen evolution and CO₂ reduction at varying areal catalyst densities, we considered the absolute product yields (catalyst mass-based production rates) and associated short-term Faradaic efficiencies (FE). To this end, we performed bulk electrolysis at constant electrode potentials and analyzed the reaction

products after 15 min. Details about the chromatograph based efficiency analysis method are provided in the Supporting Information. Figure 4.3 displays the mass-normalized absolute production rates of the four major gas products. As the areal catalyst density increased from $4 \mu\text{g cm}^{-2}$ to $15 \mu\text{g cm}^{-2}$ and $31 \mu\text{g cm}^{-2}$, so decreased the H_2 formation rate exhibiting a rather flat logarithmic production (black symbols in Figure 4.3a-c). More importantly for our discussion here, the areal CuO_x catalyst nanoparticle density evidenced a clear effect on the hydrocarbon product yields during the CO_2RR . In particular, the CH_4 and C_2H_4 production rates revealed opposite trends with particle density: the production rate of C_2H_4 strongly increased, whereas that of CH_4 decreased. Note also that the onset potential of C_2H_4 production at around $-1.0 \text{ V}_{\text{RHE}}$ for the low areal density experiment shifted strongly anodically (smaller overpotentials) by about 100 mV with higher areal density ($15 \mu\text{g cm}^{-2}$ and $31 \mu\text{g cm}^{-2}$). Such a density-dependent onset potential shift was not observed for the CH_4 formation.

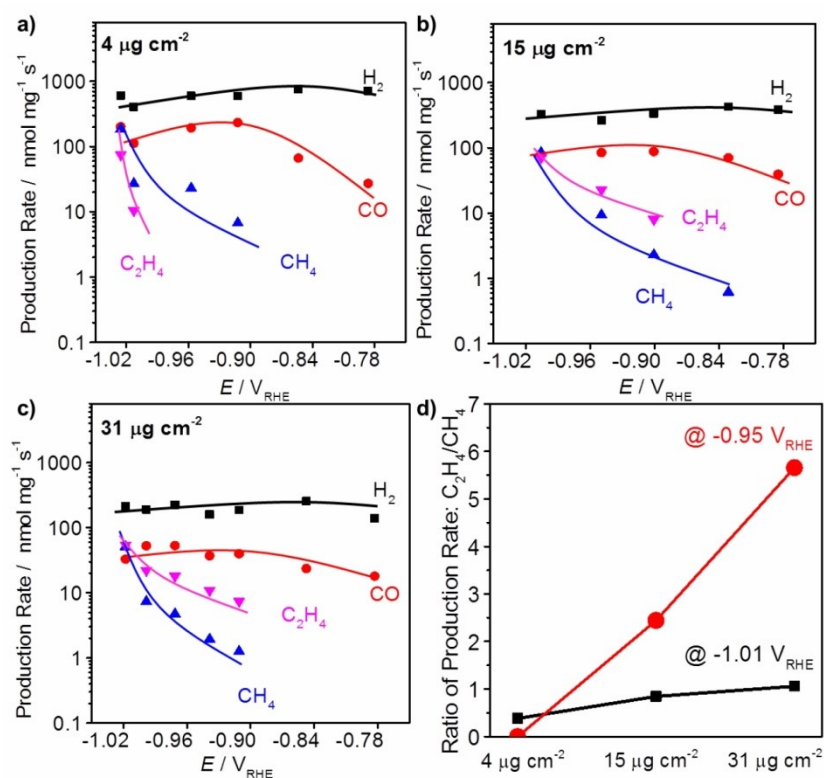


Figure 4.3 Catalyst mass-normalized absolute product formation rates of major gaseous products as a function of applied electrode potentials during CO_2 electroreduction in CO_2 -saturated 0.1 M KHCO_3 at CuO_x nanoparticle catalyst areal densities of a) $4 \mu\text{g cm}^{-2}$, b) $15 \mu\text{g cm}^{-2}$, c) $31 \mu\text{g cm}^{-2}$. d) Trends in $\text{C}_2\text{H}_4/\text{CH}_4$ production ratio at varying catalyst areal densities at $-0.95 \text{ V}_{\text{RHE}}$ and $-1.01 \text{ V}_{\text{RHE}}$ applied electrode potential. Potentials are IR corrected.

Figure 4.4 shows the production rate-derived Faradaic efficiencies (FEs) of the major gas products over the applied electrode potential. Regardless of the areal density, the H₂ evolution reaction is clearly preferred at low overpotentials but shows steadily decreasing FE values with higher overpotentials up to -1.0 V_{RHE}. Significant FE values of CH₄ and C₂H₄ emerge at applied potentials more negative of -0.84 V_{RHE}. Consistent with the data in Figure 4.3, the FE of CH₄ drops with higher areal densities in favor of that of C₂H₄. Linked with these trends are the FE values of CO that remained lower with catalyst density. The total FEs towards gaseous products and liquid products for CO₂RR and HER are shown in Figure A1.4.

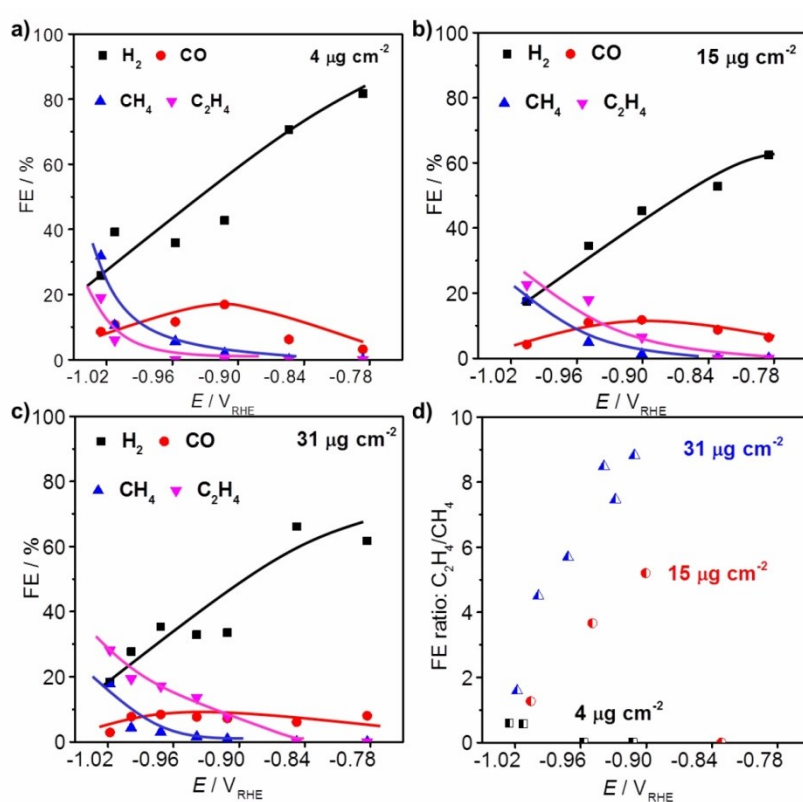


Figure 4.4 Faradaic efficiency for each product as a function of areal density at various applied overpotentials. Faradaic efficiency of CO₂ electrochemical reduction over a) $4 \mu\text{g cm}^{-2}$, b) $15 \mu\text{g cm}^{-2}$, c) $31 \mu\text{g cm}^{-2}$. d) The Faradaic efficiency ratios of C₂H₄/CH₄ versus overpotential for the different areal densities.

The stability of the CuO_x NP ensembles was evaluated at -1.0 V_{RHE} over 400 minutes at the areal catalyst density of $31 \mu\text{g cm}^{-2}$ which has the largest absolute C₂H₄ production rate. As shown in Figure 4.5a, the overall faradaic current dropped 40% during the first 150mins (Region 1) and then levelled out at -4 mA cm^{-2} (Region 2). The partial current densities of the major CO₂ reduction products, CH₄ and C₂H₄ (see Figure 4.5b), followed that overall current

trend. All three C_1 and C_2 based partial currents together accounted for about 50% of the total faradaic charge over the test time. These trends were mirrored by the absolute molar production rates of the gaseous products (see Figure 4.5c). The total Faradaic efficiencies for both gaseous and liquid products are shown in Figure A1.5, which can reach 99.3% in the end. Hence, the unbalanced charge at various overpotentials shown in Figure 4.4 is mainly attributed to the liquid products.

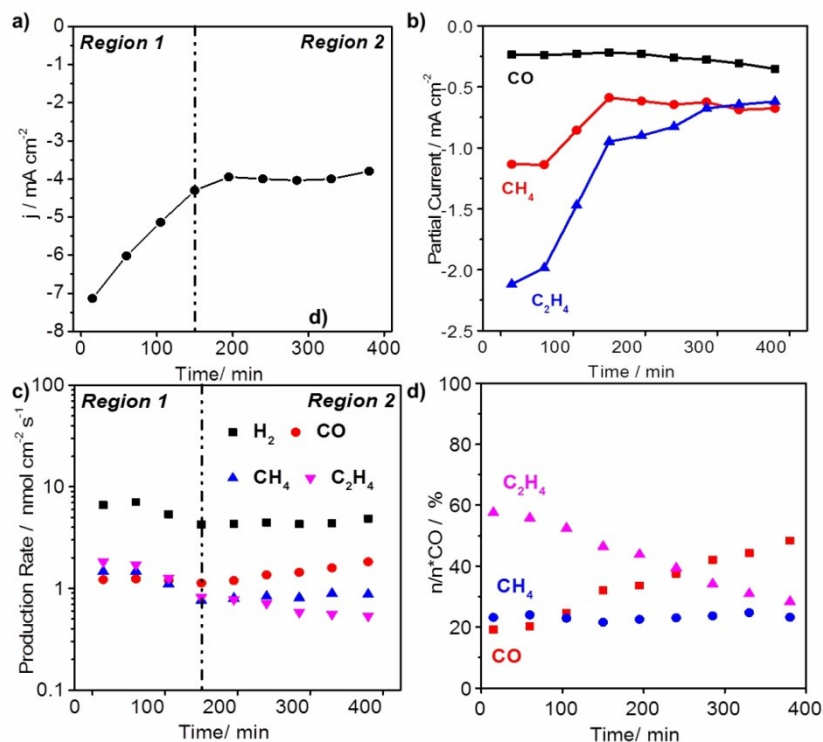
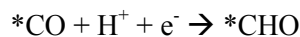


Figure 4.5 a) Chronoamperometric performance stability of the CO₂ reduction reaction on CuOx NPs in CO₂-saturated 0.1 M KHCO₃ at $-1.0 V_{RHE}$. b) Partial current densities of CO, CH₄, C₂H₄. c) Absolute product formation rates of gaseous products over time. d) The consumption ratio of *CO for CO, CH₄, C₂H₄, respectively. Catalyst areal density: 31 $\mu\text{g cm}^{-2}$.

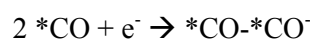
4.3 Discussions

The observed correlation between catalyst particle areal density (geometric loadings) and product yields can be plausibly rationalized in terms of the local concentrations of reactants at the electrified particle surfaces, and their effect on the rates of elementary chemical reactions. In light of prior work on the CO₂ reduction mechanism adsorbed CO, denoted as *CO, serves as a common intermediate of the reaction pathway toward methane and ethylene. After the $2e^-$

reduction of CO₂ to *CO, the latter may desorb, form gaseous CO_(g) and diffuse into the electrolyte. Alternatively, *CO may undergo subsequent stepwise proton-coupled electron transfer (hydrogenation steps) to *CHO,

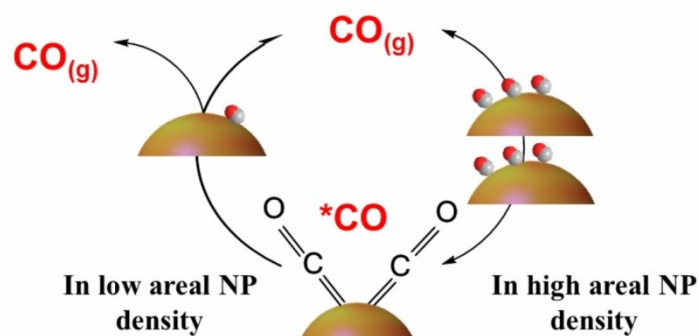


Followed by reaction to *CHOH or *CH₂O, *CH₂OH or possibly to CH₂O* and finally to CH₄. In a competing process, *CO was proposed to dimerize in a proton de-coupled electron transfer according to



Opening a C₂ pathway toward C₂H₄ via a decouple proton-electron transfer step. Clearly, the rate of this dimerization depends on the surface coverage of *CO. Now, a larger areal catalyst density decreases the mean interparticle distance between individual CuO_x NPs and increases the absolute number of electrochemical surface active sites. This is because the CuO_x NPs were applied directly as unsupported metal oxide particles lacking any volume-controlling carrier matrix, such as for instance a porous carbon. The nonlinear scaling of catalyst particle areal densities and geometric currents (see Figure 4.2a) is another indication that reactant mass transfer rates were negatively affected by larger areal catalyst densities. At reduced mean particle distances it is plausible that desorbed CO_(g) molecules are more likely to re-adsorb on the surface of nearby Cu particles rather than leaving the catalyst film as CO gas; this increases the stationary mean coverage of adsorbed *CO on the catalyst surface. At meanwhile, real-surface area in the dense areal particle density also increases the absolute active sites for *CO. As a result of this, the reaction rate along the C₂ pathway toward ethylene would be kinetically preferred as it is second order in CO coverage compared to the methane pathway (see Scheme 4.1). Indeed, as Figure 4.3d demonstrates, the ratio of C₂H₄ to CH₄ production rate more than doubles from 0.38 at areal density of 4 μg cm⁻² to 0.84 at 15 μg cm⁻², and finally almost triples to 1.06 at an areal density of 31 μg cm⁻² and an overpotential of -1.0 V_{RHE}. This trend is even more obvious at -0.95 V_{RHE}, where the ratio of C₂H₄ to CH₄ production rate increases dramatically from 0 to 2.44 and 5.65. Similar trends were discernible in the areal density-dependence of the FE ratio of C₂H₄ and CH₄ (FE_{C₂H₄}/FE_{CH₄}), a performance figure related to the charge efficiency of ethylene production. As shown in Figure 4.4d, the (FE_{C₂H₄}/FE_{CH₄}) ratio rose with the areal catalyst density values

within the given overpotential range. High areal catalyst densities associated with smaller mean interparticle distances showed favorable charge efficiencies for C₂H₄ production.



Scheme 4.1 The favored pathway for *CO in low/high areal NP densities condition. In low areal particle density, *CO tends to leave as CO(g); while in high areal NP density, the desorbed CO(g) molecules are more likely to re-adsorb on the surface of nearby Cu particles.

As mentioned before, high areal particle density affects reactant mass transport to the catalytic surface, as well, and typically decrease the local concentration in CO₂ and protons, reflected in observed reduced hydrogen yield per mass of catalysts. However, our data suggest that even if local depletion of CO₂ occurs at higher areal catalyst density, it does not appear to be able to offset the kinetic benefit of enhanced *CO re-adsorption. The local depletion of protons, or equivalently the accumulation of local OH⁻ due to hydrogen evolution and CO₂ reduction, on the other hand, can result in increased local interfacial pH values. As the reductive *CO dimerization reaction is believed to be proton-decoupled, it would not be affected by a change in local pH while the competing reactions would. As a result, one would expect a constant production rate of C₂H₄. As our experiments (Figure 4.3) revealed enhanced C₂H₄ formation rates over CH₄ (constant overpotential on SHE scale) with areal density, a local pH effect can be ruled out. The selectivity of one additional catalyst areal density of 100 μg cm⁻² is shown in Figure A1.6. The ratio of C₂H₄ to CH₄ production rate (0.98) is similar to the one of 31 μg cm⁻² (1.05). Considering that most nanoparticles tend to overlap with each other in dense condition leading to a steady mass transport state, the catalyst areal density cannot be increased infinitely to improve the hydrocarbon selectivity.

Recalling that the formation pathways of the three gas products $\text{CO}_{(\text{g})}$, CH_4 and C_2H_4 , involve adsorbed CO molecules ($^*\text{CO}$) as a common intermediate, a simple stationary mass balance relation reads

$$n_{^*\text{CO}} = n_{\text{CO}} + n_{\text{CH}_4} + 2 \times n_{\text{C}_2\text{H}_4}$$

Where n denotes the consumed or produced molar amount per time of each product. From this, a carbon reaction pathway selectivity ($n_i/n_{^*\text{CO}}$) can be derived (Figure 4.5d) that expresses the reactive preference of each product. It is evident that the $^*\text{CO}$ to C_2H_4 pathway declines strongly, while more and more $^*\text{CO}$ simply desorbs and forms molecular CO. The proportion of $^*\text{CO}$ for CH_4 formation remains essentially constant. These trends suggest that the catalyst or operation conditions during the test time vary such that the dimerization/hydrogenation of $^*\text{CO}$ to ethylene is hindered, while that of generating methane is unaffected.

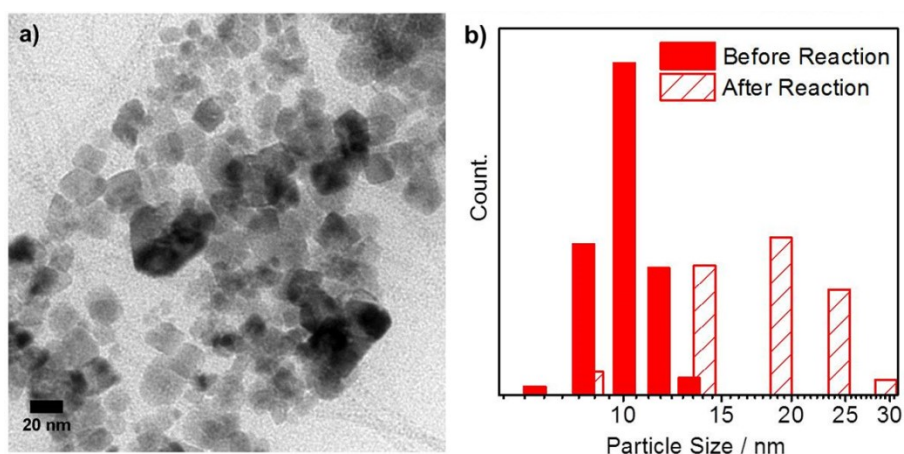


Figure 4.6 a) TEM image of CuO_x nanoparticles after the chronoamperometric stability test at $-1.0 V_{\text{RHE}}$ from Figure 4.5. b) The mean particle size after 400 min significantly increased compared to Figure 4.1a. Catalyst areal density: $31 \mu\text{g cm}^{-2}$.

In order to assess reasons for the stability trends, we investigated the particle morphology of the CuO_x NPs after the electrolysis at $-1.0 V_{\text{RHE}}$ after 400 min. As shown in Figure 4.6a, particle growth and sintering to a mean size of $(18.1 \pm 0.28 \text{ nm})$ was apparent (c.f. Figure 4.1a-b). This may occur by catalyst particle migration and coalescence and/or by free energy difference-driven Ostwald ripening. In the former sintering mode, the translational motion of entire nanoparticles leads to the collision and coalescence with neighboring particles. The latter growth mode involves the dissolution of atomic monomers, diffusion and re-deposition

on larger neighboring particles. The sintering process slows down as particles grow in size and interparticle distances increase.¹¹⁹ We are inclined to associate the dramatic decline in Faradic current during the first 150 mins of stability test with catalyst ripening and aging processes, before the faradic current levelled out in region 2 where the particle size distribution remained time stable. During the particle aging, the mean interparticle distance must have increased to the point where the kinetic *CO-reabsorption and reductive dimerization advantage on particles in close proximity was lost. *CO was now more likely to desorb and diffuse away as CO_(g) rather than re-absorb and dimerize to ethylene. Consistent with this view, the methane pathway and production rate remained essentially unaffected (note the logarithmic scale in Figure 4.5c). In summary, we believe that under our current conditions the particle size-dependent interparticle distance played the key role for the evolution of the faradaic product efficiency. At the same time, the real electrochemical active surface area of the CuO_x NPs declined and resulted in a decrease in the overall current density. The influence of a lower local pH at lower current densities (the reverse pH-ethylene correlation discussed above) appears limited, as it would affect all proton-consuming reaction rates.

4.4 Conclusions

In summary, we prepared unsupported CuO_x NP ensembles, deployed them in the form of NP layers, and demonstrated that tuning of the product distribution during catalytic CO₂ electroreduction was possible by simply adjusting the areal particle density. Increasing the areal NP density decreased the mean interparticle distances and increased the total surface active sites as deduced from geometric voltammetric current scans and TEM imaging. A shift in faradic efficiency towards C₂H₄ over CH₄ at higher areal density was observed. This observation was attributed to higher reductive dimerization rates of adsorbed *CO at smaller interparticle distances, thanks to enhanced CO_(g) re-adsorption on NP in close proximity. Enhanced re-adsorption caused higher mean surface coverages of *CO and higher kinetic ethylene formation rates ensued. Catalytic performance tests over extended reaction times corroborated the role of interparticle distances. Over other strategies to tune catalytic CO₂

reduction reaction product yields, such as varying the catalyst composition or electrolyte, adjusting the catalyst density appears relatively facile.

Chapter 5 Mechanistic Reaction Pathways of Enhanced Ethylene Yields during Electroreduction of CO₂-CO co-Feeds on Cu and Cu-Tandem Electrocatalysts

Unlike energy efficiency and selectivity challenges, the kinetic effects of impure or intentionally mixed CO₂ feeds on the catalytic reactivity of the direct electrochemical CO₂ reduction reaction (CO₂RR) have been poorly studied. Given that industrial CO₂ feeds are often contaminated with CO, a closer investigation of the CO₂RR under CO₂/CO co-feed conditions is warranted. Here, we report mechanistic insights into the CO₂RR reactivity of CO₂/CO co-feeds on Cu-based nanocatalysts. Kinetic isotope-labelling experiments—performed in an operando differential electrochemical mass spectrometry capillary flow cell with millisecond time resolution—showed an unexpected enhanced production of C₂H₄, with a yield increase of almost 50%, from a cross-coupled ¹²CO₂–¹³CO reactive pathway. The results suggest the absence of site competition between CO₂ and CO molecules on the reactive surface at the reactant-specific sites. The practical significance of sustained local interfacial CO partial pressures under CO₂ depletion is demonstrated by (non-)metallic/metallic tandem catalysts. Our findings show the mechanistic origin of improved C₂ product formation under co-feeding, but also highlight technological opportunities of impure CO₂/CO process feeds for H₂O/CO₂ co-electrolysers.

Part of chapter 5 and its supplementary information section (Appendix A2) were reproduced with permission from [Nat. Nanotechnol., 2019, 14, 1063-1070](#). Copyright of Springer Nature.¹²⁷

Xingli Wang, Jorge Ferreira de Araújo, Wen Ju, Alexander Bagger, Henrike Schmies, Stefanie Kühn, Lujin Pan, Jan Rossmeisl and Peter Strasser, “Mechanistic Reaction Pathways of Enhanced Ethylene Yields during Electroreduction of CO₂-CO co-Feeds on Cu and Cu-Tandem Electrocatalysts”

X.W., J.A. and P.S. conceived and designed this project and co-wrote the manuscript. X.W. carried out the materials synthesis, characterization and electrochemical evaluation. J.A. conducted the DEMS measurement and analyzed the results. W.J. and A.B. participated in the discussion of electrochemical and mechanism sections. H.S. performed the HE-XRD measurement and provided the help of data analysis. X.W. and S.K. performed the TEM characterizations. L.P. contributes to the electrochemical tests for CuO_x-Ag catalysts. All authors read and commented on the manuscript.

5.1 Synthesis and characterization

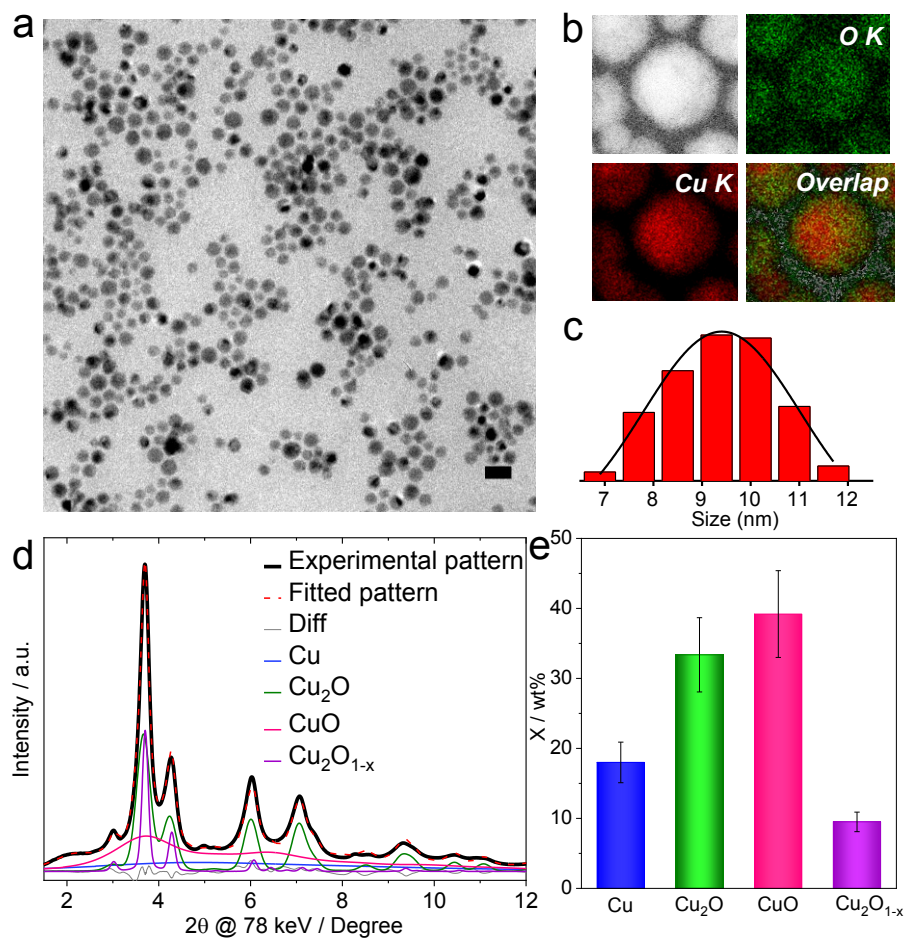


Figure 5.1 Morphological, structural, elemental and physical characterizations of CuO_x NPs synthesized in this study. a) Representative TEM images of CuO_x nanoparticles. b) EDX mapping images of CuO_x NPs. c) Size distribution of CuO_x NPs. d) Powder X-ray diffraction (XRD) of the CuO_x NPs catalysts with Rietveld refinement. e) Weight fractions of the solid phases.

For our investigation of the kinetics, product yields and mechanistic pathways of the electrochemical CO₂ reduction reaction (CO₂RR) under CO/CO₂ co-feeding conditions, spherical Cu-oxide nanoparticle catalysts were prepared and utilized (See Session 3.11) with an extra drying process in Frozen dryer. We note that this report is not concerned with the dynamics of the chemical state of the Cu catalyst under CO/CO₂ co-feeding, which is why we refrained from in-depth *operando* analytics of the operating catalysts. Yet, to reveal the initial characteristics of the Cu catalyst employed, Figure 5.1a-c displays transmission electron microscopy (TEM) images, particle size distributions and scanning transmission electron microscopy / X-ray energy dispersive spectroscopy (STEM/X-EDS) elemental maps of the

spherical CuO_x nanoparticles (CuO_x NPs). The unsupported CuO_x NPs with their narrow size distribution of 9.4 ± 1.1 nm (Figure 5.1c) were synthesized using a liquid-phase, ambient pressure route under N_2 atmosphere, followed by self-oxidation upon exposure to air at room temperature. The elemental maps of the NPs in Figure 5.1b evidenced an oxygen-rich region near the surface of the CuO_x NPs. Metallic Cu was present and preserved in the center of the NPs due to the passivating effect of the outer Cu oxide layer. Rietveld refinement-based phase analyses of synchrotron WAXS patterns confirmed the presence of non-stoichiometry and structural distortion of the crystal parameters, and allowed the extraction of the exact type, number, and ratio of the individual Cu oxide phases present in the NP ensemble. Pattern deconvolution displayed in Figure 5.1d revealed the co-presence of three crystal phases, namely $18.0 \pm 2.9\text{wt}\%$ of fcc structured metallic Cu, $33.4 \pm 5.3\text{wt}\%$ of cubic- Cu_2O and $39.2 \pm 6.2\text{wt}\%$ of monoclinic- CuO . The oxygen occupancies were also refined in the crystal phases, revealing oxygen occupancy of only 0.821 in $\text{Cu}_2\text{O}_{1-x}$, indicating an incomplete diffusion of oxygen atoms inside the unit cells.

5.2 Feeding gases control

5.2.1 In H-cell design

As the working component of H-cell is sealed tightly, the partial pressure of CO_2/CO gas can be adjusted by controlling the individual gas flow rate when the total flow rate is kept at 30 sccm constantly. With the increased amount of CO co-feeding, the feed-gas-ratio is tuned from 2:1 (CO_2 to CO), 1:1 to 1:2. Accordingly, the concentration of CO_2 or CO in the electrolyte will be dependent on the partial pressure of the gases in the atmosphere (298 K, 101.3 KPa).

In pure CO_2 condition, $c(\text{CO}_2) = 1/K_{\text{Henry-CO}_2} * P_{\text{CO}_2} = 33.6$ mM

In pure CO condition, $c(\text{CO}) = 1/K_{\text{Henry-CO}} * P_{\text{CO}} = 0.95$ mM

Table 5.1 Gas flow control of various feeds and their relevant ratios of dissolved CO_x species according to Henry's law.

CO ₂ Flow (sccm)	CO Flow (sccm)	Volumn (mL)	Con. CO ₂ (mmol)	Con. CO (mmol)	CO ₂ (aq):CO (aq) Ratio
30	0	40	1.344	0	-
20	10	40	0.892	0.013	69:1
15	15	40	0.672	0.019	35:1
10	20	40	0.448	0.025	18:1
0	30	40	0	0.038	-

5.2.2 In DEMS flow cell

Instead of controlling the dissolved CO_x species by flow gas partial pressure in H-cell, it can be achieved by a home-made mixer (see Session 3.5.3) in DEMS setup as well.

Table 5.2 Electrolyte flow control of various feeds and their relative ratios of dissolved CO_x species in DEMS setup.

Saturated Electrolyte Flow rate CO ₂ : CO	CO ₂ (aq): CO (aq) Ratio
1:1	31:1
1:3	12:1

5.3 Electrocatalytic rates and product yields under pure and mixed CO₂/CO co-feeds

We now turn to the electrochemical kinetics of the CuO_x NPs under pure CO₂ feeds, pure CO feeds and CO₂/CO co-feeds at constant total mass flow in buffered neutral (pH=6.8) electrolytes evaluated in a two-compartment, membrane reactor cells. Using Henry's law, the molar amounts of dissolved CO and CO₂ in the electrolyte were calculated for each feed condition and are plotted in Figure 5.2a. Clearly, the effective total molar amount of dissolved

CO_x (CO and CO_2) in the electrolyte decreases with increasing CO partial pressures (Table 5.1). As the NP catalyst loadings were kept constant in all experiments, any effects regarding surface roughness could be ruled out in our analysis and discussion. To assess the catalytic activity and selectivity of the CO/ CO_2 reduction process, we measured the electrochemical CO_x reduction rates under the chosen CO_2 -CO co-feeds under steady-state conditions at constant potential electrolysis at $-1.0 V_{\text{RHE}}$ for multiple hours at room temperature. Figure 5.2b-c displays the time trajectories of absolute production rates of ethylene and methane during the tests. CH_4 production rates strongly depended on feed compositions and followed the order $\text{CO} > \text{CO}_2\text{-CO (co-feed)} > \text{CO}_2$. Data revealed that methane production rates were closely correlated with the experimentally determined H_2 production rate (see Figure A2.1), indicating a possible direct dependence of CH_4 formation on the reactant redox state, the available surface $^*\text{H}$ coverage, and local proton concentration. The six-electron CO-to- CH_4 reaction cascade is expected to proceed faster than the 8-electron pathway starting from CO_2 . Further, the dominant hydrogen evolution under pure CO feed conditions can be explained by higher local pH values under reaction conditions combined with low CO solubilities. Key to our discussions here, the C_2H_4 formation rates were significantly promoted under CO_2/CO mixed feeds. Control measurements confirmed that any CO_2/CO feed ratio invariably benefited the ethylene yield (Figure 5.2d). Yields of a number of other relevant liquid products formed during CO_2/CO co-feeding are shown in Figure A2.2 and Figure A2.3. Upon a $2e^-$ reduction, either formate, HCOO^- , or adsorbed CO, denoted henceforth as $^*\text{CO}$, was formed in all feeds containing CO_2 . Under co-feeding, the partial production rate of HCOO^- was proportional to the CO_2 partial pressure, while, obviously, no HCOO^- could be formed in pure CO feeds. Unlike the terminal $2e^-$ reaction pathway to HCOO^- , $^*\text{CO}$ may desorb to molecular gaseous $\text{CO}_{(\text{g})}$ or alternatively, undergo subsequent stepwise proton-coupled electron transfer pathways to CH_4 or alternatively may dimerize in a proton de-coupled electron transfer pathway to C_2H_4 . The overall production rate of both, CH_4 and C_2H_4 (referred to here as the “hydrocarbon rate”), is plotted in Figure 5.2d, as well. It shows the lowest value in pure CO_2 feeds, in part because the HCOO^- production rate was highest. With increasing CO in the feed, the HCOO^- pathway decreased, while the hydrocarbon yield sharply increased by about 50%, despite lower solubility of CO and, hence, a lower total CO_x

electrolyte concentration. Thus, CO_x solubility arguments obviously fail to account for the observed increase in C_2H_4 yields under co-feeding. Earlier studies revealed that pure CO feeds favored proton accessibility to reactive adsorbed intermediates, and, as a result of this, concluded that C_2H_4 formed via a hydrogenated dimer ($^*\text{CO-COH}$) generated in a consecutive electron-proton McMurry coupling-type transfer at moderate overpotentials, which constituted a distinct reaction channel from the CH_4 generation pathway. This is why we are inclined to attribute the observed higher CH_4 production rates in CO-containing feeds to a more favorable proton affinity to $^*\text{CO}$, as well. Figure 5.2e displays a volcano-type trend between ethylene production rate and CO_2 partial pressure. The vastly different slopes of the relation at small and large CO_2 partial pressures clearly suggest the existence of an optimum CO_2 to CO co-feed ratio that exhibits maximum C_2H_4 yields.

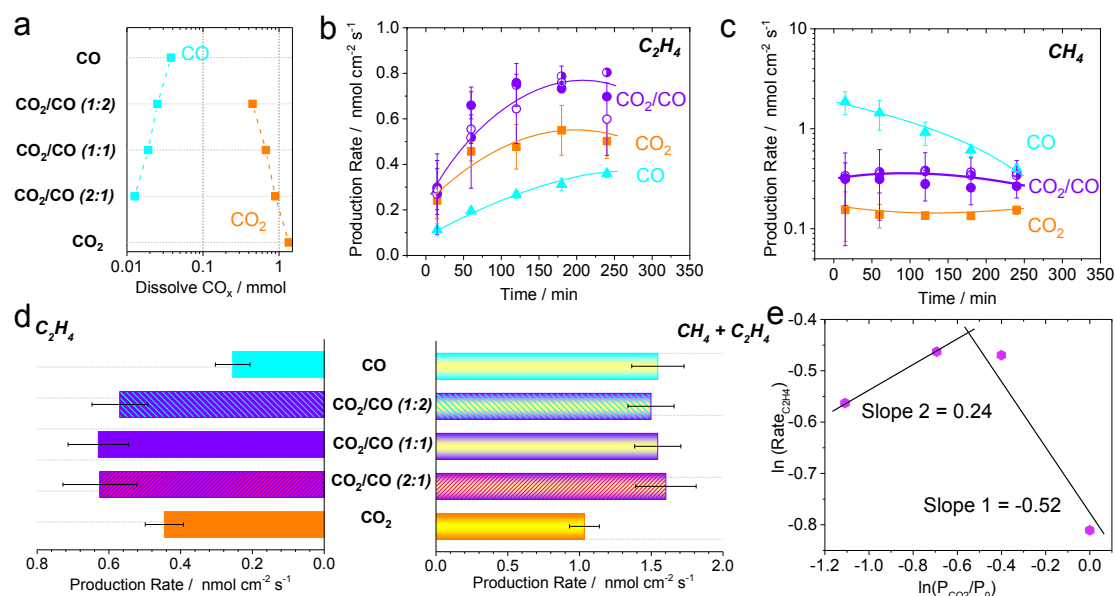


Figure 5.2 Catalytic performance detected by on-line GC in H-cell. a) The molar mass of dissolved CO_2 (aq) and CO (aq) in the 40 mL electrolyte with various feed gases according to Henry's law at 1 atm 25 °C. The total flow rate of feed gases used in all experiments is 30 sccm. Time-dependent absolute product formation rates on b) C_2H_4 and c) CH_4 at ~ -1.0 V_{RHE}. Orange: CO_2RR in CO_2 saturated 0.1 M KHCO_3 (pH=6.8); cyan: CORR in 0.1M $\text{K}_2\text{HPO}_4/\text{KH}_2\text{PO}_4$ (pH=6.9); Violet: co-feeds (CO_2/CO) reduction reductions in CO_2 saturated 0.1 M KHCO_3 . Catalyst loading: 100 $\mu\text{g cm}^{-2}$ on glassy carbon. d) C_2H_4 production rate (left) and carbon rates on hydrocarbons ($\text{CH}_4 + \text{C}_2\text{H}_4$) (right) with various feed gas ratios after 4h. CO_2 to CO partial pressure ratios in co-feed vary from 2:1, 1:1 to 1:2, leading to the ratios on dissolved CO_2 (aq) to CO (aq) in the electrolyte from 69:1, 35:1 to 18:1. e) $\ln(P_{\text{CO}_2})$ vs. $\ln(\text{Rate}_{\text{C}_2\text{H}_4})$. The error bars are given as standard error of the mean.

We then focused on the hydrocarbon yield in 1:1 CO₂/CO co-feeds as well as pure feeds over a wider electrode potential range (Figure A2.4). Favorable CH₄ production / H₂ production with CO-containing feeds were observed over the entire electrode potential range investigated, supporting our earlier mechanistic conclusions from Figure 5.2d and Figure A2.1. In CO₂/CO co-feeds, the experimental C₂H₄ yields first tracked those of pure feeds, until, at potentials cathodic of -0.93 V_{RHE}, they sharply outperformed them unfolding their kinetic benefits. In pure CO feeds, the C₂H₄ yields remained low, suggesting a CO mass-transport limitation consistent with the low CO solubility and local CO concentration at the interface.

After 2 and 4 h of electrocatalytic CO_x reduction catalysis at constant applied electrode potentials, we tracked the changes in the crystalline states and morphology of the initial CuO_x NPs. Data in (Figure A2.5, A2.6, A2.7) evidenced that under pure feeds the resulting Cu phases and particle morphologies were very similar under either pure feed. The oxidized copper phases vanished and transformed into a crystalline metallic Cu phase in both reduction processes, accompanied by a very similar particle agglomeration for all feeds. This led us to conclude that the observed differences in the catalytic ethylene yields have indeed more likely kinetic mechanistic roots, and do not arise from catalyst-related chemical factors.

We also investigated the influence of the pH value on the CO_x electroreduction kinetic in pure CO_x feeds (Figure A2.8), and we found that the C₂H₄ formation, unlike CH₄, from pure CO feeds behaved pH-independent on the SHE scale (Figure A2.8c), suggesting a proton-decoupled rate determining electron transfer step.^{74, 75} The C₂H₄ production exhibits an uphill trend in CO₂RR and slightly downhill trend in CORR, suggesting that the C-C coupling is limited by CO mass transport.

5.4 Discussions

Recalling the enhanced C₂H₄ production in co-feed in the more negative potential region, which is even more obvious than CO₂RR, it indicates that the extra CO in the CO₂ gas may help to break the mass-transport-limitation. Unlike the pure feed conditions, C₂H₄ in co-feed condition may originate from CO-CO combination, CO₂-CO₂ combination or crossed CO-CO₂ combination (see Figure 5.3). In order to validate this hypothesis, we tracked and

quantified the origin of carbon sources by labelling one of the carbons from co-feed species by using electrochemical capillary DEMS flow cell.

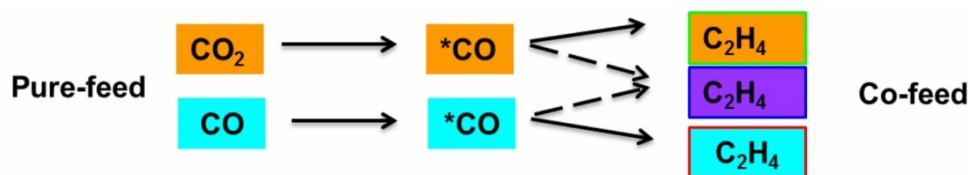


Figure 5.3 The possible carbon origins in pure feeds and co-feed during our DEMS experiments. In co-feed condition, carbon origins could go through “CO₂-CO₂” combination, “CO-CO” combination and/or crossed “CO₂-CO” combination pathway to C₂H₄.

Quantitative deconvolution of competing mechanistic C₂H₄ formation pathways

Under CO₂/CO co-feed conditions, the detected C₂H₄ product molecules originate from the dimerization of two CO species that must be located in atomic proximity. The CO species may originate from either only CO (here referred to as the “CO-CO” pathway), or from only CO₂ (here referred to as the “CO₂-CO₂” pathway) feed molecules, or else have a mixed origin, that is, one *CO derived from CO, while the other *CO was from CO₂ (referred to as cross coupling “CO₂-CO” pathway). The initial concentration ratios of dissolved CO_x (CO and CO₂) in the electrolyte and at the reactive interface are listed in Table 5.2. To obtain a more detailed mechanistic understanding of the enhancement mechanism of the ethylene production in co-feeds, we developed and utilized a novel *operando* DEMS set up (Figure 3.8) equipped with a newly designed CO₂RR capillary cell with a time resolution of ion mass current dynamics in the milli-second range. This technique enabled us to track and quantify the atomic origins of the two individual carbon atoms in the ethylene product molecules under the two pure and mixed CO₂/CO co-feeds. We achieve this by using isotope-labelled ¹³CO in the feeds. This strategy avoided complications related to mass fragment overlaps.

First, our time-resolved DEMS analysis was used to verify the significantly enhanced C₂H₄ yields during cyclic voltammetric electrode potential scans, confirming the enhanced stationary C₂H₄ yields using online GC analysis discussed above. Figure 5.4a displays time-resolved DEMS ion mass current scans of C₂H₄ and CH₄ in mixed ¹²CO₂/¹²CO (1:1, partial pressures of CO₂ and CO 50 kPa each) co-feeding conditions, in comparison to pure ¹²CO (100 kPa) and ¹²CO₂ (100 kPa) feeds. The mixed feed gave rise to greatly enhanced C₂H₄ ion mass currents (detected via the hydrogen-abstracted molecular (M-H)⁺ fragment

throughout) on the cathodic and anodic scan direction. Interestingly, the C_2H_4 ion mass currents on the cathodic and anodic sweep branch appeared quite asymmetric, suggesting local CO depletion and, as a result of this, decreased $*CO$ surface coverage at the most cathodic applied turning potential of $-1.0 V_{RHE}$. This depletion is likely due to CO diffusional mass transport limitations at the large overpotentials.

To account for differences in the individual partial pressures of CO and CO_2 under mixed and pure feeds, we then first compared the ethylene DEMS mass ion sweep under a $^{12}CO_2/^{12}CO$ (1:3, 25 kPa $^{12}CO_2$) co-feed (violet sweep curve in Figure 5.4b) with that under a $^{12}CO_2/Ar$ (1:3, 25 kPa $^{12}CO_2$) feed (orange curve in Figure 5.4b). We deliberately utilized a somewhat lower $^{12}CO_2$ partial pressure to highlight the kinetic effects of CO in the feed. The measured DEMS data evidenced that the cathodic ethylene production flanks under $^{12}CO_2/^{12}CO$ co-feed and $^{12}CO_2$ feed (both at 25 kPa $^{12}CO_2$) followed each other closely, evidencing that ethylene largely originates from dimerization of CO_2 -derived surface $*CO$ in cathodic sweep direction. Apparently, the “self-feeding” supply of CO by CO_2 to CO reduction is sufficient to maintain the ethylene formation. However, on the anodic sweep, only the $^{12}CO_2/^{12}CO$ co-feed was able to continue to generate comparable amounts of ethylene (purple curve), proving the suppression of local CO depletion at the catalytic interface.

Next, keeping the partial pressures of 25 kPa CO_2 and 75 kPa CO in the feed constant, we moved to an investigation of isotope-labelled mixed $^{12}CO_2/^{13}CO$ co-feeds, $^{12}CO_2/Ar$, and $^{13}CO/Ar$ feeds at comparable partial pressures to arrive at an accurate deconvolution of the origin of the ethylene carbon atoms associated with a quantitative assessment of the relative

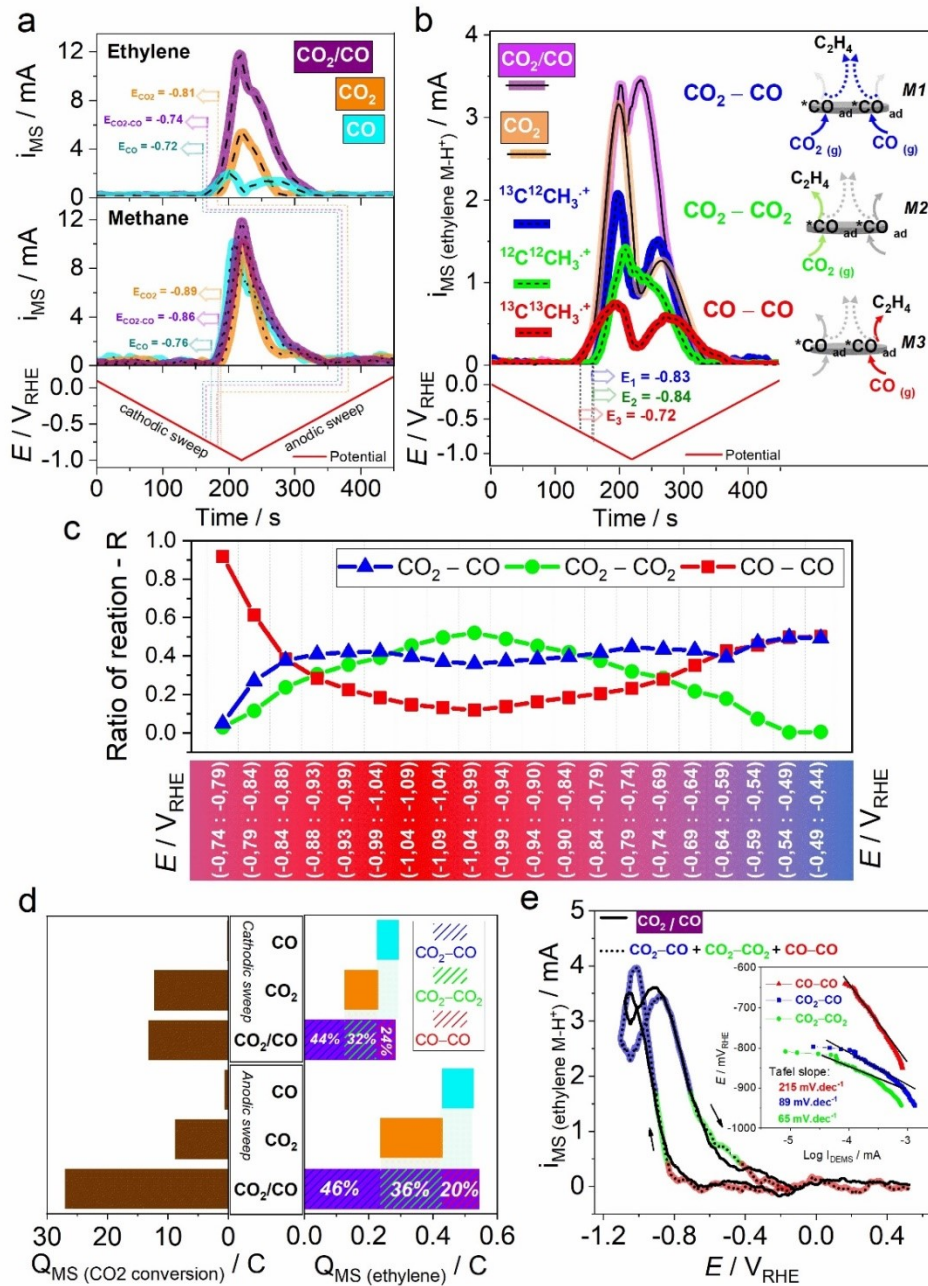


Figure 5.4 Quantitative deconvolution of relative contributions of competing CO-CO dimerization reaction pathways to ethylene using a novel *operando* DEMS capillary flow cell system. Differential electrochemical mass spectrometry (DEMS) sweep data obtained during CO_x reduction a CuO_x NP catalysts (supported on a flat 0.785 cm² glassy carbon electrode) using CO₂/CO co-feeds, pure CO₂ and pure CO feeds during a cyclic voltammetric scan at 5mV s⁻¹ and electrolyte flow of 5 μL s⁻¹. a) DEMS ion mass current sweeps over time: in the top, ethylene (molecule-H⁺, C₂H₃⁺ fragment at m/z=27), in the middle methane (CH₃⁺ m/z=15) measured under ¹²CO₂/¹²CO (1:1) co-feed (violet), pure ¹²CO₂ (orange) and pure ¹²CO feed (cyan), and in the bottom, the concurrent cyclic voltammetric sweep plotted over time. Kinetic onset potentials are listed for each feed system as E_{feed}, referenced to RHE. b) comparison of DEMS ion current sweeps over time of ethylene-related molecule-H⁺, (M-H⁺), fragments in ¹²CO₂/¹²CO (1:3) co-feeds (soft purple curve) and the corresponding ¹²CO₂/Ar

(1:3) feed maintaining 25 kPa CO₂ partial pressure (soft orange curve), and in the bottom, the concurrent cyclic voltammetric sweep plotted over time. The deconvoluted DEMS ion current sweeps over time of the three possible M-H⁺ ethylene fragments resulting under isotope-labelled ¹²CO₂/¹³CO co-feeds are shown by the blue, green, and red sweep profiles: ¹³C¹²CH₃⁺ (blue curve) represents the mechanistic pathway involving dimerization of one ¹³CO-derived and one ¹²CO₂-derived *CO (cross-coupling) according to scheme M1, ¹²C¹²CH₃⁺ (green curve) represents the mechanistic pathway involving dimerization of two ¹²CO₂-derived *CO, shown in scheme M2, and ¹³C¹³CH₃⁺ (red curve) arises from the mechanistic pathway involving dimerization of two ¹³CO-derived *CO shown in scheme M3. The values potential onset are represented for each mechanism, referred to as E_{mechanism}, with potential referenced to RHE. c) The ratio of reaction between the three mechanisms CO-CO, CO₂-CO₂ and CO₂-CO, with respective potential range of integration and with steps of 0.05 V from cathodic till anodic sweep. d) DEMS-derived ethylene mass charges for the three different feeds during the cathodic and anodic voltammetric sweep (right side), and the respective net CO₂ mass charges (CO₂ conversion) on the left side. The purple ethylene charge bars split into the relative contributions of each ethylene formation pathways (blue, green, red hashed patterns) from partial Figure 5.4b. e) Comparison of the DEMS – derived cyclic mass ion current sweep of ethylene under CO₂/CO (1:3) co-feeding, plotted in the potential domain (black line) with the sum of the three DEMS-derived ion mass sweeps of ethylene isotopes from each mechanistic pathway (blue, green, red colored dash line). The insert presents the Tafel lines of each partial reactive pathway of ethylene formation with Tafel slope values in mV_{RHE} dec⁻¹.

contributions of the three competing ethylene formation pathways (see Session 3.5.3). Figure 5.4b compares the three individual ethylene ion mass current sweeps in the time domain (red, blue, and green curves) corresponding to the three distinct reactive pathways over one cyclic voltammetric potential scan (red profile at the bottom). The red sweep denotes the sweeping trajectory of the mass current of the ¹³C₂H₃⁺ fragment (I_{m/z 29 (CO-CO)}) associated with the “CO-CO” pathway where CO originates entirely from the isotope labelled ¹³CO feed. The green sweep is the C₂H₃⁺ fragment (I_{m/z 27 (CO₂-CO₂)}) of the “CO₂-CO₂” pathway, where adsorbed CO stems entirely from non-labelled CO₂. Finally, the blue sweep is the ¹³CCH₃⁺ fragment (I_{m/z 28 (CO₂-CO)}) related to the cross-coupling “CO₂-CO” pathway where ethylene is formed from CO originating from CO₂ and CO. Alongside the mass current sweeps of the three C₂H₃⁺ ethylene fragments, Figure 5.4b also schematically illustrates the corresponding three CO dimerization pathways to ethylene in the respective color. Obviously, the contribution of each mechanistic pathway is a complex function of the applied electrode potential and scan direction.

The milli-second time-resolved measurements of catalytic ethylene sweeps using the DEMS capillary cell enabled us to accurately evaluate the kinetic onset potentials of ethylene for each mechanism separately (Figure 5.4b). To the best of our knowledge, there has been no time-resolved, transient kinetic study to date, where reaction mechanisms with kinetic onset potentials were reported for, as virtually all previous reports used steady-state or time-delayed NMR and chromatography-based product analysis techniques. Our analysis revealed that the C_2H_4 onset potentials shifted anodically by about 140 mV when operating in pure CO feeds (cyan sweep, $E_{CO} = -0.67 V_{RHE}$) compared to pure CO_2 feeds (orange sweep, $E_{CO_2} = -0.81 V_{RHE}$), evidencing a lower kinetic activation barrier of the catalytic CO to C_2H_4 cascade.

Integration of the three individual DEMS-derived deconvoluted ion mass current sweeps from Figure 5.4b yielded the total ethylene charges, Q_{MS} , of the pathways, which could be converted into relative charge contributions. The ratio of reaction in Figure 5.4c presents, the ratio of resulted ethylene charge from intervals of 0.05 V and for each mechanism CO-CO, CO_2-CO_2 and CO_2-CO . High production ratio over a large potential range is observed for the CO_2-CO mechanism, demonstrating a continuous contribution (Figure A2.9). The right-hand bars in Figure 5.4d presents, the total ethylene charges ($Q_{MS, ethylene}$) under the three different feed conditions during the cathodic (top) and anodic (bottom) sweep separately. The length of the purple bars underlines the enhanced ethylene production under CO_2/CO co-feed conditions compared to the orange and blue bars of the pure CO_2 and CO feeds. From the $Q_{MS(ethylene)}$ values, we evaluated the relative contribution of the cross-coupling “ CO_2-CO ” pathway to the total ethylene generation to as high as 45% over the entire sweep, compared to 33% of the “ CO_2-CO_2 ” and a mere 22% of the “ $CO-CO$ ” pathways in Figure A2.10. A breakdown of the relative contributions of each pathway during the anodic and cathodic scan are provided in Table 5.3. In other words, two thirds (67%) of the total ethylene yield can be kinetically directly attributed to the presence and reactivity of gaseous CO in the reactant feed during CO_x electroreduction. Also in Figure 5.4d, the integrated $m/z = 44$ ion mass charge of CO_2 ($Q_{MS(CO_2 conversion)}$) was evaluated for cathodic and anodic scan separately.

Interestingly, CO_2 conversion on the cathodic scan is similar for co-feeds and pure CO_2 feeds, while in the anodic scan direction, the conversion of CO_2 becomes 3x larger in the presence of CO, consistent with the larger ethylene formation charge in Figure 5.4c. Evidently, the

Table 5.3 Comparison of DEMS-derived kinetic reaction parameters of the three CO dimerization pathways to ethylene depending on the chemical origin of the CO. Cross-coupling (CO₂-CO) pathway: The dimerizing CO intermediates derive from CO₂ and CO; (CO₂-CO₂) pathway and (CO-CO) pathway: CO originated only from CO₂ or CO, respectively; i_{MS} (mA cm⁻² s⁻¹) is the respective maximum C₂H₃⁺ ion current, Q_{MS} (As) is the DEMS charge under the deconvoluted C₂H₃⁺ ion current sweeps under CO₂/CO co-feeding in cathodic and anodic scan direction. “Tafel” denotes the experimentally apparent (ion mass current derived) Tafel slopes (V_{RHE} dec⁻¹), while E (in units of V_{RHE}) is the experimental onset potential of ethylene formation.

Reactive CO dimerization pathway	Anodic scan direction		Cathodic scan direction		Tafel	E
	i_{MS}	Q_{MS}	i_{MS}	Q_{MS}		
CO₂-CO	1.5 ± 0.1	0.11 ± 0.012	2 ± 0.2	0.07 ± 0.006	89	-0.83
CO₂-CO₂	1 ± 0.4	0.09 ± 0.019	1.5 ± 0.2	0.05 ± 0.008	65	-0.84
CO-CO	0.63 ± 0.05	0.06 ± 0.009	0.77 ± 0.05	0.05 ± 0.013	215	-0.72

presence of CO is able to maintain higher CO₂ reduction rates even at the most cathodic electrode potentials, where local reactant depletion occurs under the pure CO₂ feed. To check the accuracy of our mechanistic pathway deconvolution, Figure 5.4e compares the experimentally measured total ethylene ion mass sweep (solid black line) with the sum of the three individual C₂H₃⁺ ion mass fragment sweeps (dashed curve with color coding for each mechanism). Clearly, the three contributions reproduce the experimental overall ethylene sweep curve very well. The inset of Figure 5.4d displays mechanism-specific DEMS-derived E-log(i_{MS}) Tafel plots and fitted linear Tafel lines with slopes of 81, 125 and 184 mV.dec⁻¹ for CO₂-CO, CO₂-CO₂ and CO-CO respectively. Thus, the lowest Tafel slope was found for the cross-coupling CO₂-CO pathway, underlining the facile reaction kinetics of the dimerization of two CO molecules from distinct origins. The CO-CO mechanism, with its lowest onset potential, showed a significantly less favorable Tafel slope with the most significant voltage loss per current decade, likely based on the extremely low CO solubility and rapid local interfacial CO depletion affecting the apparent Tafel slope (see Table 5.3).

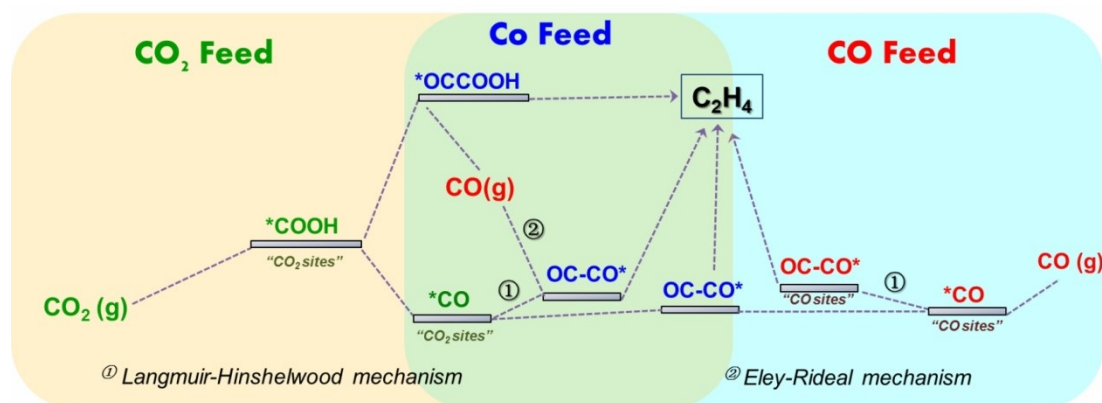
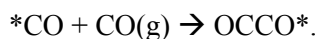
Co-feed mechanism

Figure 5.5 Mechanistic hypotheses of enhanced ethylene production under CO_2/CO reactant co-feeds. The demonstration of possible dimerization pathways with common intermediates in CO_2 feed, co-feed and CO feed.

Figure 5.5 details the mechanistic implications and conclusions resulting from our time-resolved kinetic analysis of the electrocatalytic $\text{CO}_2\text{-CO-C}_2\text{H}_4$ reaction cascade, sketching plausible reaction pathways and vital intermediates of the three feed conditions. First and foremost, the DEMS results evidence that the C_2H_4 production under CO_2/CO co-feeds originates predominantly from dimerization of two adsorbed *CO molecules to form a neutral OC-CO* or a previously reported negatively charged OC-CO* adduct,⁸⁴ which is further reduced to ethylene. The dominant cross-coupling Langmuir-Hinshelwood-type mechanism (denoted “1” in Figure 5.5) with the reactive *CO stemming from both CO_2 and CO is marked as the blue dimerization pathway. The fact that CO in the feed, CO(g) , boosts ethylene yields via a dominant cross-coupling pathway despite a much lower combined CO_x concentration at the liquid-solid interface, speaks to non-competing adsorption of CO and CO_2 . This suggests the existence of two distinct, non-scrambling “reactant-specific” surface adsorption sites in atomic proximity on the operating Cu nanocatalyst, one for the adsorption of dissolved CO_2 and another for dissolved interfacial CO . This is a rather unexpected, yet interesting conclusion with important implications for catalyst and electrolyte design. Also, spatially inhomogeneous distributions of “reactant-specific” $\text{*}^{12}\text{CO}$ and $\text{*}^{13}\text{CO}$ sites on the catalyst surface would consequently result in products enriched in one or the other isotope, as recently reported by Lum and Ager¹⁰⁵.

In addition to our “two-site” hypothesis involving Langmuir-Hinshelwood type pathways, a Eley-Rideal (ER) type reaction pathway, involving C-C coupling (denoted by “2” in Figure 5.5) of an adsorbed *CO and a solvated CO(g) at the outer Helmholtz layer, could, in principle, account for or at least contribute to the enhanced ethylene formation rates according:



Following what is known on similar ER mechanisms,^{74, 82, 120} we cannot fully exclude that increasing CO_(g) concentrations at the double layer may favor ER-type C₂H₄ production in parallel to the Langmuir-Hinshelwood pathway. Data in Figure A2.11 showed that increasing the local interfacial CO_(g) concentration under CO-rich CO₂/CO (1:3) co-feeds decreased the net CO formation due to faster C-C coupling and ethylene formation.

Finally, DFT calculations indicated that yet another mechanistic coupling pathway to C₂H₄, though energetically somewhat less favorable than the *CO dimerization on Cu(100) facets,⁸² may open up on non-Cu(100) facets under co-feed conditions with high CO partial pressures. This pathway involves the coupling of adsorbed *COOH and *CO and becomes energetically more and more favorable at large *CO coverages and high local CO_(g) concentration. This new C₂ pathway of *COOH and *CO/CO_(g) may become energetically possible on facets other than Cu(100) facets and proceeds according to



in parallel to the existing *OCCO dimerization pathway (see Figure 5.5).

5.5 Extended co-feed mechanism on bifunctional tandem catalyst design

The co-feed mechanism also provides a strategy to design an active catalyst towards C₂H₄. To mimic the co-feed condition, a catalyst with high CO production could be used as a substitution of CO gas feed in CO₂RR. In this session, Nickel-nitrogen-functionalized carbon material (NiNC) and Ag were chosen as the tandem partner for their excellent CO activity, to increase the local CO concentration on the CuO_x NPs interface.

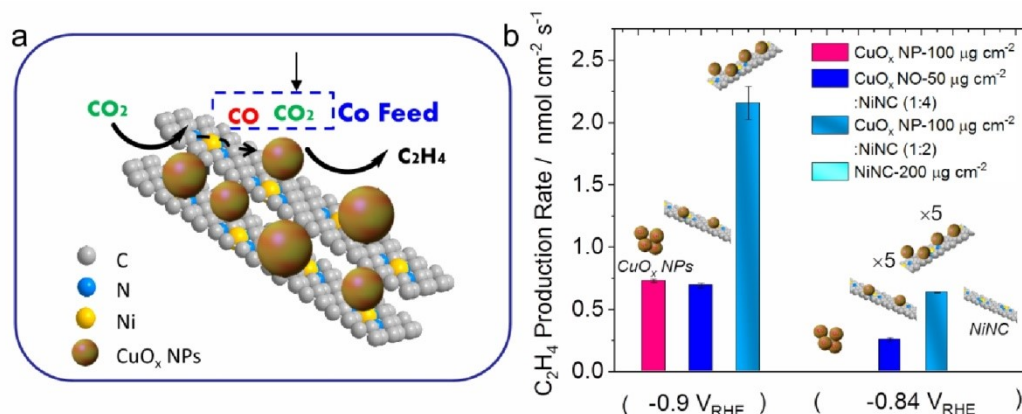


Figure 5.6 The realization of enhanced ethylene production using internal CO₂/CO “self co-feeding” using non-metallic/metallic tandem catalyst design. a) The tandem catalyst design is combining NiNC material as a local CO-producer and CuO_x NPs on carbon paper electrode. b) C₂H₄ production rate with the bifunctional hybrid catalyst with carbon paper as working electrode for CO₂RR at the various component and fixed overpotentials. The experimental C₂H₄ production rates at -0.84 V_{RHE} are multiplied by 5 for comparison. No detectable C₂H₄ formation on pure CuO_x NPs with areal loading of 100 μg cm⁻² at -0.84 V_{RHE}. No detectable C₂H₄ formation on pure NiNC catalyst at both -0.84 V_{RHE} and -0.9 V_{RHE}.

Figure 5.6a displays the first examples of a bifunctional non-metallic/metallic tandem catalyst. High-surface area Ni-nitrogen-functionalized carbon (NiNC) acts as selective CO-producer⁴⁷ and supports CuO_x NPs with reactant-specific surface sites. The SEM images of the as-prepared CuO_x-NiNC tandem catalyst are shown in Figure A2.12, illustrating the location of the two distinct components. The neighbouring CuO_x NPs and NiNC are among micrometer scale while partially overlapped with each other. The catalytic C₂H₄ performance of CuO_x-NiNC tandem catalysts was significantly enhanced compared to supported CuO_x NPs. As shown in Figure 5.6b, the tandem CuO_x-NiNC (1:4) catalyst features the same C₂H₄ production yields at half the mass loading of CuO_x NP. Similarly, CuO_x-NiNC (1:2) catalysts yield twice the C₂H₄ production rate. At overpotentials of -0.84V_{RHE}, CuO_x-NiNC tandem catalysts produce considerably less free gaseous CO (Figure A2.13a) compared to pure NiNC, evidencing that some of the internally generated CO are immediately consumed by the tandem catalysts. The CH₄ yield increased in the tandem catalysts, as well (Figure A2.13b). The liquid products analysis for the CuO_x-NiNC tandem catalysts is included in Table A2.1.

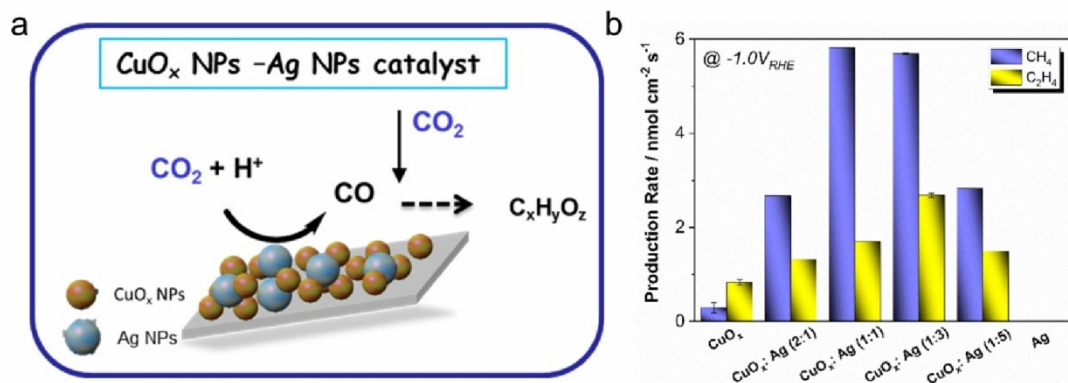


Figure 5.7 The realization of enhanced ethylene/methane production using internal CO₂/CO “self co-feeding” using metallic/metallic tandem catalyst design with fixed CuO_x areal particles density of 100 μg/cm². a) The catalyst is combining Ag material as a local CO-producer and CuO_x NPs on glassy carbon electrode. b) C₂H₄ and CH₄ production rate with CuO_x-NiNC catalyst for CO₂RR at the various component and fixed overpotentials. Error bars are given as standard error of mean.

The metallic/metallic tandem catalyst was also studied. Shown in Figure 5.7a, Ag was employed as local CO-maker for the CuO_x NPs. Figure 5.7b plots the absolute production rates on various CuO_x to Ag component at electrode potentials of -1.0 V_{RHE}. The production rate of C₂H₄ was facilitated with all CuO_x to Ag ratios compared to pure CuO_x, especially at the ratio of 1 to 3 (CuO_x:Ag). The CH₄ production rate exhibited a same trend as C₂H₄, again, indicating that the “self-formed” CO played a dominating role in the catalytic reactions. To test the stability of the tandem CuO_x-Ag catalyst in the H-cell configuration, 20-hour electrolysis was carried out using the CuO_x: Ag (1:3) catalyst at the chosen electrode potential (-1.0 V_{RHE}), where the respective maximum C₂H₄ was observed (Figure A2.14). The tandem catalysts reported in the literatures^{28, 121, 122} are also in good accordance with above-mentioned co-feed system, again, suggesting the ubiquity of our co-feed mechanism.

5.6 Conclusions

The electroreduction of mixed CO₂/CO feeds on CuO_x NPs and pure CO₂ feeds on tandem Ni/N doped carbon-CuO_x catalysts displayed significantly improved catalytic C₂H₄ yields over a wide electrode potential range. Using *operando* DEMS, time-resolved isotope labelling experiments, carried out in a customized CO₂ capillary cell, the possible mechanistic pathways were quantitatively deconvoluted. Our analysis demonstrated that the enhanced

C_2H_4 production largely originated from a crossed CO_2 -CO combination pathway and that over two-thirds of the generated C_2H_4 involved co-fed CO. The co-fed CO gas does not compete with CO_2 for adsorption sites, which implies the existence of separate, non-scrambling reactant-specific surface adsorption sites for CO_2 and CO. Finally, we demonstrated that the co-feeding mechanism is the mechanistic basis of internally co-fed tandem catalyst concepts. In the end, we confirmed our mechanistic conclusions about the equivalence of external and internal CO co-feeding highlighting the non-metallic/metallic CuO_x -NiNC and metallic/metallic CuO_x -Ag tandem catalysts, which involve a (non-)metallic CO producer coupled to ethylene-producing CuO_x . Our mechanistic insights offer a wide range of practical catalysts design strategies to CO₂RR electrocatalyst with improved ethylene yield, but, in a more general sense, we think our mechanistic concepts are transferable to other interesting products such as ethanol or propanol, as well.

Chapter 6 Sheet-like Copper Oxides with Stable and Selective Ethylene Production for Direct CO₂ Electroreduction

Oxidic and oxide-derived nanostructured copper catalysts have frequently been used to promote the electrochemical reduction of CO₂ (CO₂RR) to higher-value products such as ethylene. Here, we present a successful synthesis of free-standing sheet-like copper oxides nanoparticles, exposing predominantly {001} facets, and investigate CO₂RR performance in an H-cell configuration. The highly active CuO_x nanoparticles exhibit ordinary stability towards ethylene over at least 24 hours. A combination of operando X-ray Absorption Spectroscopy (XAS) and operando Wide-Angle X-ray Scattering (WAXS) are used to reveal the changes in structure the catalyst that undergoes at different reaction stages. The onset potentials of the main products are also determined by operando Differential Electrochemical Mass Spectrometry (DEMS). The complementary analysis depicts a highly active system, in which a complete reduction of oxidized Cu progresses from the surface towards bulk layers. The defect-rich surface introduced by the self-reducing process is proposed to be responsible for the catalytically stable performance for C₂H₄ formation.

Chapter 6 and its supplementary information section (Appendix A3) were reproduced from a manuscript under preparation for submission.

Xingli Wang, Katharina Klingan, Jorge Ferreira de Araújo, Henrike Schmies, Isaac Martens, Fabio Dionigi, Shan Jiang, Holger Dau, and Peter Strasser, “Sheet-like Copper Oxides with Stable and Selective Ethylene Production for Direct CO₂ Electroreduction”

X.W., P.S. conceived and designed the experiments. X.W. performed the experiments and analyzed the data, K.K. helped the experiment of *operando* XAS, data analysis and wrote the XAS report; F.J. helped the DEMS measurements; X.W., H.S., I.M., F.D. contributed to WAXS measurements and data analysis. S.J. did *in situ* Raman spectroscopy, X.W. and P.S. wrote the manuscript; all authors contributed to the discussions.

6.1 Synthesis and characterization

The sheet-like CuO_x (CuO_x NS) catalyst was prepared by solvothermal synthesis through Cu(OH)₂ intermediate in alkaline condition (see Figure A3.1). The wrinkled large-scale thin Cu(OH)₂ layer is then decomposed to CuO and H₂O. Figure 6.1 a-b presents scanning electron microscopy (SEM) image and transmission electron microscopy (TEM) image of as-prepared copper oxides nanoparticles. As shown in the images, the 2-dimension (2D) structure remained after the thermal decomposition of Cu(OH)₂, while the large sheet layer split into small pieces and the narrow ones merged together. The final products exhibit rectangular nanosheet-like morphology with serrated edges on the sides of shorter length. Figure A3.2a shows cross-section image of CuO_x NS, indicating a stacked structure in a single free standing CuO_x NS. The thickness of each nanosheet is less than 30 nm. The crystallinity and surface roughness are highlighted by the high-resolution transmission electron microscopy (HR-TEM) image and selected area electron diffraction (SAED) image. The HR-TEM image (Figure 6.1c) of the CuO_x NS shows well-defined lattice fringes with an interplanar spacing of 2.8Å, corresponding to {110} planes of monoclinic CuO. Moreover, from SAED pattern (Figure 6.1d), the rhombus diffraction spots along [001] can be seen with indexed (020), (-110), (-200), (-1-10), (0-20) and (1-10) planes, indicating that the CuO_x NS has {001} exposed surface. The relative intensity of the diffraction spots is presented in Figure A3.2b. The crystal structure is also provided in Figure A3.3 with indexed (001), (110) and (11-1) planes.

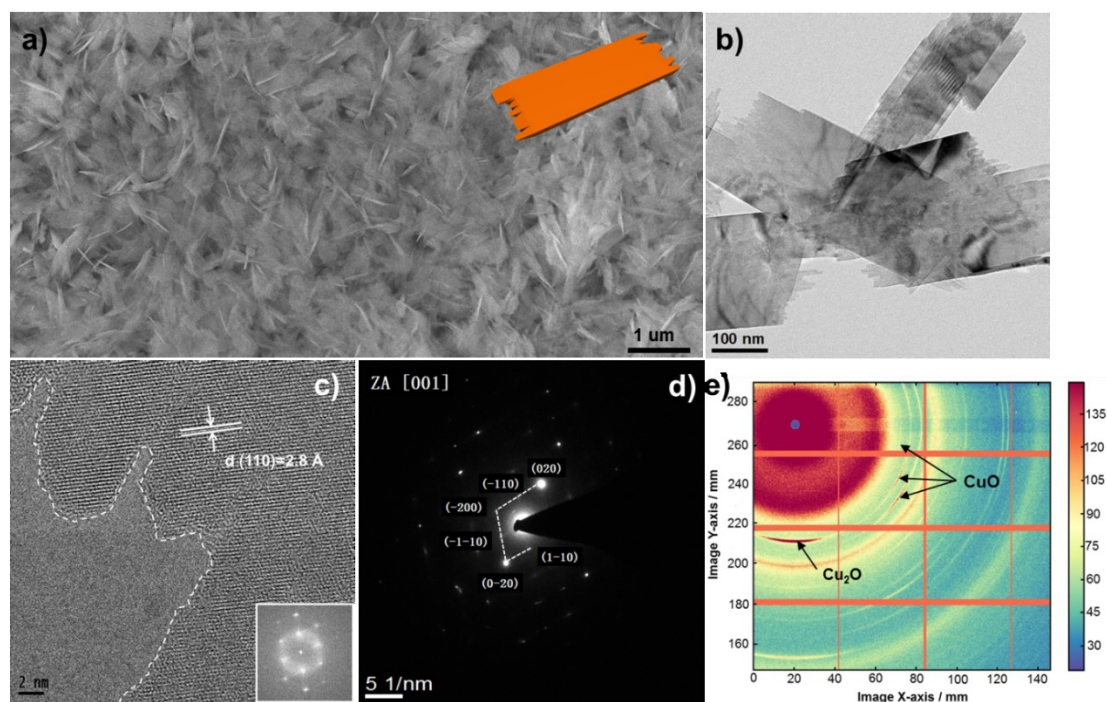


Figure 6.1 Morphological, structural characterizations of sheet-like CuO_x nanoparticles synthesized in this study. a) Large-scale scanning electron microscopy (SEM) image and 3D structure of CuO_x NS (insert, orange). b) Transmission electron microscopy (TEM) image and c) high resolution TEM images with measured lattice distance and the corresponding fast Fourier transformation. d) Selected area electron diffraction (SAED) pattern along zone axis [001]. e) 2D Synchrotron grazing incidence wide-angle X-ray scattering (GI-WAXS) image demonstrating preferred orientation of as-prepared CuO_x NS on glassy carbon. Additional azimuthally integrated line profiles are shown in Figure A4.4b.

A 2D synchrotron grazing incidence wide-angle X-ray scattering (GI-WAXS) image of drop-casting CuO_x NS on glassy carbon is shown in Figure 6.1e. The diffraction patterns are mainly contributed by the CuO phase, while a small reflection due to an additional Cu_2O phase is also observed with low angle. The higher order Cu (I) peaks appear absent. It can be seen that the (002) and (11-1) reflections of Cu (II) exhibit a stronger intensity in the meridional direction, demonstrating that the CuO_x nanosheets are stacked along the $\langle 001 \rangle$ direction and that this one is perpendicular to the incident beam. A partial contour plot is shown in Figure A4.4a, indicating the coexistence of both the Cu_2O phase and the CuO phase. The distribution of scattering intensity was obtained by integration of the 2D detector GI-WAXS image numerically. Azimuthal integrations of CuO_x NS line profiles are included in Figure A4.4b.

6.2 Electrochemical CO₂RR over sheet-like CuO_x catalysts

The catalytic CO₂RR activity of as-prepared CuO_x NS was tested in a two-compartment membrane-separated H-cell configuration within the potential range of -0.75V to -1.0V versus RHE in CO₂ saturated 0.1 M KHCO₃. We deposited the catalysts onto glassy carbon electrode via drop coating of a catalyst ink to keep the catalyst loading of 100 μg cm⁻² constant for each measurement. The detailed absolute production rates for all products after 1h are listed in Figure 6.2a. C₂H₄ exhibited earlier formation compared to CH₄. Thus, a region with only C₂H₄ as the unique hydrocarbon can be observed at relatively low overpotentials. In contrast, CH₄ formation experienced a rapid growth after -0.9 V_{RHE} and exceeded C₂H₄ at -0.97 V_{RHE}. The corresponding partial densities are shown in Figure 6.2b, demonstrating an outstanding selectivity toward hydrocarbon. The geometric current density of C₂H₄ reached up to 6.2 mA cm⁻² at -0.97 V_{RHE}, and for CO remained at low level during the entire given overpotential range. The production rate-derived Faradic efficiencies (FEs) of all detectable products over selected electrode potentials are shown in Figure A3.5. The total FEs for each measurement reaches 90%, with clear suppression of HER and enhancement of C₂H₄ with higher overpotentials. Since the catalytical electroreduction process on copper oxides always involves a self-reducing period with a mixed matrix of metallic and oxidized copper, long-term electrolysis up to ~20 h has been carried out at -0.76 V_{RHE}, -0.84 V_{RHE} and -1.0 V_{RHE}, respectively. Figure 6.2c-f shows the production rates (and FEs) as a function of reaction time. The production rates towards the main carbon-based products (CO, CH₄, and C₂H₄) displayed a similar activation process in the initial stage of CO₂ electrolysis, while with higher overpotentials, a larger slope was observed (Figure 6.2c-e), indicating a faster transition time. After 120 min, the production rates reached to the peak value. At all selected overpotentials, C₂H₄ formation remains constant after peak values, while CH₄ only formed at -1.0 V_{RHE} and declined after the highest point. It is noteworthy that C₂H₄ is the only hydrocarbon formed at -0.84 V_{RHE} and C₂H₄ production rate is even higher (1.6 nmol cm⁻² s⁻¹) than conventional electropolished Cu foil at -1.0 V_{RHE}.¹²³ The testing time was then prolonged to 1200 min. As we can see in Figure 6.2f, the production rate and FE towards C₂H₄ displayed minor changes over the reaction time. The morphology change of the as-prepared CuO_x NS

was determined by SEM after 1200-min electrolysis, where dramatically change was found displayed as particle agglomeration (see Figure A3.6). The same phenomena were observed after long-term reaction at $-0.76 \text{ V}_{\text{RHE}}$ (Figure A3.7).

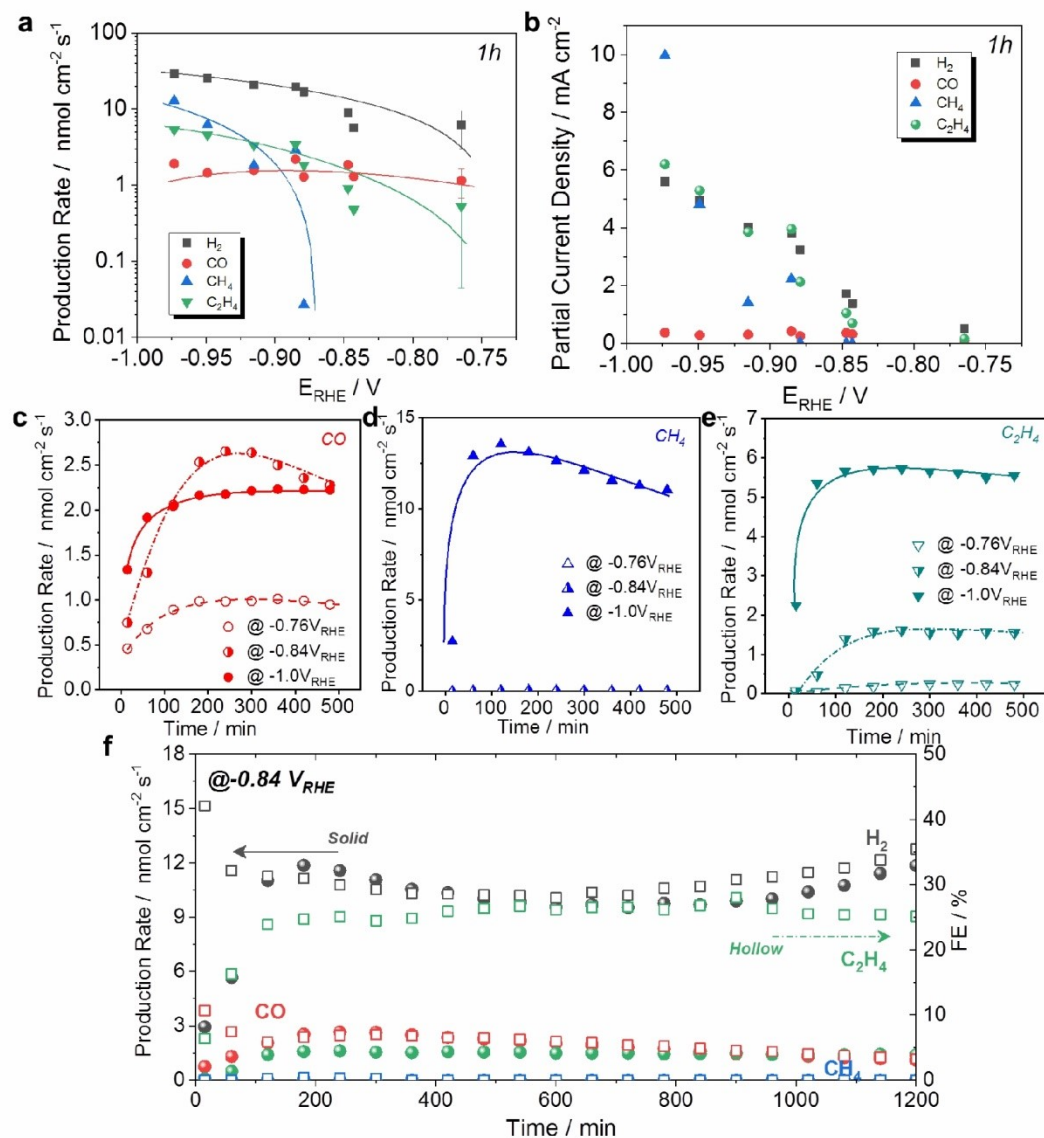


Figure 6.2 Electrochemical Performance of CO_2RR with as-prepared CuO_x NS in H-cell configuration. a) Absolute product formation rates of major gaseous products as a function of applied electrode potentials during CO_2RR in CO_2 -saturated 0.1M KHCO_3 at 60 min. b) Partial current density of major gaseous products. Time-dependent absolute product formation rates on c) CO , d) CH_4 and e) C_2H_4 with various overpotentials. f) Chronoamperometric performance stability of the CO_2 reduction reaction on CuO_x NS in CO_2 -saturated 0.1M KHCO_3 at $-0.84 \text{ V}_{\text{RHE}}$.

6.3 Discussions

The above-mentioned observations of activity/selectivity evolution at fixed overpotential suggest that the catalytic performance is mainly dependent on either structural-morphological evolution and/or crystalline phase transition. Taking the long-stability test at $-0.84\text{ V}_{\text{RHE}}$ as an example, which showed a considerable C₂H₄ formation but no CH₄, the products formation was unaffected after reaching their peak point. Now, the sintering and coalescence of CuO_x nanosheets could be observed as early as 1-h after start of the electrolysis experiment (see Figure A3.8). In addition, the highest C₂H₄ selectivity was achieved after the original shape was lost. This implies that the catalyst morphology and its evolution do not appear to be the main factor or determinant for the experimental high catalytic performance. Considering relatively large negative overpotentials used during the measurements, copper oxides are likely quantitatively reduced to metallic Cu. To determine the prevalent local structure motifs, *operando* XAS was employed to examine the local atomic structure evolution and *in situ* GI-WAXS for crystalline phase change of as-prepared CuO_x electrocatalyst under catalytic operating condition.

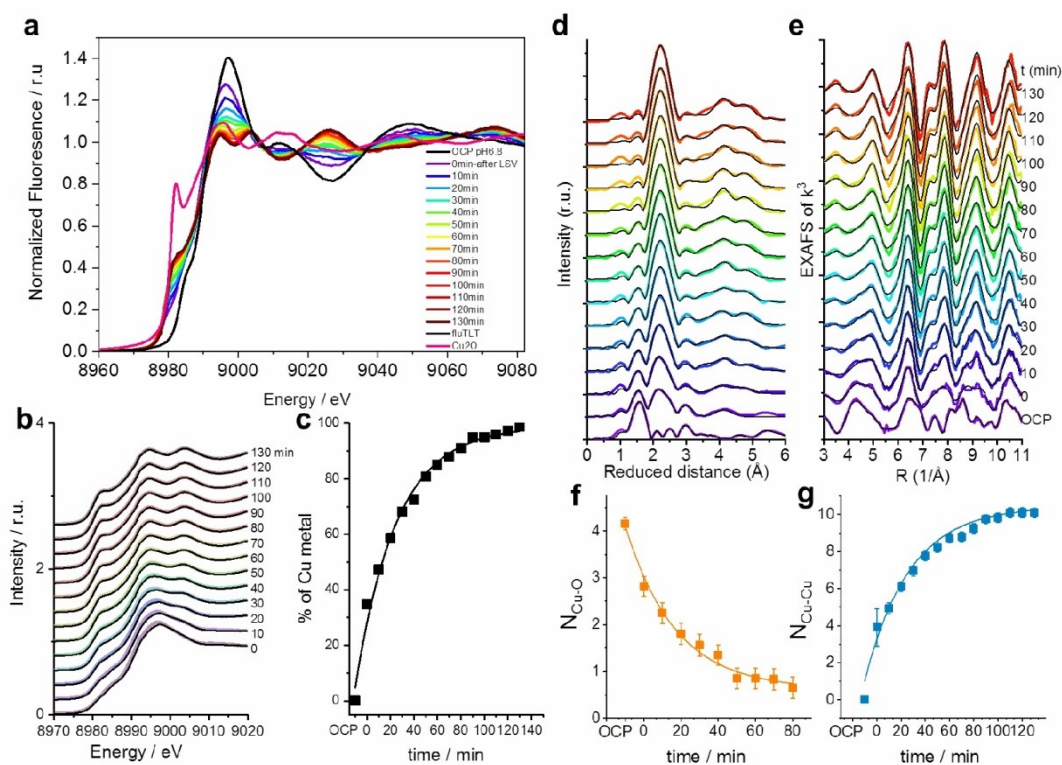


Figure 6.3 Catalyst evolution during CO₂RR characterized by *operando* XAS. a) XANES at the Cu K-edge of the CuO_x NS film at OCP in 0.1 M KHCO₃ at pH 6.8 and during 130 min CO₂RR at -0.84 V_{RHE}. b) Linear combinations (with the weighting factors as fit parameters) of Cu foil and the CuO_x NS film at OCP were fitted to experimental data of the CuO_x NS film during 130 min CO₂RR at -0.84 V_{RHE}. Colored lines represent the experimental data and black lines the linear combinations. c) Amount of Cu metal in the CuO_x nanoparticle film during 130 min CO₂RR at -0.84 V_{RHE}. Values are obtained by linear combinations (with the weighting factors as fit parameters) of Cu foil and the CuO_x film at OCP, which were fitted to experimental data. d) FT of k³ weighted EXAFS at the Cu K-edge of the CuO_x film at OCP and during 130 min CO₂RR at -0.84 V_{RHE} in 0.1 M KHCO₃ at pH 6.8. Colored lines represent the experimental data and black lines the simulations. The distance on the x-axis is reduced by 0.35 Å relative to the real distance. e) EXAFS (k³ weighted) at the Cu K-edge of the CuO_x film at OCP and during 130 min CO₂RR at -0.84 V_{RHE} in 0.1 M KHCO₃ at pH 6.8. Colored lines represent the experimental data and black lines the simulations. Coordination numbers of the first Cu-O (f) coordination sphere and the first intermetallic Cu-Cu (g) shell. Catalyst loading: 100 μg cm⁻².

The CuO_x NS electrode was prepared and characterized by *operando* XAS in fluorescence geometry. X-ray absorption near edge spectra (XANES) shown in Figure A3.9 compares the oxidation state of CuO_x NS film with reference samples, which is identical in its dry state and at OCP in 0.1 M KHCO₃ at pH 6.8 with single CuO being the main present component. The small portion of Cu₂O which was detected by WAXS (Figure 6.1e) is attributed to the grazing

incidence mode, which offers a much larger surface sampled by the X-ray beam. The catalyst structure at resting condition is a highly ordered CuO structure. The nanoparticle film is even more ordered than the reference powder (see higher Debye Waller parameters for the CuO powder reference in the simulation table). However, CuO reference powder and CuO nanoparticle film have the same atomic structure (see Figure A3.10 and simulation results in Table A3.1). Contributions from Cu(OH)₂ and Cu₂O in the relaxed state of the CuO NP film can be excluded.

Applying a constant electrode potential of $-0.84 V_{\text{RHE}}$, complete reduction to metallic copper is observed after 130 min. The transformation from CuO to Cu was followed by the intensity decrease of the pre-edge feature at 8996 eV. The reduction from cupric oxide, CuO, to metallic Cu occurs directly without any detectable intermediate formation of Cu₂O (Figure 6.3a). Linear combinations of Cu foil and the CuO NS film at OCP were calculated and fitted with the weighting factors as fit parameters to the experimental spectra. Directly after the LSV scan, 35% of the bulk volume has been reduced to Cu metal (see Figure 6.3b-c). At the end of the experiment, all Cu species are present as Cu metal. (The linear combination gives 99%, the remaining 1% is within the uncertainty of the data quality). The gradual change from CuO to Cu metal is also indicated by the intensity decrease of the Cu-O bond (1.94 Å) and the intensity increase of the Cu-Cu (2.53 Å) bond (Figure 6.3d-e). Coordination numbers (CN) of Cu-O decreased with the reduction process, while CN of Cu-Cu increased, and stabilized at 10 after 120 min. There is no change in the Cu-O distance (first coordination sphere) and no change in the Cu-Cu bond length. The obtained CN of self-reduced Cu is smaller than that expected for the face centered cubic (FCC) structure of metallic copper, indicating a defective structure formed during catalytic reduction. The resulting undercoordinated sites with strong binding ability continuously contribute to the outstanding catalytic performance, which is also proposed and discussed by previous study.^{94, 124, 125}

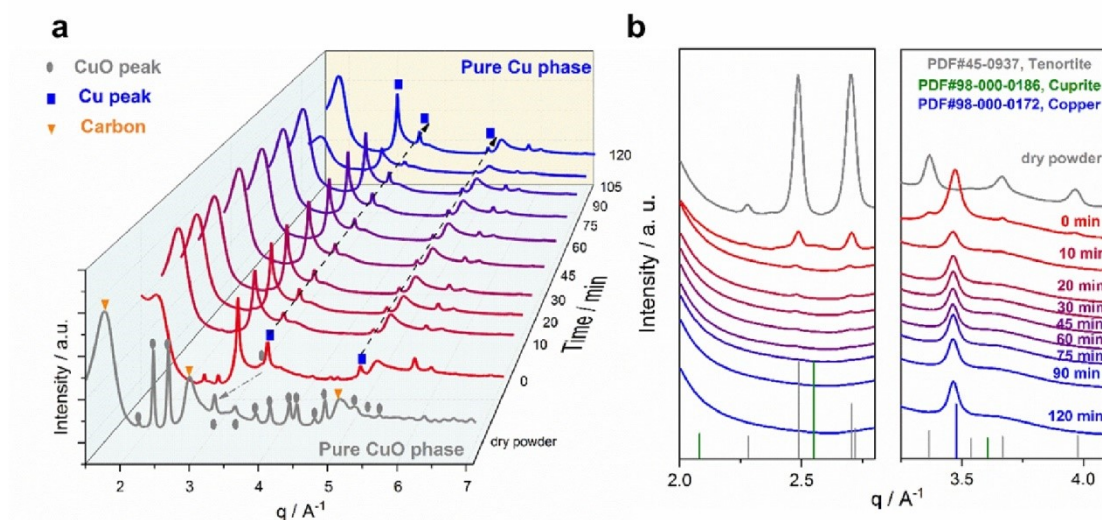


Figure 6.4 Catalyst shape evolution detected by *in situ* WAXS. a, b) *in situ* WAXS patterns of CuO_x NS electrode with catalyst loading of 20 $\mu\text{g cm}^{-2}$ during 130 min CO₂RR at $-0.84 V_{\text{RHE}}$.

The reduction of CuO_x NS to metallic copper during operation at catalytic potential was further confirmed by *in situ* WAXS measured in grazing incidence mode (see Figure 6.4a). The dry powder showed clear reflections of a single Cu(II) oxide phase with the whole pixel integration on the 2D detector. The majority of this CuO phase was reduced within the first 30 min, while a small portion of a residual oxide phase lasted for almost 120 min. The vanishing of distinct CuO reflections and growth of metallic copper reflections are shown in Figure 6.4b.

The evolution of the dominant catalytic reaction products during the change in the catalyst structure owing to the reduction of CuO_x NS are shown in Figure 6.5. The time resolved transient ion currents of each product was recorded over applied electrode potential and time using a custom-designed millisecond-resolved differential electrochemical mass spectrometry (DEMS) flow cell. During repeated cyclic voltammetric scans, the product ion current - potential curves showed increasing ion currents in cathodic scan directions, while the ion currents decreased in the anodic scan direction (as shown in Figure 6.5).

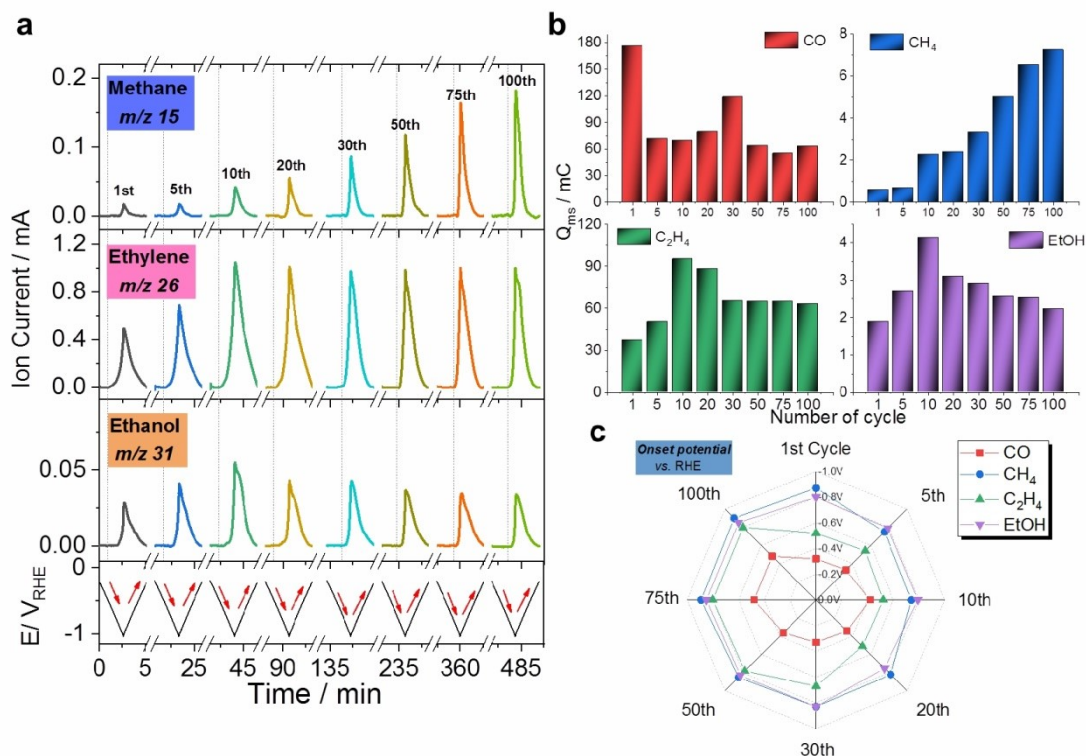


Figure 6.5 Products formation and onset potential shift along the electroreduction of CuO_x NS catalyst. a) *operando* Differential electrochemical mass spectrometry (DEMS) sweep data obtained during CO₂RR on CuO_x NS catalyst (supported on a flat 0.785 cm² glassy carbon electrode) using CO₂-saturated 0.1M KHCO₃ by continuous cyclic voltammetric scan at 5mV s⁻¹. b) DEMS-derived mass charges for various products formed during the cathodic and anodic voltammetric sweep. c) Spider plot shows the variations in the onset electrode potential of key products during CO₂RR by continuous cyclic voltammetric scan at 5mV s⁻¹. Product molecules considered are: m/z =28 CO, m/z = 15 corresponding to methane, m/z =26 corresponding to ethylene, m/z =31 corresponding to ethanol.

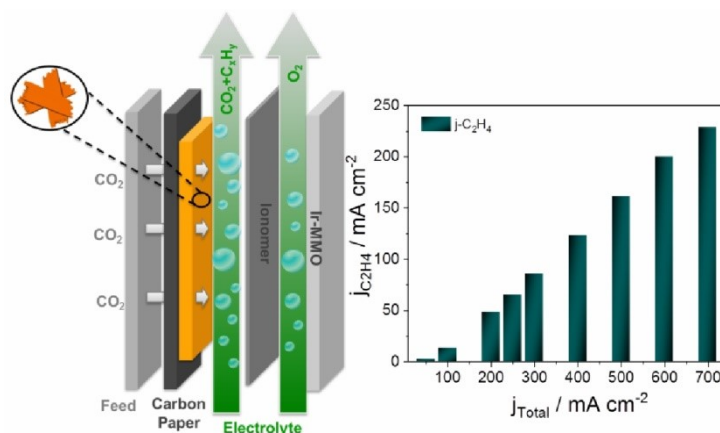
Figure 6.5a displays and compares the characteristic ion currents of CH₄, C₂H₄ and ethanol (EtOH) over the voltammetric cycle number. C₂H₄ and ethanol (EtOH) exhibited very similar trend, where the ion currents peaked after the 10th cycle, while CH₄ increased monotonically. The mass ion charges of CO, CH₄, C₂H₄ and EtOH (ethanol) were considered and deconvoluted at m/z values of 28, 15, 26, 31, respectively. These m/z values yield quantitative measures of the product formation rates (Yields) over each cycle (see Figure 6.5b). All product yield showed growing trends as the metallic character of the Cu catalysts increased in the course of the reduction process; this is in contrast to CO, the yield of which appeared to decline after 5th cycle. The onset potentials of the key catalytic reduction products and their changes with cycle number and with catalyst structure are included in Figure 6.5c,

demonstrating a significant influence on C₂H₄ and CO. After 40 min, the onset potentials of C₂H₄ and CO moved to more and more negative values, where a large portion of the initial oxidized copper was reduced. Thus, in the beginning of CO₂RR (within 10 cycles), the catalyst with a large portion of cupric oxide phase seems inactivate towards CO₂RR, leading to relatively lower ion currents toward the major products. This may also indicate the co-presence of a carbonate passivation layer, which suppresses the products evolution. While it shows a positive effect on onset potentials towards CO and ethylene, while not affecting the CH₄ and EtOH onset potential.

6.4 Conclusions

We have developed a facile synthesis route towards sheet-like CuO_x nanoparticles with predominantly {001} facet. Catalytic tests in an H-Cell showed highly active CO₂RR performance and excellent stability. As illuminated by ex-situ SEM, the loss of initial morphology did not cause catalyst deactivation. Using the combination of *operando* XAS and *in situ* WAXS, we were able to trace the reconstruction process that CuO_x NS underwent during CO₂RR, indicating a conversion from the initial copper oxide phase to catalytically active metallic copper phase. The sustained presence of ionic Cu species below our detection limit cannot be dismissed, nor confirmed as the origin of sustained catalytic activity. Meanwhile, under-coordinated surface sites were generated by self-reducing catalysts, which was held responsible for the outstanding experimental performance. Our *operando* DEMS results suggested that the initial oxidized copper phase and/or a carbonate passivation layer shifted the onset potentials on CO and C₂H₄ more anodically, but left those of CH₄ and EtOH unaffected. Together the materials and kinetic catalytic study presented here on previously unexplored sheet-like CuO_x nanoparticles have established valuable structure-activity-selectivity correlations for future catalyst designs.

Chapter 7 Achieving high C_2H_4 Evolution at industrial current densities on CuO_x nanosheet derived gas diffusion electrode



The electrochemical conversion of CO_2 (CO₂RR) to valuable carbon-based products at an industrial equivalent scale is posed to assess the potential economic and technical feasibility of the technology. Delivered by the work presented in Chapter 6, the sheet-like CuO_x nanoparticles exhibit the promise to selectively convert CO_2 into ethylene during CO₂RR. We thus employ such CuO_x nanosheets (CuO_x NS) as a catalyst candidate for a type of Gas Diffusion Electrode (GDE) combined Micro-Flow-Cell (MFC) measurement. The catalytic performance of CuO_x NS exhibits an outstanding ethylene production under industry equivalent neutral condition, demonstrating C_2H_4 partial current density of $229\ mA\ cm^{-2}$ and stable faradic C_2H_4 efficiencies around 30 % for up to 24 hours (at $300\ mA\ cm^{-2}$). The partial current towards C_{2+} products reaches $\sim 410\ mA\ cm^{-2}$. The morphological and structural evolution of the reactive CuO_x NS catalysts is also investigated in combination with an electrochemical liquid TEM micro reactor. Our quasi in situ TEM monitoring tracked a remarkable amount of Cu particle evolution, which is in good agreement with the ex situ-TEM images of catalysts measured under GDE-flow-cell conditions. The present study corroborates the power of in situ electrochemical liquid TEM studies for the understanding of activity-selectivity-morphology relations under catalytic CO₂RR operating conditions at the industry level.

Chapter 7 and its supplementary information section (Appendix A4) were reproduced from a manuscript under preparation for submission.

Xingli Wang, Tim Möller, Malte Klingenhof, Stefanie Kühl and Peter Strasser, “Achieving high C₂H₄ Evolution at industrial current densities on CuO_x nanosheet derived gas diffusion electrode”

P.S., X.W. conceived and designed the experiments. X.W. M. K. and S. K. performed the microscopy experiments, X.W analyzed the data, T.M. helped with the flow cell measurement and data analysis; X.W. and P.S. wrote the manuscript; all authors contributed to the discussions

7.1 CO₂RR electrolysis using GDE combined MFC

To assess the technological potential of CuO_x nanosheets catalysts (synthesis details in Chapter 3.12) for industrial CO₂ co-electrolysis, we employed a single three-electrode electrolyzer with multi-chambers cell set-ups for pressurizing the gas flow and circulated electrolyte flows in the cathodic chamber (see Figure 7.1a). In the electrolyzer, a catalyst suspension containing a known amount of catalyst, is usually spray-coated onto a carbon paper substrate as a working electrode. The hydrophobic microporous layer on carbon paper helps to form a uniform gas-liquid interface between the substrate and catalyst during the reaction. The microporous layer also helps to lower the ohmic contact resistances between porous layer and catalyst layer. The solubility of CO₂ in liquid aqueous electrolytes limits its transport rates to the reactive interface. This is why current density in CO₂-saturated liquid electrolytes⁴⁹ remains low. In contrast, a Gas Diffusion Electrode (GDE) set-up with a three-phase interface of electrolyte, catalyst and pressurized CO₂ inside the GDE offers a solution. With a catalyst loading of 1 mg cm⁻² on an active geometric surface area of 3 cm² GDE, constant current densities between 50 and 700 mA cm⁻² were applied galvanostatically to the cell in 1 M KHCO₃. Each current is held for 2 h before moving on to the next current step.

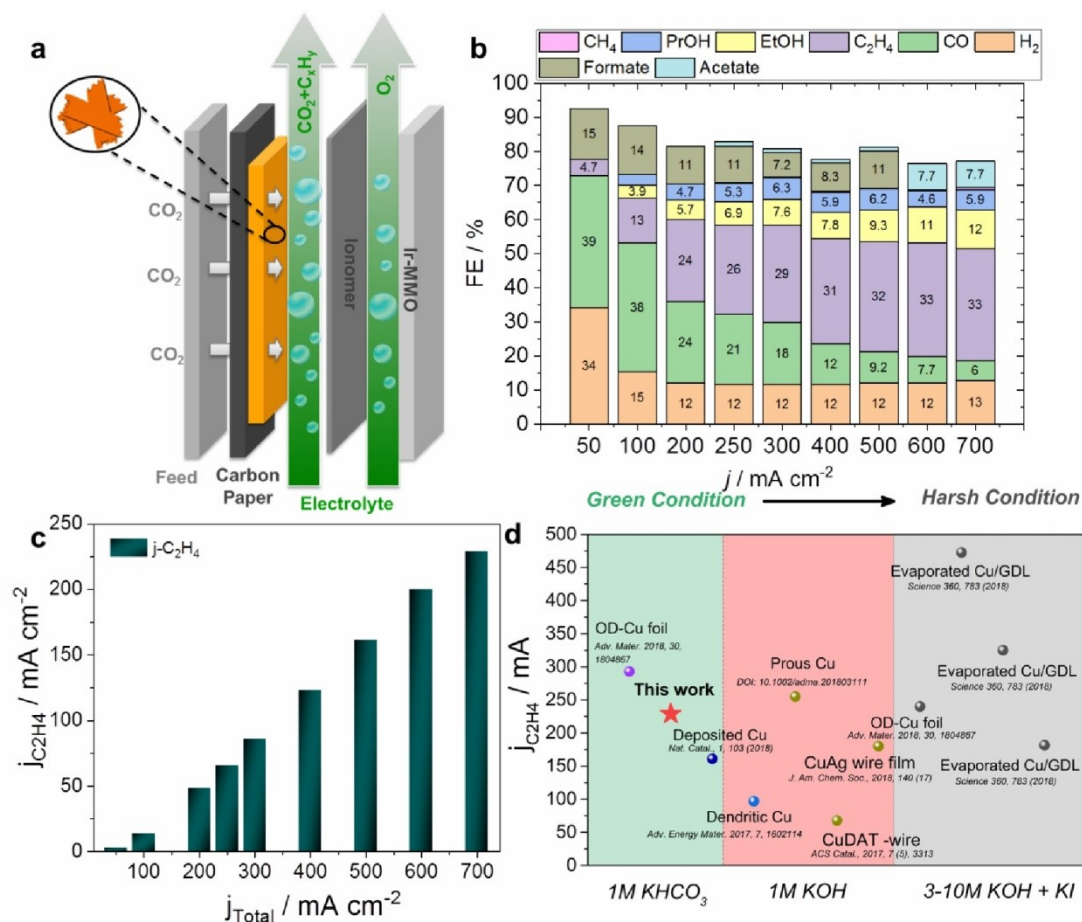


Figure 7.1 Electrochemical characterization in micro flow-cell configuration. a) Schematic representation of the Flow-Cell. b) FEs as a function of applied geometric current density for CuO_x NS with a catalyst loading of 1 mg/cm² in 1 M KHCO₃. c) Partial current density of C₂H₄ vs the total applied current density. d) Plot of ethylene partial current density in a flow-cell system (compared with references).

Figure 7.1b shows experimentally measured FEs of major CO₂RR products on CuO_x electrocatalyst as a function of the applied current densities. It shows a high selectivity towards CO₂RR exceeding 58 % and HER selectivity is only 13% at 700 mA cm⁻². The FE towards C₂H₄ exhibits an uphill trend with increase of applied current densities. Maintaining a constant FE of C₂H₄ as 33% at high current densities, the partial current of C₂H₄ is reported as 229 mA cm⁻² (at 700 mA cm⁻²) in mild condition (see figure 7.1c). The geometric partial current density towards C₂₊ products also reaches ~ 410 mA cm⁻² (at 700 mA cm⁻²) (see figure A4.1) CH₄ formation is suppressed at all current densities (0.58% at 700 mA cm⁻²), leading to unique C₂H₄ formation as single hydrocarbon product. Figure 7.1d compares the C₂H₄ partial current density in a flow-cell system reported in the literatures. Our catalyst is among the best

catalysts for CO₂RR in neutral condition with flow cell configuration. Note that we used nanoparticles for the GDE, which also brings the flexibility for the GDE design with tunable catalyst loading. While most studies focused on the electro-deposition system.

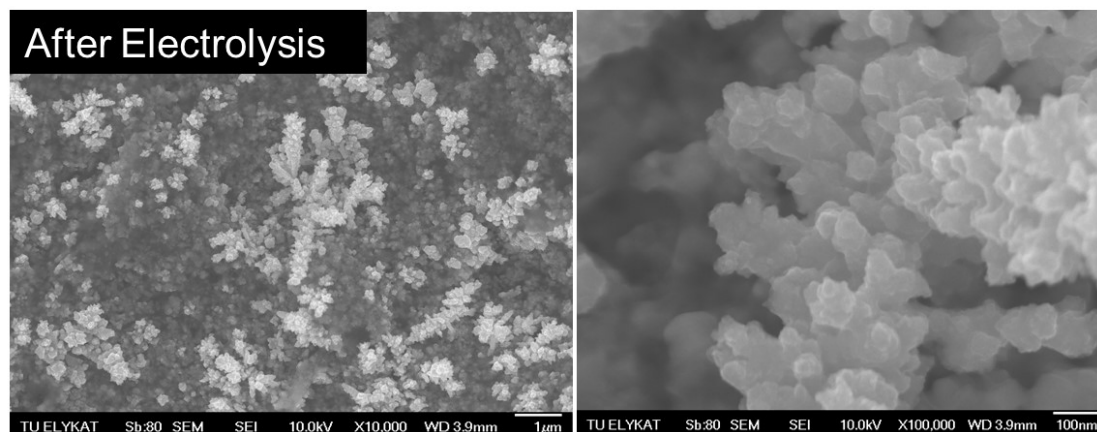


Figure 7.2 SEM image of CuO_x NS GDE after CO₂ electrolysis.

The electroreduction of CO₂ on a catalyst is almost always accompanied by a morphology evolution of the catalytic active material. SEM was employed to determine the morphology change of the GDE after the catalytic reaction. As shown in Figure 7.2, particle agglomeration and dendrite growth can be observed. Even though the CuO_x NS strongly reshaped during the CO₂ electrolysis process, the rough surfaces remained after the current-screening, which was considered to contribute continuously to the high activity and outstanding selectivity.

7.2 Discussions

The CuO_x NS catalyst reached a stable faradaic efficiency of ethylene, FE_{C₂H₄}, of nearly 30% when the applied current density reached 300 mA cm⁻². The catalyst and its GDE were able to maintain this FE efficiency even at higher current densities. A stability test was subsequently performed at 300 mA cm⁻² for 24 hours. The FE_{C₂H₄} reached 31% already after 4-hour test. Only a negligible decrease in C₂H₄ efficiency was observable after as long as 20 hours. Particle agglomeration and dendrite growth were observed by SEM after the long-term electrolysis. A control experiment was taken in H-cell configuration at similar overpotential (-1 V_{RHE}) for 24 h (see Figure A4.2), while no evident dendrites were observed in the SEM images, the observed aggregation was similar (see Figure A4.3).

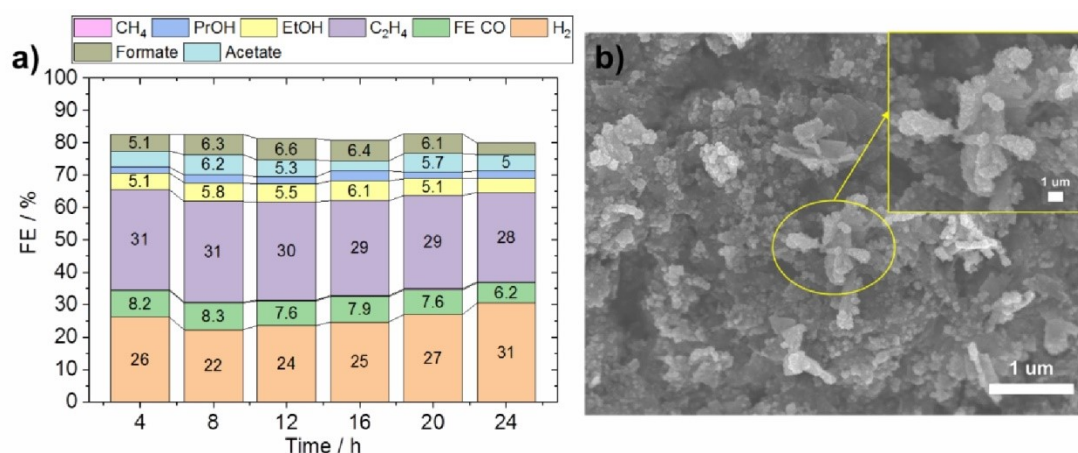


Figure 7.3 a) Gaseous products efficiencies with 300 mA cm^{-2} in CO_2 electrolyzer flow cell. All tests were performed with CO_2 saturated 1 M KHCO_3 and 1 mg cm^{-2} catalyst loading. b) SEM images after flow cell test.

The morphological restructuring of copper oxides catalysts during catalytic operation has been suggested to play an important role during the reaction. However, direct imaging of the morphological and structural evolution of reactive copper oxide catalysts has remained elusive. *In situ* microscopy technique offers us an exciting opportunity to trace the morphological evolution during the reaction. Figure 7.4a shows the interaction between the electron beam and CuO_x electrocatalyst in a customized microscopic electrochemical liquid cell setup. The cross-section scheme of the liquid cell holder is shown with the electrodes is given on the top chip. The quasi *in situ* TEM experiments were realized in a Protochips Poseidon holder, in which a three-component flow cell chip was inserted and equipped with a silicon nitride electron transparent window. Several control experiments were carried out first, because the typical K^+ -containing KHCO_3 electrolyte is known to be unsuitable for the silicon nitride window, risking of the membrane break (according to the user manual). Then CO_2 -saturated 0.1 M KHCO_3 was changed to $0.1 \text{ M Na}_2\text{HPO}_4/\text{NaH}_2\text{PO}_4$ ($\text{pH}=6.9$) to maintain a similar pH value. We performed 15-min CO_2 electrolysis in the H-cell with $0.1 \text{ M Na}_2\text{HPO}_4/\text{NaH}_2\text{PO}_4$. As we can see in Figure A4.4, the morphological evolution of the CuO_x NS catalyst does not depend on the interaction of CO_2 with the catalyst surface. The shape loss of CuO_x NS started already after 15 min seen by sheet cracking. Thus, $0.1 \text{ M Na}_2\text{HPO}_4/\text{NaH}_2\text{PO}_4$, without CO_2 feed is used for the following *quasi in situ* TEM experiments. Another reason to leave the CO_2 feed in the first experiment is that the gas bubbles in electrochemical liquid TEM micro reactor always cause short-circuit.

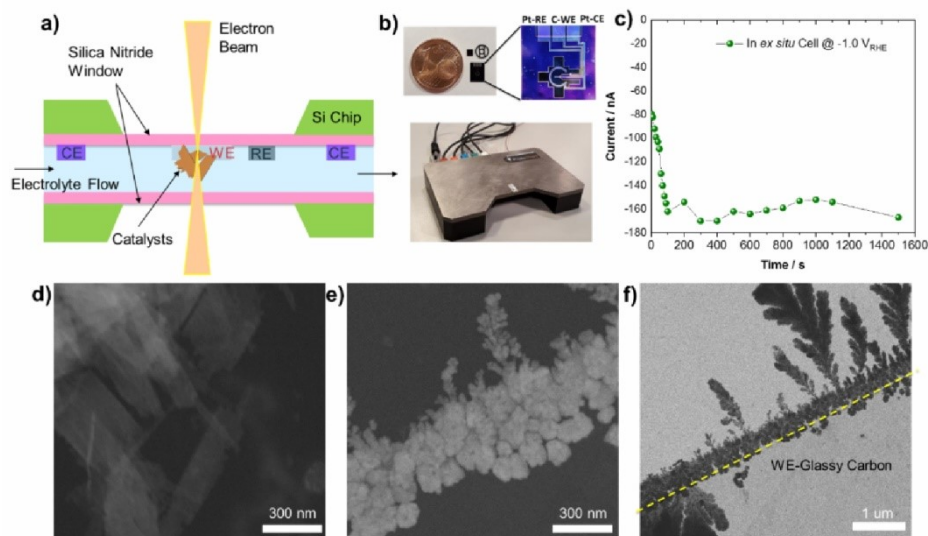


Figure 7.4 *in situ* Observation of dendrite growth after electrochemical reduction of CuO_x NS catalysts inside an electrochemical liquid cell TEM holder. a) Cross-section of the chip with the corresponding bottom chip and the electrolyte layer between the chips. b) Dimension of the electrochemistry chip (upper left), photography of top E chip (upper right) and *ex situ* test cell. c) Chronoamperometric performance in 0.1 M Na₂HPO₄/NaH₂PO₄ (pH=6.9) for 25 min. STEM image of CuO_x NS on electrochemistry chip d) before and e) after reduction. f) TEM image of CuO_x NS on electrochemistry chip after reduction.

Figure 7.4d represents the STEM image of CuO_x NS attached on the carbon working electrode of the top window of the electrochemical liquid TEM cell. After TEM imaging (Figure 7.4d), the whole chips, containing the top electrochemical chip, bottom chip and as well as a gasket, were transferred into the *ex situ* cell with a similar operating system for electrochemistry test. Chronoamperometric performance was then measured for 25 min in an *ex situ* electrochemical liquid TEM cell. A very similar CA curve was thereby obtained (Figure 7.4c) as that obtained in the H-cell. After rinsing, the *ex situ* cell was carefully unmounted and the same chip (“E-chip”) configuration was mounted into the electrochemical liquid TEM cell again for imaging. Figure 7.4 e,f show the direct images after electrochemistry of the CuO_x NS catalyst. Again, the sheet-like catalyst deshed and the particles agglomerated along the edge of the glassy carbon electrode. Moreover, the formation of clear dendrite was observed on the top E-chip. The quasi *in situ* data suggest particle evolution in liquid TEM cell agreed better with practical flow cell condition. We attribute this to the harsh electroreduction condition in both flow cell electrolyzer and liquid TEM micro reactor, where the current densities are quite high, comparing to the relative catalyst loading.

7.3 Conclusions

We have investigated the electrocatalytic reduction of CO₂ to selective C₂H₄ streams on CuO_x NS catalysts, with exposing predominantly {001} facets, in a Micro-Flow-Cell (MFC) configuration equipped with a Gas Diffusion Electrode (GDE). The catalyst poses a faradaic efficiency exceeding 33% ethylene at high current (700 mA cm⁻²) with suppressed HER. The partial current of C₂H₄ and C₂₊ reaches 229 and ~410 mA cm⁻², respectively. We then demonstrated the morphological transformations in an electrochemical liquid TEM cell set up. Dendrites growth was observed in both flow cell and liquid TEM cell due to the similar harsh electroreduction condition, which differs from the H-cell. Our *quasi in situ* experiment verified the feasibility of *in situ* microscopy technology for future investigation on catalytically morphology evolution under CO₂RR operating conditions at industry relevant current levels.

Chapter 8 Summary and Outlook

The present Dissertation set out to establish a new in-depth understanding of CO₂ electroreduction reactivity on known and new catalysts with high C₂₊ product selectivity. By adjusting the local environment of our studied CuO_x nanoparticle model catalysts, including tuning the particle assembles and introducing co-reactant-gas-feeding system, we were able to uncover the Critical role of local interfacial CO concentrations and, using advanced electrochemical mass spectrometry, succeeded in deducing previously unavailable details of the reaction mechanism and the relative contribution of reactive pathways. Beyond this fundamental investigation, novel tandem catalysts, consisting of the C₂ product selective CuO_x nanoparticles in combination with a selective CO producer (such as Ag or a novel non-metallic NiNC carbon catalyst), have delivered significant enhancements in ethylene production and yield in comparison to CuO_x and NiNC control catalysts. More importantly, a new type of sheet-shaped CuO_x nanoparticles was designed, developed and systematically investigated based on the knowledge found in this work, and its impressive performance for ethylene formation was further demonstrated in both liquid H-cell configuration and industry-relevant micro flow cell. Moreover, a combination of *operando*/(*quasi*) *in situ* techniques were used to discovery the morphology-structure-phase-activity-selectivity relationship.

8.1 Manipulating *CO behavior by local condition

Recalling the importance of *CO formed after 2e⁻ transfer process during CO₂ feed, which can be followed by a protonation pathway to CH₄ or dimerization pathway to C₂H₄ (as illustrated in Figure 8.1).

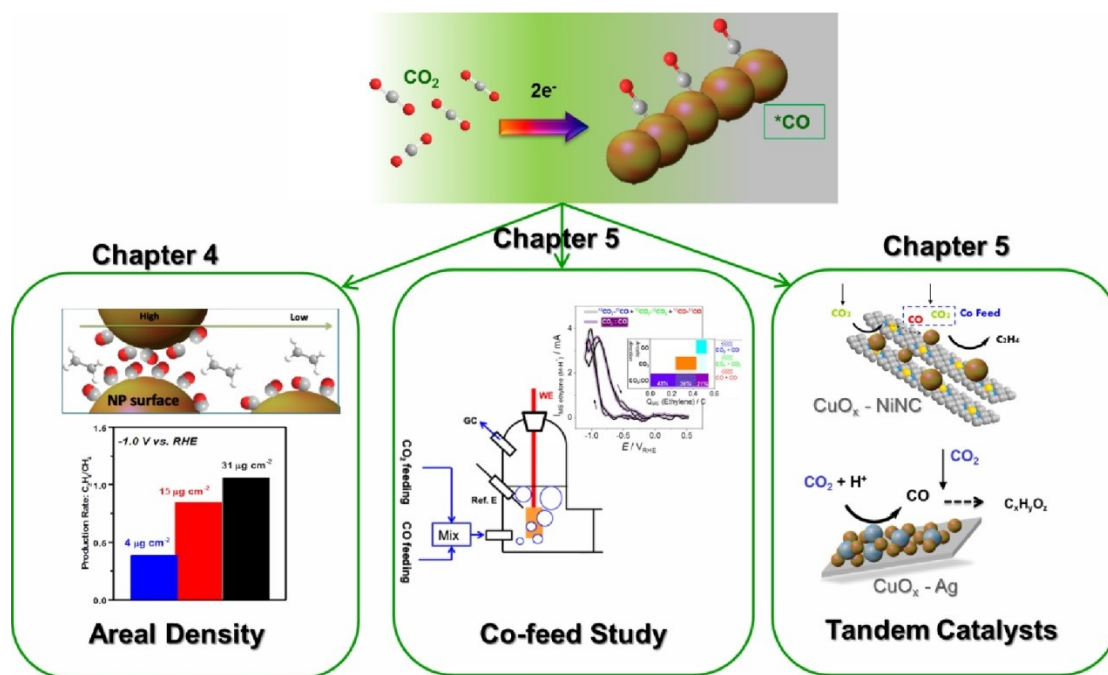


Figure 8.1 Graphical summary of topics and issues discussed and investigated in the first part of work, including areal density control, mechanistic co-feed study, and tandem catalyst. (Reprinted with permission from The John Wiley and Sons and Springer Nature)^{126,127}

We started our mechanistic study on particle assemblies, aiming to control re-adsorption behavior of $*\text{CO}$ (see Chapter 4). In this contribution, tunable product distribution of ethylene and methane during CO_2 electroreduction is observed by simply adjusting the areal particle density. As CO_2RR is a multiple proton and electron reaction, the desorption, diffusional transport and possible re-adsorption of chemical reaction intermediates or products on closely spaced particles may result in variations in product selectivity. By increasing the areal NP density, the mean interparticle distances decrease and the real surface-area increases as deduced from geometric voltammetric current scans. A shift in Faradic efficiency towards C_2H_4 over CH_4 in higher areal density is observed. This observation is attributed to higher dimerization rates of adsorbed $*\text{CO}$ at smaller interparticle distances and more surface active sites, which enhanced $\text{CO}(\text{g})$ re-adsorption on NP in close proximity. The following catalytic performance tests over extended reaction times corroborate the role of interparticle distances. To further increase the local concentration of $\text{CO}(\text{g})$, a CO_2 with CO co-feeding system was then investigated (see Chapter 5). In this part, the electrochemical reduction of “modified gas feed” (CO_2 with CO co-feeding) is systematically investigated on uniform and catalytically active Cu oxide NPs as a promising method to improve C_2H_4 formation over a wide electrode

potential range. Using a custom-designed DEMS flow cell, carbon origins of C_2H_4 in the co-feed system were successfully identified by isotope labelling of one of the carbon species from the co-feed (^{12}C and ^{13}C). Our analysis demonstrated for the first time that the enhanced C_2H_4 production mainly originated from a kinetically favored CO_2 -CO crossed combination pathway. Our study highlights the role of extra CO on the ethylene product, indicating additional channels for ethylene production opened up without affecting the existing pathways. The co-feed mechanism inspired a new fabrication of catalysts with a CO-maker catalyst and copper-based material, yielding high selectivity to hydrocarbons with a facile preparation method.

8.2 Shaped CuO_x nanoparticles for CO2RR

Our focus moved to new catalyst development in the second part of this work. A new type of sheet-like copper oxide nanoparticles with preferred $\{001\}$ orientation was successfully synthesized and first applied for CO2RR in an H-cell configuration (see Chapter 6). The highly active CuO_x nanoparticles exhibit outstanding stability and selectivity towards ethylene. A combination of (*in situ/operando*) WAXS and XAS were used to examine the phase/local atomic structure evolution of as-prepared CuO_x electrocatalyst under operating CO2RR electrolysis condition. Millisecond-resolved *operando* DEMS was employed to determine the onset potential shift of the products with gradually self-electroreduced CuO_x electrocatalyst to a purely metallic Cu phase. *Ex situ* SEM measurements showed that the initial sheet-like morphology de-shaped during the reduction reaction and progressing particle aggregation in the H-cell, while unaffected the catalytic performance. These results suggest that the improved catalytic performance for oxide-derived copper catalyst arise from a combination of the increased content of metallic copper induced under-coordinated sites, and the stable, high local pH created through nanostructured morphology.

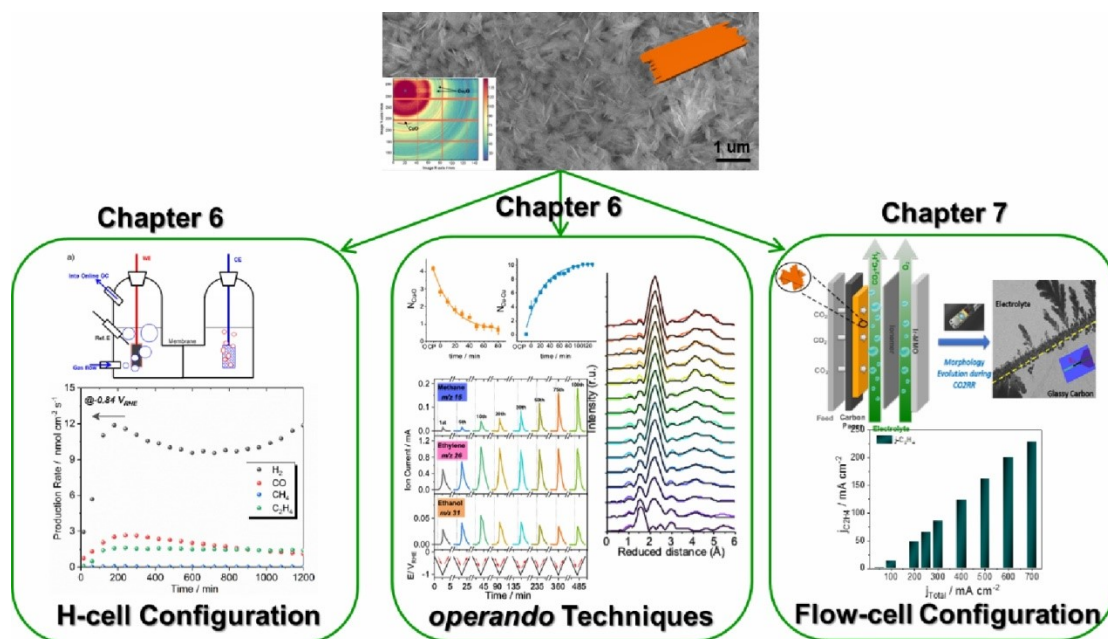


Figure 8.2 Graphical summary of topics and issues discussed and investigated in the second part of this work, including shaped CuO_x nanoparticles synthesis, characterization, H-cell tests, a combination of *operando* studies, and flow cell test at industrial relevant level.

To reach the industrial level CO_2 electrolysis, performance exhibited in common H-type cell is far from sufficient, mostly due to mass transfer limitations of the CO_2 reactant. Thus, micro flow cell experiments were done in a following-up work (see Chapter 7). The catalyst exhibited a stable faradaic efficiency towards ethylene exceeding 33 %. The partial current of C_2H_4 and C_{2+} reached 229 and 356 mA cm^{-2} , respectively, obtaining as an excellent catalyst for ethylene under neutral condition. Our study on morphological transformations of free-standing CuO_x nanosheets was done in electrochemical liquid TEM micro reactor. Dendrite growth caused by harsh electroreduction conditions was observed in both flow cell and liquid TEM cell experiments, which differs from observations in the H-cell. Our data suggest the particle evolution in liquid TEM cell agreed better with the micro flow cell due to similar practical flow conditions. The present study corroborates the power of *in situ* electrochemical liquid TEM studies for the understanding of morphology-activity-selectivity relations under catalytic CO_2RR operating conditions at the industry level.

8.3 Outlook

An unprecedented contribution towards understanding the mechanism in pure CO₂ reduction reactions was provided in this work, offering new guidelines for obtaining active and stable electrocatalysts. However, it still remains a challenge to selectively form a single product with extended catalyst stability on Cu-based electrocatalysts. Currently, most of the catalysts are screened in H-cell devices. The mass transfer limitation shown in the H-cell is often considered as a barrier for continuously large scale operation of CO₂ electrolysis. To solve this problem, the translation to flow cell has proven to be a highly effective method for the development of industrial scale electrochemical reactors. The continuously circulated gas and liquid flow in the flow cell reactor, moving reactants and products to and away from the electrodes, helps to break the mass transport limitations. Therefore, further investigations in flow cell reactors with Cu-based catalysts, together with new catalyst development, provide an opportunity for the practical application from lab scale to industrial scale.⁵¹

Reference

1. Li F, MacFarlane DR, Zhang J. Recent advances in the nanoengineering of electrocatalysts for CO₂ reduction. *Nanoscale* 2018, 10(14): 6235-6260.
2. Shi J, Jiang Y, Jiang Z, Wang X, Wang X, Zhang S, *et al.* Enzymatic conversion of carbon dioxide. *Chemical Society Reviews* 2015, 44(17): 5981-6000.
3. Qiao J, Liu Y, Hong F, Zhang J. A review of catalysts for the electroreduction of carbon dioxide to produce low-carbon fuels. *Chemical Society Reviews* 2014, 43(2): 631-675.
4. Costentin C, Robert M, Saveant J-M. Catalysis of the electrochemical reduction of carbon dioxide. *Chemical Society Reviews* 2013, 42(6): 2423-2436.
5. Spinner NS, Vega JA, Mustain WE. Recent progress in the electrochemical conversion and utilization of CO₂. *Catalysis Science & Technology* 2012, 2(1): 19-28.
6. Jitaru M, Lowy DA, Toma M, Toma BC, Oniciu L. Electrochemical reduction of carbon dioxide on flat metallic cathodes. *Journal of Applied Electrochemistry* 1997, 27(8): 875-889.
7. Annual Energy Outlook 2019. US Energy Information Administration Office of Energy Analysis 2019.
8. Renewable capacity statistics 2019. International Renewable Energy Agency (IRENA), Abu Dhabi.
9. Benson EE, Kubiak CP, Sathrum AJ, Smieja JM. Electrocatalytic and homogeneous approaches to conversion of CO₂ to liquid fuels. *Chemical Society Reviews* 2009, 38(1): 89-99.
10. Inglis JL, MacLean BJ, Pryce MT, Vos JG. Electrocatalytic pathways towards sustainable fuel production from water and CO₂. *Coordination Chemistry Reviews* 2012, 256(21-22): 2571-2600.
11. Goepfert A, Czaun M, Jones J-P, Surya Prakash GK, Olah GA. Recycling of carbon dioxide to methanol and derived products - closing the loop. *Chemical Society Reviews* 2014, 43(23): 7995-8048.
12. Albo J, Alvarez-Guerra M, Castano P, Irabien A. Towards the electrochemical conversion of carbon dioxide into methanol. *Green Chemistry* 2015, 17(4): 2304-2324.
13. Li Y, Sun Q. Recent Advances in Breaking Scaling Relations for Effective Electrochemical Conversion of CO₂. *Advanced Energy Materials* 2016, 6(17): 1600463.
14. Elgrishi N, Chambers MB, Wang X, Fontecave M. Molecular polypyridine-based metal complexes as catalysts for the reduction of CO₂. *Chemical Society Reviews* 2017, 46(3): 761-796.
15. Handoko AD, Wei F, Jenndy, Yeo BS, Seh ZW. Understanding heterogeneous electrocatalytic carbon dioxide reduction through *operando* techniques. *Nature Catalysis* 2018, 1(12): 922-934.

16. Mota FM, Kim DH. From CO₂ methanation to ambitious long-chain hydrocarbons: alternative fuels paving the path to sustainability. *Chemical Society Reviews* 2019, 48(1): 205-259.
17. Jouny M, Luc W, Jiao F. General Techno-Economic Analysis of CO₂ Electrolysis Systems. *Industrial & Engineering Chemistry Research* 2018, 57(6): 2165-2177.
18. Higgins D, Hahn C, Xiang C, Jaramillo TF, Weber AZ. Gas-Diffusion Electrodes for Carbon Dioxide Reduction: A New Paradigm. *ACS Energy Letters* 2019, 4(1): 317-324.
19. Zheng T, Jiang K, Ta N, Hu Y, Zeng J, Liu J, *et al.* Large-Scale and Highly Selective CO₂ Electrocatalytic Reduction on Nickel Single-Atom Catalyst. *Joule* 2019, 3(1): 265-278.
20. Hori Y. Electrochemical CO₂ Reduction on Metal Electrodes. vol. 42, 2008, pp 89-189.
21. Kuhl KP, Hatsukade T, Cave ER, Abram DN, Kibsgaard J, Jaramillo TF. Electrocatalytic Conversion of Carbon Dioxide to Methane and Methanol on Transition Metal Surfaces. *Journal of the American Chemical Society* 2014, 136(40): 14107-14113.
22. Zhang Y-J, Sethuraman V, Michalsky R, Peterson AA. Competition between CO₂ Reduction and H₂ Evolution on Transition-Metal Electrocatalysts. *Acs Catalysis* 2014, 4(10): 3742-3748.
23. Kim D, Resasco J, Yu Y, Asiri AM, Yang P. Synergistic geometric and electronic effects for electrochemical reduction of carbon dioxide using gold-copper bimetallic nanoparticles. *Nature Communications* 2014, 5: 4948.
24. Lum Y, Kwon Y, Lobaccaro P, Chen L, Clark EL, Bell AT, *et al.* Trace Levels of Copper in Carbon Materials Show Significant Electrochemical CO₂ Reduction Activity. *Acs Catalysis* 2016, 6(1): 202-209.
25. Singh MR, Kwon Y, Lum Y, Ager JW, III, Bell AT. Hydrolysis of Electrolyte Cations Enhances the Electrochemical Reduction of CO₂ over Ag and Cu. *Journal of the American Chemical Society* 2016, 138(39): 13006-13012.
26. Clark EL, Hahn C, Jaramillo TF, Bell AT. Electrochemical CO₂ Reduction over Compressively Strained CuAg Surface Alloys with Enhanced Multi-Carbon Oxygenate Selectivity. *Journal of the American Chemical Society* 2017, 139(44): 15848-15857.
27. Higgins D, Landersp AT, Ji Y, Nitopi S, Morales-Guio CG, Wang L, *et al.* Guiding Electrochemical Carbon Dioxide Reduction toward Carbonyls Using Copper Silver Thin Films with Interphase Miscibility. *Acs Energy Letters* 2018, 3(12): 2947-2955.
28. Morales-Guio CG, Cave ER, Nitopi SA, Feaster JT, Wang L, Kuhl KP, *et al.* Improved CO₂ reduction activity towards C₂₊ alcohols on a tandem gold on copper electrocatalyst. *Nature Catalysis* 2018, 1(10): 764-771.
29. Zeng J, Bejtka K, Ju W, Castellino M, Chiodoni A, Sacco A, *et al.* Advanced Cu-Sn foam for selectively converting CO₂ to CO in aqueous solution. *Applied Catalysis B-Environmental* 2018, 236: 475-482.

30. Zhu W, Zhang L, Yang P, Hu C, Dong H, Zhao Z-J, *et al.* Formation of Enriched Vacancies for Enhanced CO₂ Electrocatalytic Reduction over AuCu Alloys. *Acs Energy Letters* 2018, 3(9): 2144-2149.
31. Huang J, Mensi M, Oveisi E, Mantella V, Buonsanti R. Structural Sensitivities in Bimetallic Catalysts for Electrochemical CO₂ Reduction Revealed by Ag-Cu Nanodimers. *Journal of the American Chemical Society* 2019, 141(6): 2490-2499.
32. Chen Y, Li CW, Kanan MW. Aqueous CO₂ Reduction at Very Low Overpotential on Oxide-Derived Au Nanoparticles. *Journal of the American Chemical Society* 2012, 134(49): 19969-19972.
33. Zhu W, Michalsky R, Metin O, Lv H, Guo S, Wright CJ, *et al.* Monodisperse Au Nanoparticles for Selective Electrocatalytic Reduction of CO₂ to CO. *Journal of the American Chemical Society* 2013, 135(45): 16833-16836.
34. Mistry H, Reske R, Zeng Z, Zhao Z-J, Greeley J, Strasser P, *et al.* Exceptional Size-Dependent Activity Enhancement in the Electroreduction of CO₂ over Au Nanoparticles. *Journal of the American Chemical Society* 2014, 136(47): 16473-16476.
35. Zhu W, Zhang Y-J, Zhang H, Lv H, Li Q, Michalsky R, *et al.* Active and Selective Conversion of CO₂ to CO on Ultrathin Au Nanowires. *Journal of the American Chemical Society* 2014, 136(46): 16132-16135.
36. Kim C, Jeon HS, Eom T, Jee MS, Kim H, Friend CM, *et al.* Achieving Selective and Efficient Electrocatalytic Activity for CO₂ Reduction Using Immobilized Silver Nanoparticles. *Journal of the American Chemical Society* 2015, 137(43): 13844-13850.
37. Kumar B, Asadi M, Pisasale D, Sinha-Ray S, Rosen BA, Haasch R, *et al.* Renewable and metal-free carbon nanofibre catalysts for carbon dioxide reduction. *Nature Communications* 2013, 4: 2819.
38. Mao X, Hatton TA. Recent Advances in Electrocatalytic Reduction of Carbon Dioxide Using Metal-Free Catalysts. *Industrial & Engineering Chemistry Research* 2015, 54(16): 4033-4042.
39. Wu J, Ma S, Sun J, Gold JI, Tiwary C, Kim B, *et al.* A Metal-free electrocatalyst for Carbon Dioxide Reduction to Multi-carbon Hydrocarbons and Oxygenates. *Nature Communications* 2016, 7: 13869.
40. Xie J, Zhao X, Wu M, Li Q, Wang Y, Yao J. Metal - Free Fluorine - Doped Carbon Electrocatalyst for CO₂ Reduction Outcompeting Hydrogen Evolution. *Angewandte Chemie International Edition* 2018, 57(31): 9640-9644.
41. Zhang S, Kang P, Ubnoske S, Brennaman MK, Song N, House RL, *et al.* Polyethylenimine-Enhanced Electrocatalytic Reduction of CO₂ to Formate at Nitrogen-Doped Carbon Nanomaterials. *Journal of the American Chemical Society* 2014, 136(22): 7845-7848.
42. Wu J, Yadav RM, Liu M, Sharma PP, Tiwary CS, Ma L, *et al.* Achieving Highly Efficient, Selective, and Stable CO₂ Reduction on Nitrogen-Doped Carbon Nanotubes. *Acs Nano* 2015, 9(5): 5364-5371.
43. Zheng T, Jiang K, Wang H. Recent Advances in Electrochemical CO₂-to-CO Conversion on Heterogeneous Catalysts. *Advanced Materials* 2018, 30(48): 1802066.

44. Siahrostami S. Designing Carbon-Based Materials for Efficient Electrochemical Reduction of CO₂. *Industrial & Engineering Chemistry Research* 2019, 58(2): 879-885.
45. Zhu DD, Liu JL, Qiao SZ. Recent Advances in Inorganic Heterogeneous Electrocatalysts for Reduction of Carbon Dioxide. *Advanced Materials* 2016, 28(18): 3423-3452.
46. Liu J, Ma Q, Huang Z, Liu G, Zhang H. Recent Progress in Graphene-Based Noble-Metal Nanocomposites for Electrocatalytic Applications. *Advanced Materials* 2019, 31(9): 1800696.
47. Ju W, Bagger A, Hao G-P, Varela AS, Sinev I, Bon V, *et al.* Understanding Activity and Selectivity of Metal-nitrogen-doped Carbon Catalysts for Electrochemical Reduction of CO₂. *Nature Communications* 2017, 8(1): 944.
48. Huan TN, Ranjbar N, Rousse G, Sougrati M, Zitolo A, Mougél V, *et al.* Electrochemical Reduction of CO₂ Catalyzed by Fe-N-C Materials: A Structure-Selectivity Study. *Acs Catalysis* 2017, 7(3): 1520-1525.
49. Moeller T, Ju W, Bagger A, Wang X, Luo F, Trung Ngo T, *et al.* Efficient CO₂ to CO Electrolysis on Solid Ni-N-C Catalysts at Industrial Current Densities. *Energy & Environmental Science* 2019, 12(2): 640-647.
50. Hori Y, Wakebe H, Tsukamoto T, Koga O. Electrocatalytic Process of CO Selectivity in Electrochemical Reduction of CO₂ at Metal Electrodes in Aqueous Media. *Electrochimica Acta* 1994, 39(11-12): 1833-1839.
51. Kim C, Dionigi F, Beermann V, Wang X, Möller T, Strasser P. Alloy Nanocatalysts for the Electrochemical Oxygen Reduction (ORR) and the Direct Electrochemical Carbon Dioxide Reduction Reaction (CO₂RR). *Advanced Materials* 2018: 1805617.
52. Yoshio H, Katsuhei K, Akira M, Shin S. Production of Methane and Ethylene in Electrochemical Reduction of Carbon Dioxide at Copper Electrode in Aqueous Hydrogencarbonate Solution. *Chemistry Letters* 1986, 15(6): 897-898.
53. Murata A, Hori Y. Product Selectivity Affected by Cationic Species in Electrochemical Reduction of CO₂ and CO at a Cu Electrode. *Bulletin of the Chemical Society of Japan* 1991, 64(1): 123-127.
54. Hori Y, Takahashi R, Yoshinami Y, Murata A. Electrochemical Reduction of CO at a Copper Electrode. *Journal of Physical Chemistry B* 1997, 101(36): 7075-7081.
55. Hori Y, Takahashi I, Koga O, Hoshi N. Electrochemical Reduction of Carbon Dioxide at Various Series of Copper Single Crystal Electrodes. *Journal of Molecular Catalysis A: Chemical* 2003, 199(1-2): 39-47.
56. Tang W, Peterson AA, Varela AS, Jovanov ZP, Bech L, Durand WJ, *et al.* The Importance of Surface Morphology in Controlling the Selectivity of Polycrystalline Copper for CO₂ Electroreduction. *Physical Chemistry Chemical Physics* 2012, 14(1): 76-81.
57. Guo H, Chen Y, Cortie MB, Liu X, Xie Q, Wang X, *et al.* Shape-Selective Formation of Monodisperse Copper Nanospheres and Nanocubes via Disproportionation Reaction Route and Their Optical Properties. *The Journal of Physical Chemistry C* 2014, 118(18): 9801-9808.

58. Schouten KJP, Gallent EP, Koper MT. The Influence of pH on the Reduction of CO and CO₂ to Hydrocarbons on Copper Electrodes. *J Electroanal Chem* 2014, 716: 53-57.
59. Sen S, Liu D, Palmore GTR. Electrochemical Reduction of CO₂ at Copper Nanofoams. *Acs Catalysis* 2014, 4(9): 3091-3095.
60. Kas R, Kortlever R, Yilmaz H, Koper MTM, Mul G. Manipulating the Hydrocarbon Selectivity of Copper Nanoparticles in CO₂ Electroreduction by Process Conditions. *ChemElectroChem* 2015, 2(3): 354-358.
61. Figueiredo MC, Ledezma-Yanez I, Koper MTM. *In situ* Spectroscopic Study of CO₂ Electroreduction at Copper Electrodes in Acetonitrile. *Acs Catalysis* 2016, 6(4): 2382-2392.
62. Ledezma-Yanez I, Gallent EP, Koper MTM, Calle-Vallejo F. Structure-sensitive Electroreduction of Acetaldehyde to Ethanol on Copper and Its Mechanistic Implications for CO and CO₂ Reduction. *Catalysis Today* 2016, 262: 90-94.
63. Varela AS, Kroschel M, Reier T, Strasser P. Controlling the Selectivity of CO₂ Electroreduction on Copper: The Effect of the Electrolyte Concentration and the Importance of the Local pH. *Catalysis Today* 2016, 260: 8-13.
64. Wang Z, Yang G, Zhang Z, Jin M, Yin Y. Selectivity on Etching: Creation of High-Energy Facets on Copper Nanocrystals for CO₂ Electrochemical Reduction. *ACS Nano* 2016, 10(4): 4559-4564.
65. Kim D, Kley CS, Li Y, Yang P. Copper Nanoparticle Ensembles for Selective Electroreduction of CO₂ to C₂-C₃ products. *Proceedings of the National Academy of Sciences of the United States of America* 2017, 114(40): 10560-10565.
66. Li Y, Cui F, Ross MB, Kim D, Sun Y, Yang P. Structure-Sensitive CO₂ Electroreduction to Hydrocarbons on Ultrathin 5-fold Twinned Copper Nanowires. *Nano Letters* 2017, 17(2): 1312-1317.
67. Bertheussen E, Hogg TV, Abghoui Y, Engstfeld AK, Chorkendorff I, Stephens IEL. Electroreduction of CO on Polycrystalline Copper at Low Overpotentials. *Acs Energy Letters* 2018, 3(3): 634-640.
68. Reske R, Mistry H, Behafarid F, Roldan Cuenya B, Strasser P. Particle Size Effects in the Catalytic Electroreduction of CO₂ on Cu Nanoparticles. *Journal of the American Chemical Society* 2014, 136(19): 6978-6986.
69. Mistry H, Varela AS, Bonifacio CS, Zegkinoglou I, Sinev I, Choi Y-W, *et al.* Highly Selective Plasma-activated Copper Catalysts for Carbon Dioxide Reduction to Ethylene. *Nature Communications* 2016, 7: 12123.
70. Varela AS, Ju W, Reier T, Strasser P. Tuning the Catalytic Activity and Selectivity of Cu for CO₂ Electroreduction in the Presence of Halides. *ACS Catalysis* 2016, 6(4): 2136-2144.
71. Somorjai GA. Catalysis on the Atomic Scale (Emmett Award Lecture of 1977). *Catalysis Reviews* 1978, 18(2): 173-197.
72. Peterson AA, Abild-Pedersen F, Studt F, Rossmeisl J, Norskov JK. How Copper Catalyzes the Electroreduction of Carbon Dioxide into Hydrocarbon Fuels. *Energy & Environmental Science* 2010, 3(9): 1311-1315.

73. Peterson AA, Nørskov JK. Activity Descriptors for CO₂ Electroreduction to Methane on Transition-Metal Catalysts. *The Journal of Physical Chemistry Letters* 2012, 3(2): 251-258.
74. Kortlever R, Shen J, Schouten KJP, Calle-Vallejo F, Koper MTM. Catalysts and Reaction Pathways for the Electrochemical Reduction of Carbon Dioxide. *Journal of Physical Chemistry Letters* 2015, 6(20): 4073-4082.
75. Huang Y, Handoko AD, Hirunsit P, Yeo BS. Electrochemical Reduction of CO₂ Using Copper Single-Crystal Surfaces: Effects of CO* Coverage on the Selective Formation of Ethylene. *ACS Catalysis* 2017, 7(3): 1749-1756.
76. Cheng T, Xiao H, Goddard WA, III. Full Atomistic Reaction Mechanism with Kinetics for CO Reduction on Cu(100) From ab initio Molecular Dynamics Free-energy Calculations at 298 K. *Proceedings of the National Academy of Sciences of the United States of America* 2017, 114(8): 1795-1800.
77. Goodpaster JD, Bell AT, Head-Gordon M. Identification of Possible Pathways for C-C Bond Formation during Electrochemical Reduction of CO₂: New Theoretical Insights from an Improved Electrochemical Model. *Journal of Physical Chemistry Letters* 2016, 7(8): 1471-1477.
78. Garza AJ, Bell AT, Head-Gordon M. Mechanism of CO₂ Reduction at Copper Surfaces: Pathways to C₂ Products. *Acs Catalysis* 2018, 8(2): 1490-1499.
79. Cheng T, Xiao H, Goddard WA, III. Reaction Mechanisms for the Electrochemical Reduction of CO₂ to CO and Formate on the Cu(100) Surface at 298 K from Quantum Mechanics Free Energy Calculations with Explicit Water. *Journal of the American Chemical Society* 2016, 138(42): 13802-13805.
80. Xiao H, Cheng T, Goddard WA, III. Atomistic Mechanisms Underlying Selectivities in C₁ and C₂ Products from Electrochemical Reduction of CO on Cu(111). *Journal of the American Chemical Society* 2017, 139(1): 130-136.
81. Montoya JH, Peterson AA, Nørskov JK. Insights into C-C Coupling in CO₂ Electroreduction on Copper Electrodes. *ChemCatChem* 2013, 5(3): 737-742.
82. Schouten KJP, Kwon Y, van der Ham CJM, Qin Z, Koper MTM. A New Mechanism for the Selectivity to C₁ and C₂ Species in the Electrochemical Reduction of Carbon Dioxide on Copper Electrodes. *Chemical Science* 2011, 2(10): 1902-1909.
83. Kuhl KP, Cave ER, Abram DN, Jaramillo TF. New Insights into the Electrochemical Reduction of Carbon Dioxide on Metallic Copper Surfaces. *Energy & Environmental Science* 2012, 5(5): 7050-7059.
84. Calle-Vallejo F, Koper MTM. Theoretical Considerations on the Electroreduction of CO to C₂ Species on Cu(100) Electrodes. *Angewandte Chemie-International Edition* 2013, 52(28): 7282-7285.
85. Nie X, Esopi MR, Janik MJ, Asthagiri A. Selectivity of CO₂ Reduction on Copper Electrodes: The Role of the Kinetics of Elementary Steps. *Angewandte Chemie-International Edition* 2013, 52(9): 2459-2462.
86. Montoya JH, Shi C, Chan K, Nørskov JK. Theoretical Insights into a CO Dimerization Mechanism in CO₂ Electroreduction. *Journal of Physical Chemistry Letters* 2015, 6(11): 2032-2037.

87. Durand WJ, Peterson AA, Studt F, Abild-Pedersen F, Nørskov JK. Structure Effects on the Energetics of the Electrochemical Reduction of CO₂ by Copper Surfaces. *Surface Science* 2011, 605(15): 1354-1359.
88. Nie X, Luo W, Janik MJ, Asthagiri A. Reaction Mechanisms of CO₂ Electrochemical Reduction on Cu(111) Determined with Density Functional Theory. *Journal of Catalysis* 2014, 312: 108-122.
89. Luo W, Nie X, Janik MJ, Asthagiri A. Facet Dependence of CO₂ Reduction Paths on Cu Electrodes. *Acs Catalysis* 2016, 6(1): 219-229.
90. Huang Y, Ong CW, Yeo BS. Effects of Electrolyte Anions on the Reduction of Carbon Dioxide to Ethylene and Ethanol on Copper (100) and (111) Surfaces. *Chemsuschem* 2018, 11(18): 3299-3306.
91. Tsang CF, Javier AC, Kim Y-G, Baricuatro JH, Cummins KD, Kim J, *et al.* Potential-Dependent Adsorption of CO and Its Low-Overpotential Reduction to CH₃CH₂OH on Cu(511) Surface Reconstructed from Cu(pc): *Operando* Studies by Seriatim STM-EQCN-DEMS. *Journal of the Electrochemical Society* 2018, 165(15): J3350-J3354.
92. Li CW, Kanan MW. CO₂ Reduction at Low Overpotential on Cu Electrodes Resulting from the Reduction of Thick Cu₂O Films. *Journal of the American Chemical Society* 2012, 134(17): 7231-7234.
93. Li CW, Ciston J, Kanan MW. Electroreduction of Carbon Monoxide to Liquid Fuel on Oxide-derived Nanocrystalline Copper. *Nature* 2014, 508: 504.
94. Verdaguier-Casadevall A, Li CW, Johansson TP, Scott SB, McKeown JT, Kumar M, *et al.* Probing the Active Surface Sites for CO Reduction on Oxide-Derived Copper Electrocatalysts. *Journal of the American Chemical Society* 2015, 137(31): 9808-9811.
95. Manthiram K, Beberwyck BJ, Aivisatos AP. Enhanced Electrochemical Methanation of Carbon Dioxide with a Dispersible Nanoscale Copper Catalyst. *Journal of the American Chemical Society* 2014, 136(38): 13319-13325.
96. Chen CS, Handoko AD, Wan JH, Ma L, Ren D, Yeo BS. Stable and Selective Electrochemical Reduction of Carbon Dioxide to Ethylene on Copper Mesocrystals. *Catalysis Science & Technology* 2015, 5(1): 161-168.
97. Dutta A, Rahaman M, Luedi NC, Mohos M, Broekmann P. Morphology Matters: Tuning the Product Distribution of CO₂ Electroreduction on Oxide-Derived Cu Foam Catalysts. *ACS Catalysis* 2016, 6(6): 3804-3814.
98. Handoko AD, Ong CW, Huang Y, Lee ZG, Lin L, Panetti GB, *et al.* Mechanistic Insights into the Selective Electroreduction of Carbon Dioxide to Ethylene on Cu₂O-derived Copper Catalysts. *The Journal of Physical Chemistry C* 2016, 120(36): 20058-20067.
99. Ren D, Ang BS-H, Yeo BS. Tuning the Selectivity of Carbon Dioxide Electroreduction toward Ethanol on Oxide-Derived Cu_xZn Catalysts. *Acs Catalysis* 2016, 6(12): 8239-8247.
100. Eilert A, Cavalca F, Roberts FS, Osterwalder J, Liu C, Favaro M, *et al.* Subsurface Oxygen in Oxide-Derived Copper Electrocatalysts for Carbon Dioxide Reduction. *The Journal of Physical Chemistry Letters* 2017, 8(1): 285-290.

101. Liu C, Lourenço MP, Hedström S, Cavalca F, Diaz-Morales O, Duarte HA, *et al.* Stability and Effects of Subsurface Oxygen in Oxide-Derived Cu Catalyst for CO₂ Reduction. *The Journal of Physical Chemistry C* 2017, 121(45): 25010-25017.
102. Lum Y, Yue B, Lobaccaro P, Bell AT, Ager JW. Optimizing C–C Coupling on Oxide-Derived Copper Catalysts for Electrochemical CO₂ Reduction. *The Journal of Physical Chemistry C* 2017, 121(26): 14191-14203.
103. Lum Y, Ager JW. Stability of Residual Oxides in Oxide-Derived Copper Catalysts for Electrochemical CO₂ Reduction Investigated with O¹⁸ Labeling. *Angewandte Chemie-International Edition* 2018, 57(2): 551-554.
104. Pander JE, III, Ren D, Huang Y, Loo NWX, Hong SHL, Yeo BS. Understanding the Heterogeneous Electrocatalytic Reduction of Carbon Dioxide on Oxide-Derived Catalysts. *Chemelectrochem* 2018, 5(2): 219-237.
105. Lum Y, Ager JW. Evidence for Product-specific Active Sites on Oxide-derived Cu Catalysts for Electrochemical CO₂ reduction. *Nature Catalysis* 2019, 2(1): 86-93.
106. Hahn C, Hatsukade T, Kim Y-G, Vailionis A, Baricuatro JH, Higgins DC, *et al.* Engineering Cu Surfaces for the Electrocatalytic Conversion of CO₂: Controlling Selectivity toward Oxygenates and Hydrocarbons. *Proceedings of the National Academy of Sciences of the United States of America* 2017, 114(23): 5918-5923.
107. Roberts FS, Kuhl KP, Nilsson A. High Selectivity for Ethylene from Carbon Dioxide Reduction over Copper Nanocube Electrocatalysts. *Angewandte Chemie-International Edition* 2015, 54(17): 5179-5182.
108. Loiudice A, Lobaccaro P, Kamali EA, Thao T, Huang BH, Ager JW, *et al.* Tailoring Copper Nanocrystals towards C₂ Products in Electrochemical CO₂ Reduction. *Angewandte Chemie-International Edition* 2016, 55(19): 5789-5792.
109. Xiao H, Goddard WA, Cheng T, Liu Y. Cu metal Embedded in Oxidized Matrix Catalyst to Promote CO₂ Activation and CO Dimerization for Electrochemical Reduction of CO₂. *Proceedings of the National Academy of Sciences* 2017, 114(26): 6685-6688.
110. Gao D, Zegkinoglou I, Divins NJ, Scholten F, Sinev I, Grosse P, *et al.* Plasma-Activated Copper Nanocube Catalysts for Efficient Carbon Dioxide Electroreduction to Hydrocarbons and Alcohols. *Acs Nano* 2017, 11(5): 4825-4831.
111. Favaro M, Xiao H, Cheng T, Goddard WA, Yano J, Crumlin EJ. Subsurface Oxide Plays a Critical Role in CO₂ Activation by Cu (111) Surfaces to Form Chemisorbed CO₂, the First Step in Reduction of CO₂. *Proceedings of the National Academy of Sciences* 2017, 114(26): 6706-6711.
112. Cavalca F, Ferragut R, Aghion S, Eilert A, Diaz-Morales O, Liu C, *et al.* Nature and Distribution of Stable Subsurface Oxygen in Copper Electrodes During Electrochemical CO₂ Reduction. *The Journal of Physical Chemistry C* 2017, 121(45): 25003-25009.
113. Garza AJ, Bell AT, Head-Gordon M. Is Subsurface Oxygen Necessary for the Electrochemical Reduction of CO₂ on Copper? *The Journal of Physical Chemistry Letters* 2018, 9(3): 601-606.

-
114. Liu C, Hedström S, Stenlid JH, Pettersson LGM. Amorphous, Periodic Model of a Copper Electrocatalyst with Subsurface Oxygen for Enhanced CO Coverage and Dimerization. *The Journal of Physical Chemistry C* 2019, 123(8): 4961-4968.
 115. Rietveld H. A Profile Refinement Method for Nuclear and Magnetic Structures. *Journal of applied Crystallography* 1969, 2(2): 65-71.
 116. Fassel VA, Kniseley RN. Inductively Coupled Plasma. *Optical Emission Spectroscopy. Analytical Chemistry* 1974, 46(13): 1110A-1120A.
 117. Risch M, Klingan K, Heidkamp J, Ehrenberg D, Chernev P, Zaharieva I, *et al.* Nickel-oxido Structure of a Water-oxidizing Catalyst Film. *Chemical Communications* 2011, 47(43): 11912-11914.
 118. Risch M, Ringleb F, Kohlhoff M, Bogdanoff P, Chernev P, Zaharieva I, *et al.* Water Oxidation By Amorphous Cobalt-based Oxides: *in situ* Tracking of Redox Transitions and Mode of Catalysis. *Energy & Environmental Science* 2015, 8(2): 661-674.
 119. Hansen TW, DeLaRiva AT, Challa SR, Datye AK. Sintering of Catalytic Nanoparticles: Particle Migration or Ostwald Ripening? *Acc Chem Res* 2013, 46(8): 1720-1730.
 120. Schreier M, Yoon Y, Jackson MN, Surendranath Y. Competition Between H and CO for Active Sites Governs Copper-mediated Electrosynthesis of Hydrocarbon Fuels. *Angewandte Chemie International Edition* 2018, 57(32): 10221-10225.
 121. Huang J, Mensi M, Oveisi E, Mantella V, Buonsanti R. Structural Sensitivities in Bimetallic Catalysts for Electrochemical CO₂ Reduction Revealed by Ag-Cu Nanodimers. *J Am Chem Soc* 2019, 141(6): 2490-2499.
 122. Lum Y, Ager JW. Sequential Catalysis Controls Selectivity in Electrochemical CO₂ Reduction on Cu. *Energy & Environmental Science* 2018, 11(10): 2935-2944.
 123. Jovanove Z, Araújo J, Li S, Strasser P. Catalyst Preoxidation and EDTA Electrolyte Additive Remedy Activity and Selectivity Declines During Electrochemical CO₂ Reduction. *Journal of Physical Chemistry C* 2019, 123(4): 2165-2174.
 124. Feng X, Jiang K, Fan S, Kanan MW. A Direct Grain-Boundary-Activity Correlation for CO Electroreduction on Cu Nanoparticles. *ACS Central Science* 2016, 2(3): 169-174.
 125. Liu X, Xiao J, Peng H, Hong X, Chan K, Nørskov JK. Understanding Trends in Electrochemical Carbon Dioxide Reduction Rates. *Nature Communications* 2017, 8: 15438
 126. Wang X, Varela AS, Bergmann A, Kuehl S, Strasser P. Catalyst Particle Density Controls Hydrocarbon Product Selectivity in CO₂ Electroreduction on CuO_x. *ChemSusChem*, 2017, 10: 4642-4649.
 127. Wang X, Araújo J, Ju W, Bagger A, Schmies H, Kuehl S, *et al.* Mechanistic reaction pathways of enhanced ethylene yields during electroreduction of CO₂-CO co-feeds on Cu and Cu-tandem electrocatalysts. *Nature Nanotechnology*, 2019, 14: 1063-1070.

Appendix

A1. Supplementary Information to Chapter 4

Catalyst particle density controls hydrocarbon product selectivity in CO₂ electroreduction on CuO_x

Reproduced with permission from [ChemSusChem, 2017, 10, 4642-4649](#). Copyright of The John Wiley and Sons (2017).¹²⁶

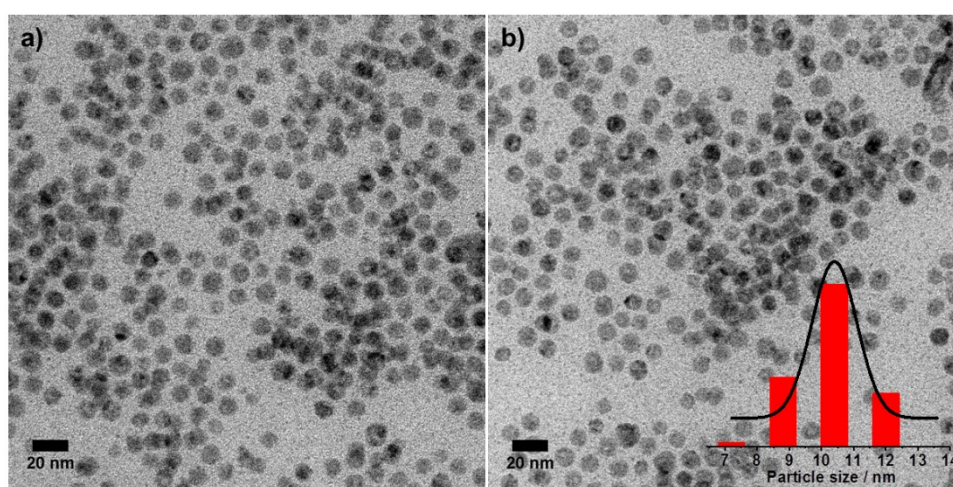


Figure A1.1 a) b) Representative TEM images of CuO_x nanoparticles after 7 days in hexane. The inset shows the size distribution of CuO_x nanoparticles.

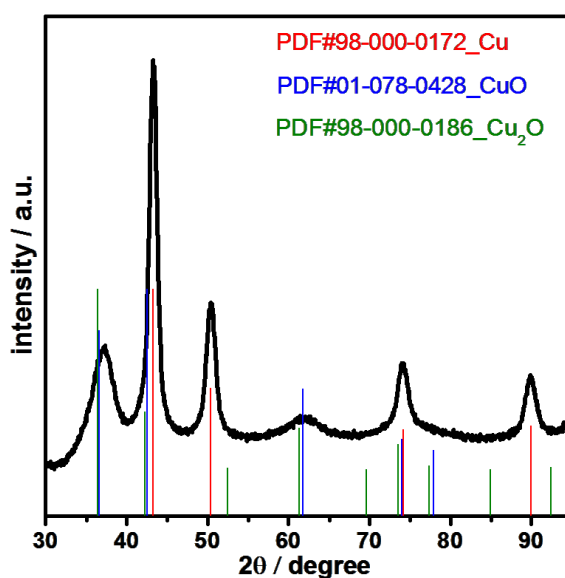


Figure A1.2 a) Diffraction pattern of as-prepared CuO_x NPs. Also indicated are diffraction patterns of metallic Cu (red, PDF#98-000-0172), CuO (blue, PDF#01-078-0428), and Cu₂O (green, PDF#98-000-0186).

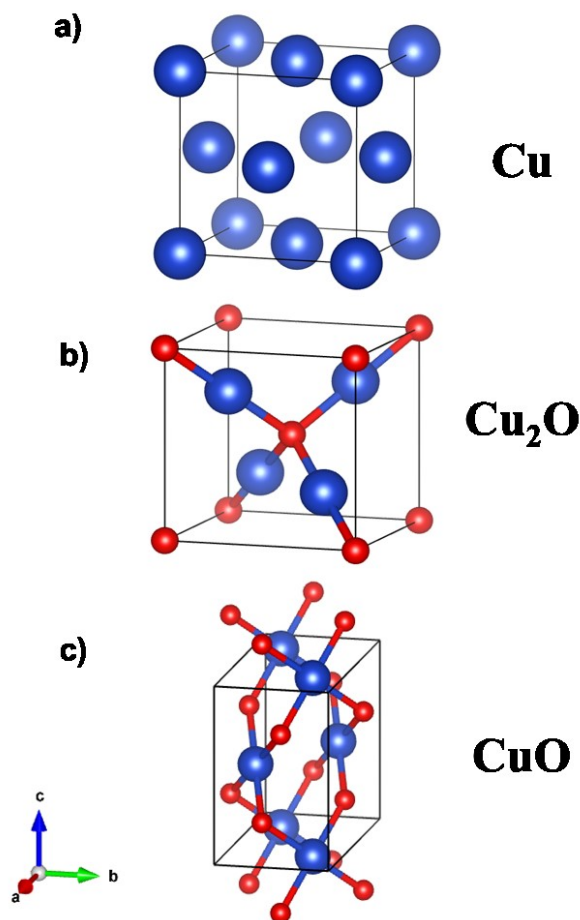


Figure A1.3 The crystal structures of a) metallic Cu, b) cubic-Cu₂O (cuprite), c) monoclinic-CuO (Tenorite). Color legend: blue spheres, Cu; red sphere, O.

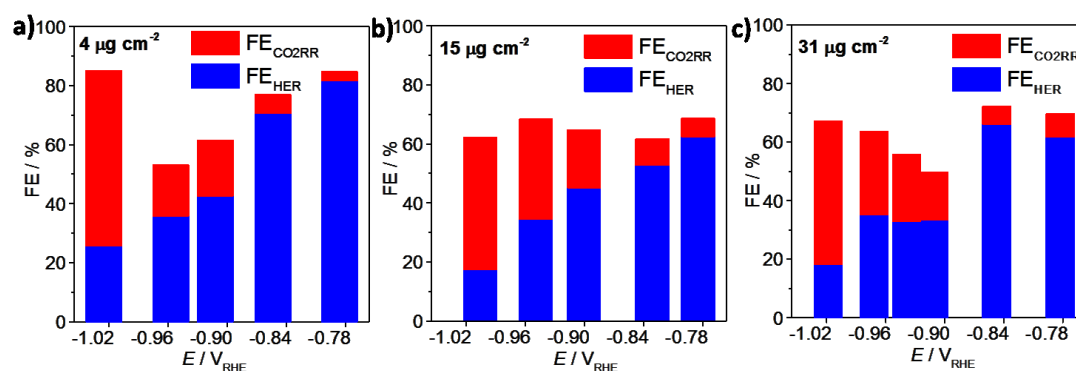


Figure A1.4 The total Faradaic efficiencies of gaseous products as a function of areal density at various applied overpotentials. Faradaic efficiencies of CO₂RR and HER over a) 4 μg cm⁻², b) 15 μg cm⁻², c) 31 μg cm⁻².

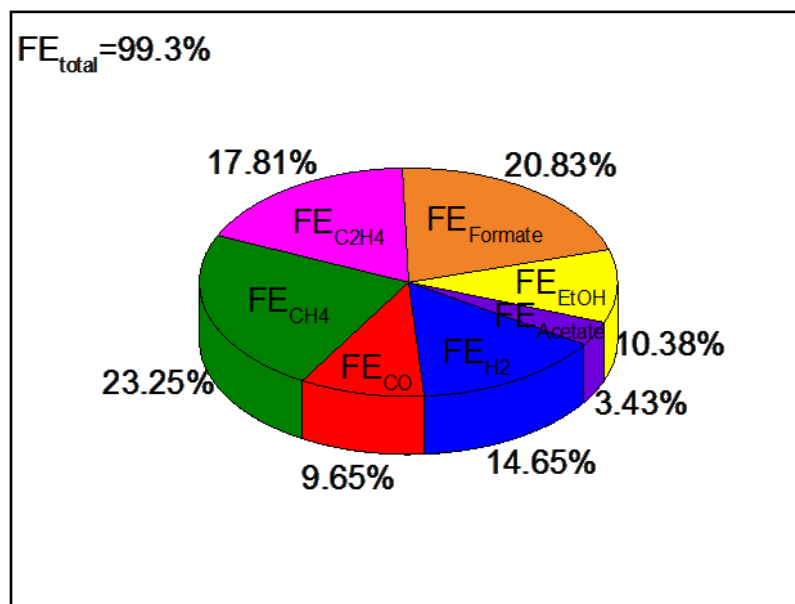


Figure A1.5 The Faradaic efficiencies for all detected products on CuO_x NPs after 400 min with the areal particle density of $31 \mu g cm^{-2}$ at $-1.0V_{RHE}$.

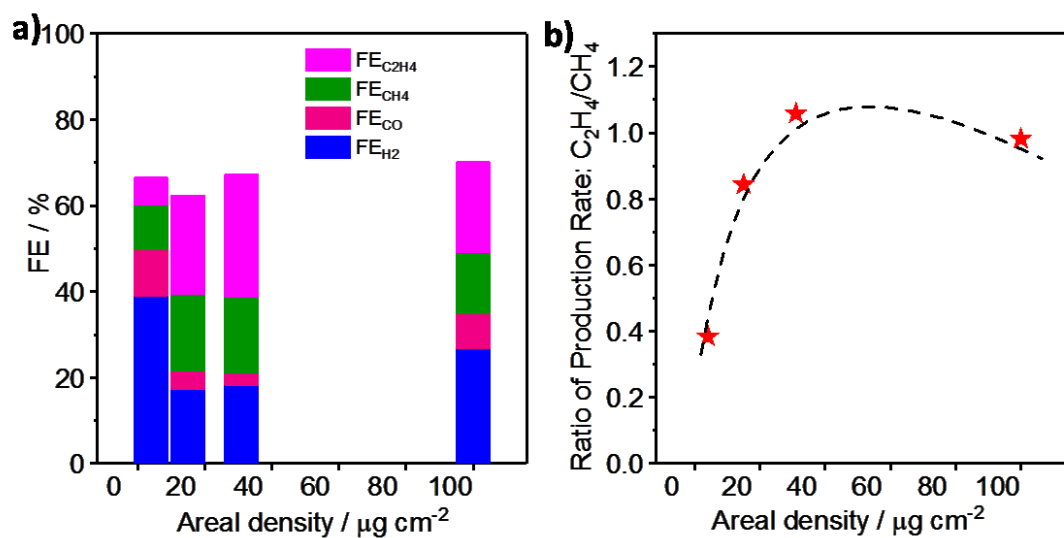


Figure A1.6 a) Total Faradaic efficiency for gaseous products as a function of areal particle density. b) Trends in C_2H_4/CH_4 production ratio at varying catalyst areal densities at $-1.01 V_{RHE}$ applied electrode potential. Potentials are IR corrected.

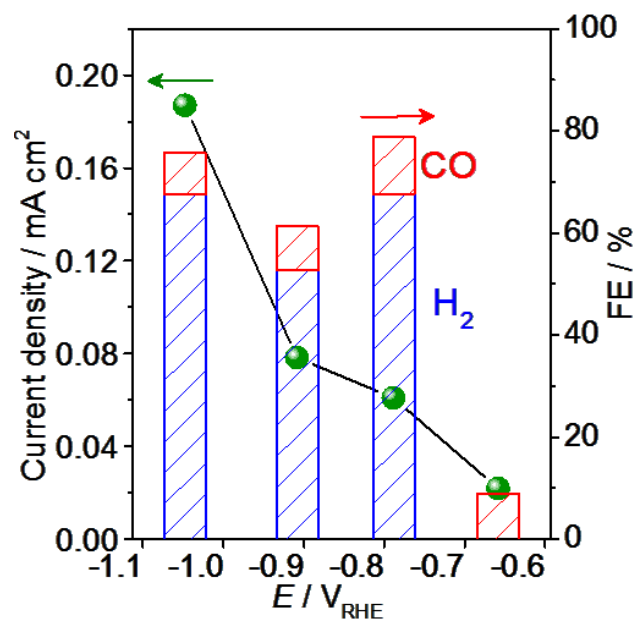


Figure A1.7 Electrochemical CO₂ reduction activity (left axis of ordinates) and selectivity (right axis of ordinates) of glassy carbon as blank at various overpotentials. The amount of H₂ at -0.66 V_{RHE} is not detectable (under TCD detecting limitation).

A2. Supplementary Information to Chapter 5

Mechanistic reaction pathways of enhanced ethylene yields during electroreduction of CO₂-CO co-feeds on Cu and Cu-tandem electrocatalysts

Reproduced in part with permission from [Nat. Nanotechnol., 2019, 14, 1063-1070](#). Copyright of Springer Nature.¹²⁷

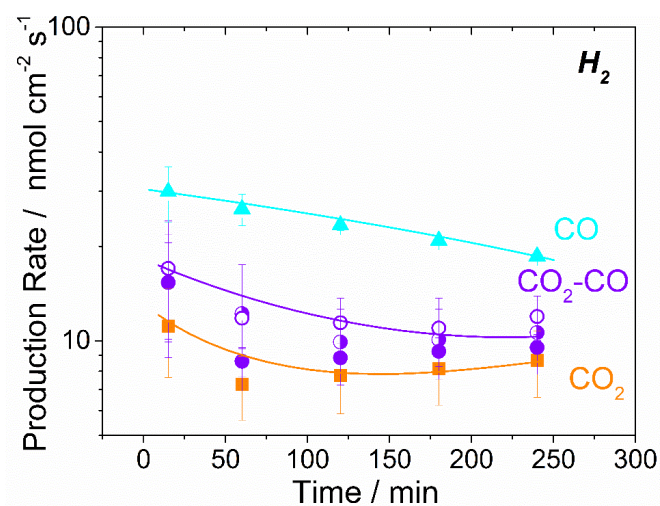


Figure A2.1 Time-dependent absolute product formation rates on H₂. Orange: CO₂RR in CO₂ saturated 0.1 M KHCO₃ (pH=6.8); cyan: CORR in 0.1 M K₂HPO₄/KH₂PO₄ (pH=6.9); Violet: co-feeds (CO₂/CO) reduction reductions in CO₂ saturated 0.1 M KHCO₃. Catalyst loading: 100 ug/cm².

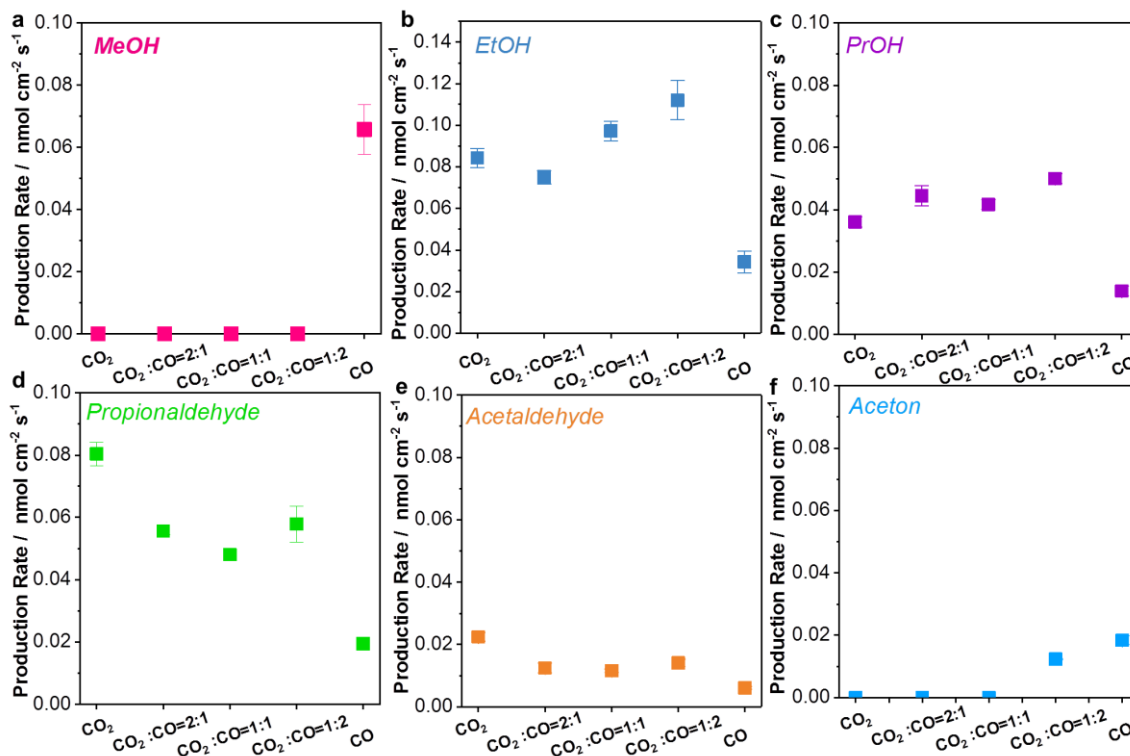


Figure A2.2 Liquid products analysis after 4-hour measurements in various feeds conditions. Absolute product formation rates of detected liquid products on CuO_x NPs with various CO_2/CO ratios.

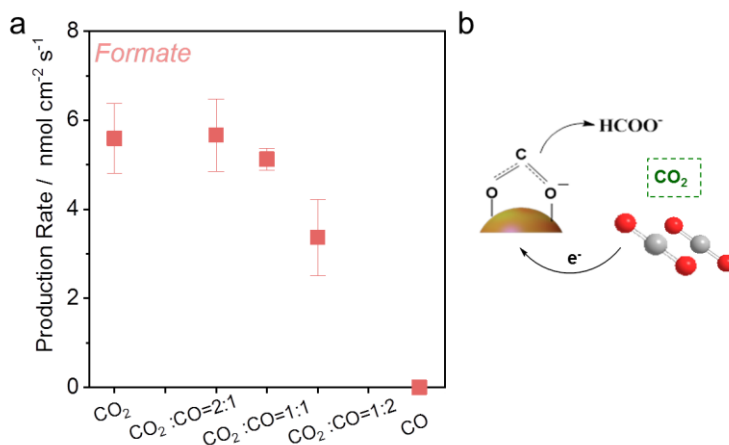


Figure A2.3 Formate analysis after 4-hour measurements in various feeds conditions. a) Absolute product formation rate of formate on CuO_x NPs with various CO_2/CO ratios. b) The pathway from CO_2 to formate. It shows that the formate only forms in CO_2 -involving feeds.

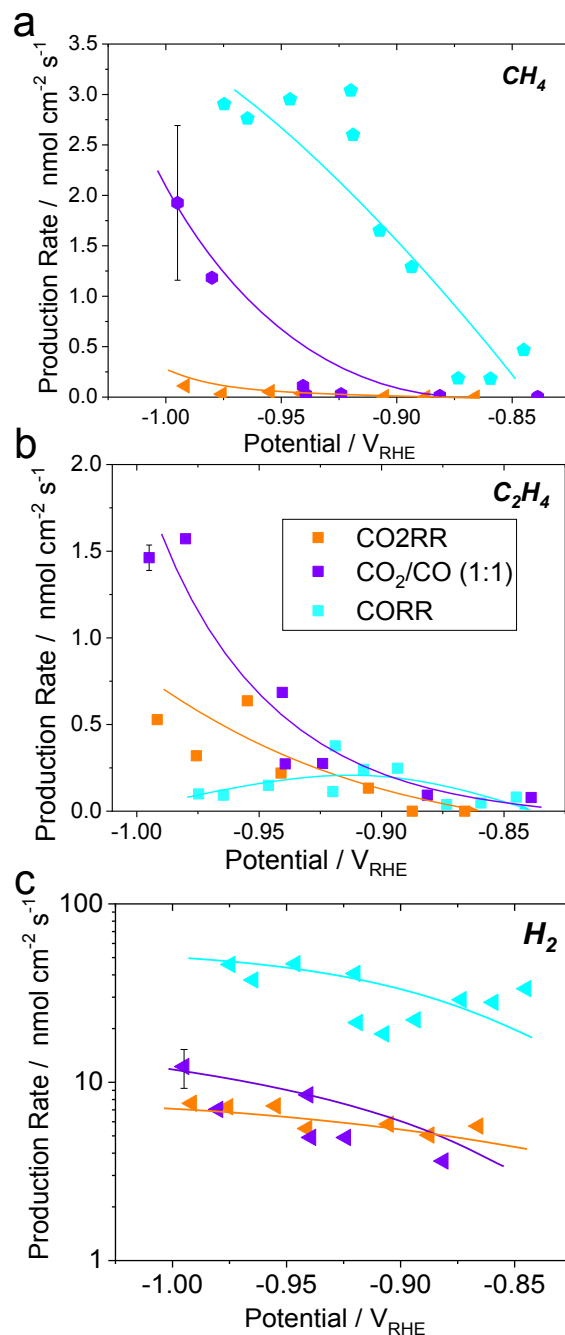


Figure A2.4 The potential-dependent tests of CORR, CO₂RR and co-feed reduction (CO₂/CO 1:1). Absolute product formation rates of a) CH_4 , b) C_2H_4 and c) H_2 on CuO_x nanoparticles.

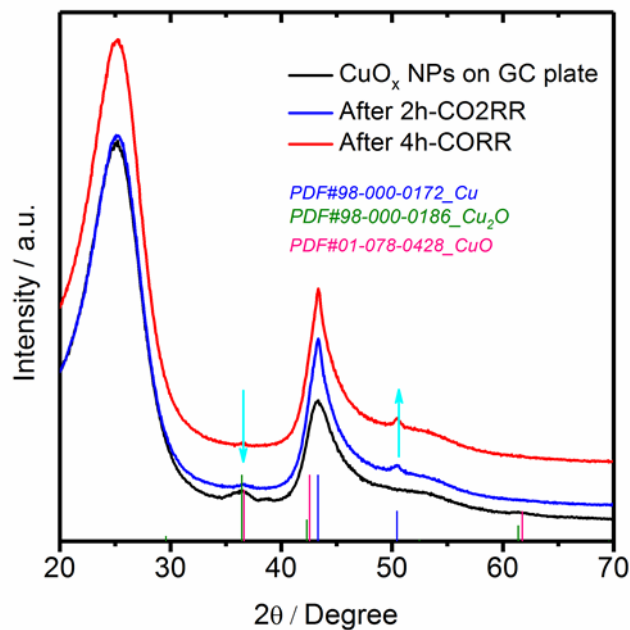


Figure A2.5 XRD profiles of as-prepared working electrodes tested before and after electrochemical reductions. Grazing incidence X-ray Diffraction (GI-XRD) analysis of thin film catalysts coated on glassy carbon as working electrodes. The bottom lines show pdf reference patterns of metallic copper (Cu, blue), pdf # 98-000-0172; cuprite (Cu₂O, green), pdf # 98-000-0186, and of tenorite, (CuO, pink), pdf # 01-078-0428.

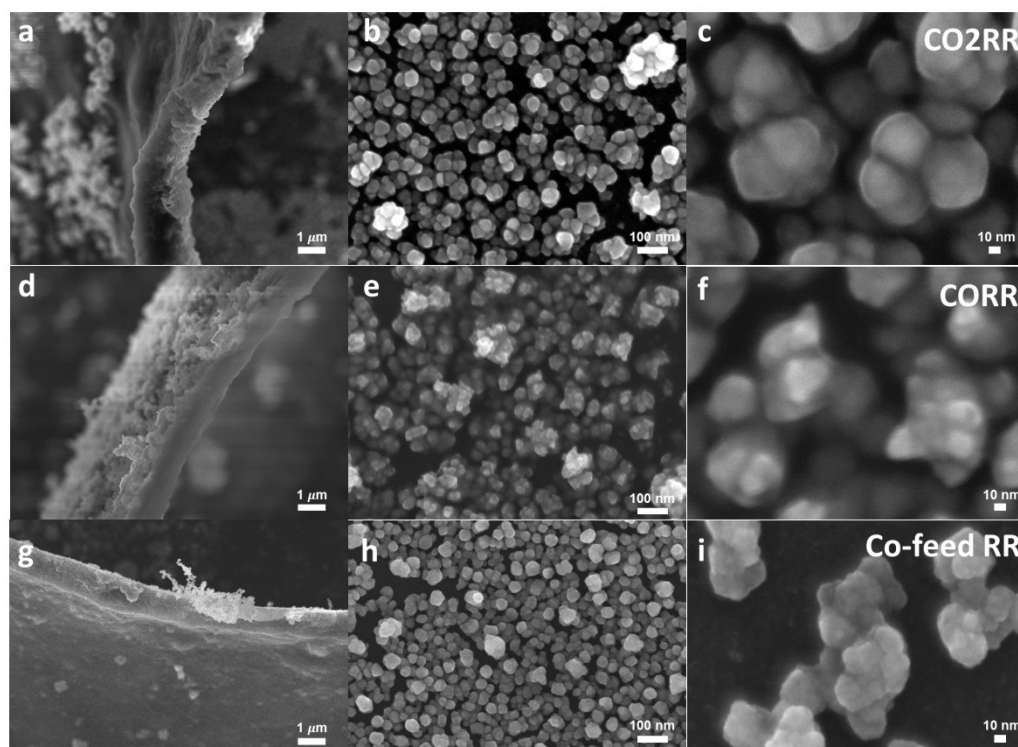


Figure A2.6 SEM images of as-prepared working electrodes after electrochemical reductions. Morphology evolution of CuO_x NPs during a-c) CO_2RR in CO_2 saturated 0.1 M KHCO_3 (pH=6.8); d-e) CORR in 0.1 M $\text{K}_2\text{HPO}_4/\text{KH}_2\text{PO}_4$ (pH=6.9); g-i) co-feed reduction (CO_2 : CO 1:1) in CO_2 saturated 0.1 M KHCO_3 (pH=6.8).

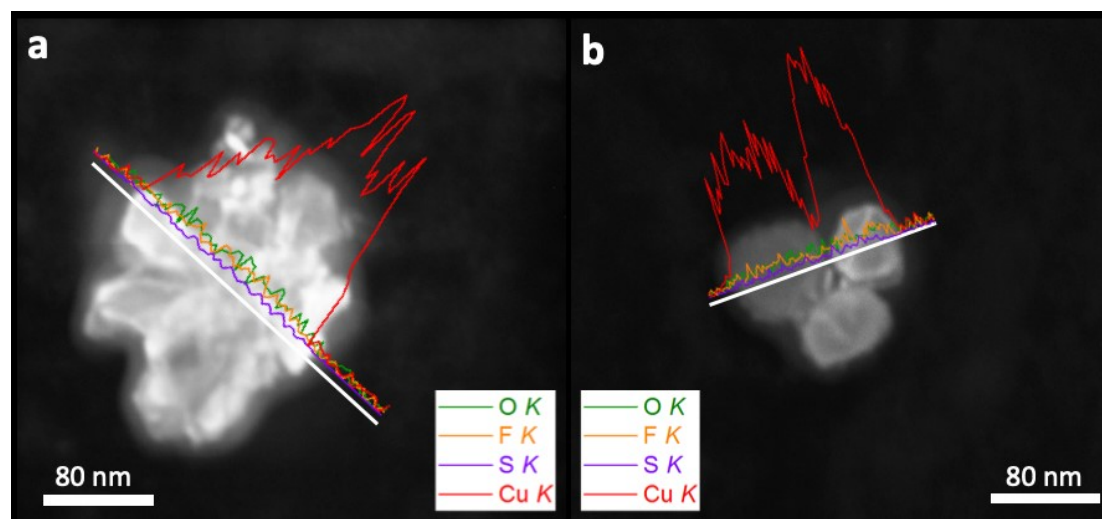


Figure A2.7 High angle annular dark field (HADDF) images and EDX (Energy dispersive X-ray spectroscopy) line scan of the CuO_x NPs after co-feed (1:1) reduction. EDX line analysis of the CuO_x NPs was carried out by detection of X-ray band derived from O K, F K, S K, and Cu K with two distinct locations.

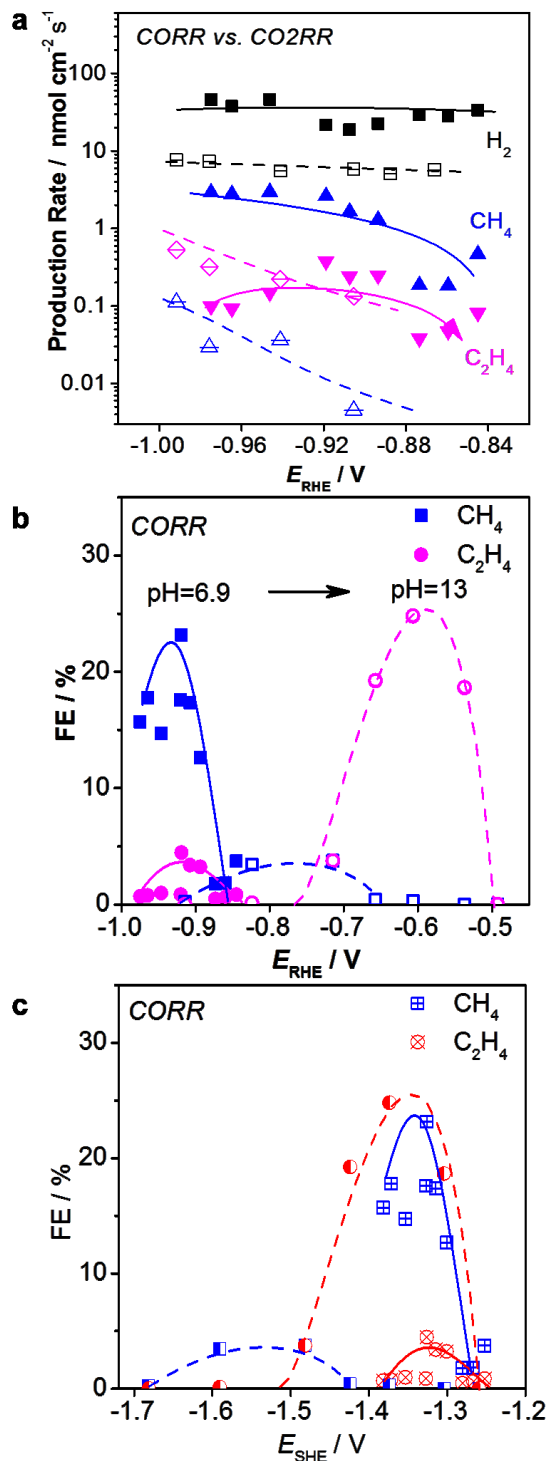


Figure A2.8 Investigation of pure feed reductions of CORR and CO2RR. a) Absolute product formation rates of major gaseous products (black: H_2 ; blue: CH_4 ; pink: C_2H_4) as a function of applied electrode potentials during CORR (solid plots) in 0.1 M $\text{K}_2\text{HPO}_4/\text{KH}_2\text{PO}_4$ ($\text{pH}=6.9$) and CO2RR (hollow plots) in CO_2 -saturated 0.1M KHCO_3 . b, c) Faradaic efficiencies of major gaseous products (blue: CH_4 ; red: C_2H_4) as a function of applied electrode potentials during CORR in 0.1 M $\text{K}_2\text{HPO}_4/\text{KH}_2\text{PO}_4$ ($\text{pH}=6.9$) and 0.1 M KOH ($\text{pH}=13$). Potentials are IR corrected.

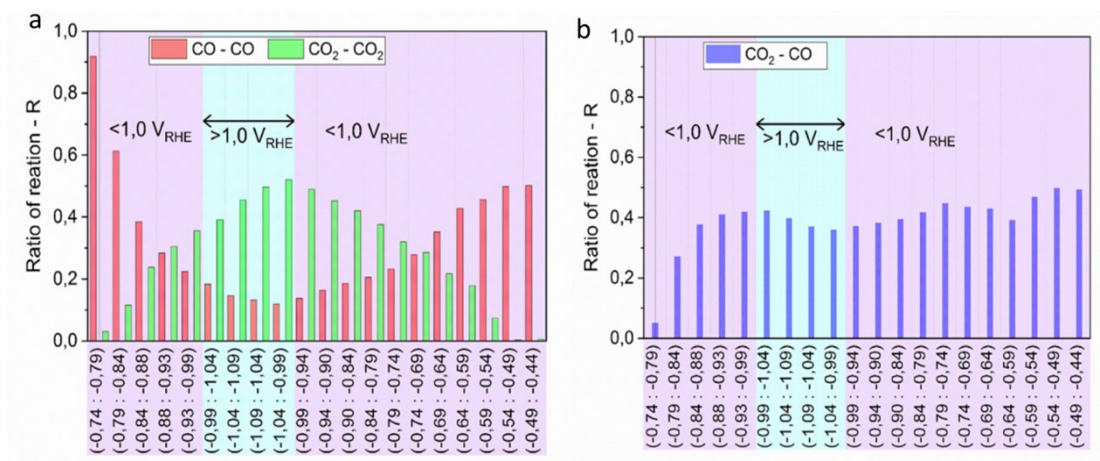


Figure A2.9 The ratios of reaction between the three mechanisms. The ratio of reaction between the three mechanisms on a) CO-CO, CO₂-CO₂, and b) CO₂-CO, with respective potential range for integration at 0.05 V from cathodic to anodic sweep of potentials.

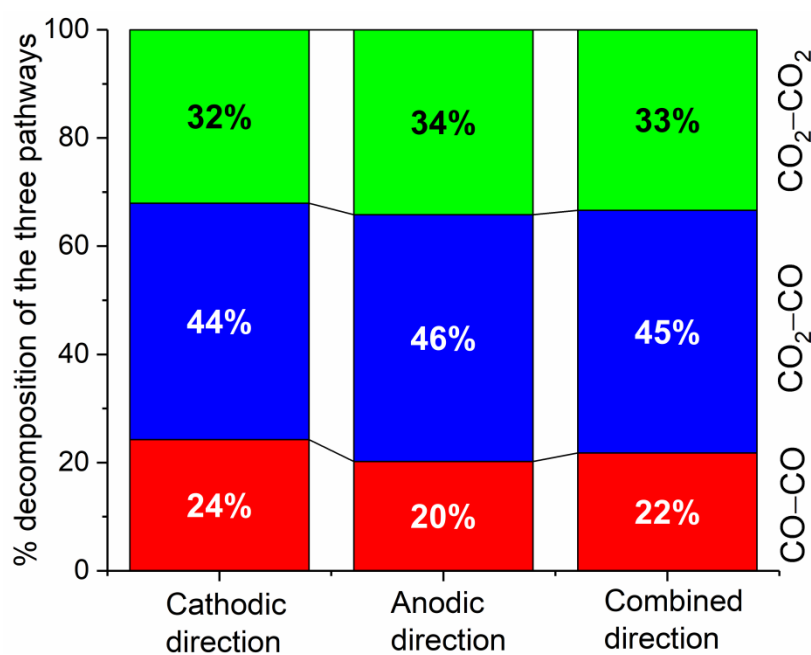


Figure A2.10 Decomposition of the three pathways calculated by the co-feed system of a mixture of carbon isotopes. The charge under deconvoluted curves in each correspondent pathway CO-CO (red area), CO₂-CO (blue area) and CO₂-CO₂ (green area) in fragment M-H⁺. Analysis were carried out during cathodic, and anodic direction and the sum with combination direction (total charge)

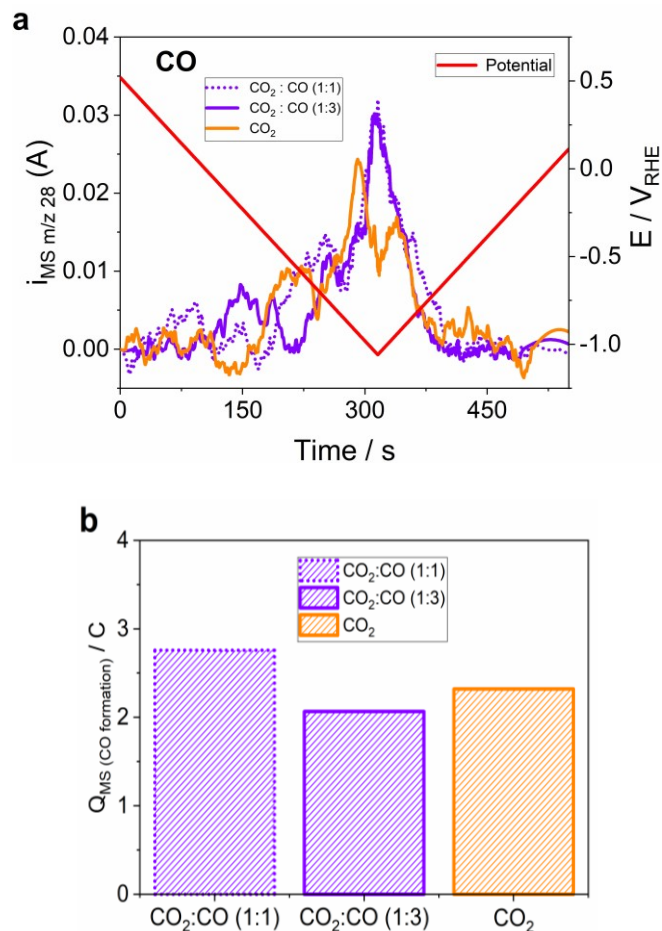


Figure A2.11 Differential electrochemical mass spectrometry data obtained on 0.785 cm^2 large glassy carbon electrode drop-coated with CuO_x NPs catalysts and using pure CO, pure CO_2 , and CO_2 -CO co-feed. The graph above presents the ion mass current over time with products deconvoluted CO ($m/z\ 28$) measured in pure CO, pure CO_2 and CO_2 -CO co-feed system in a mixed ratio of 1:1 or in the diluted gas ratio (1:3). The bar graph in the figure illustrates the ionic mass charge for CO evolution (taken by $m/z\ 28$) for each feeds measured.

To deconvolute of CO signal from mass fragmentation signal of CO_2 (CO^+ $m/z\ 28$), we used the relation of molecular mass signal $m/z\ 44$ and fragment signal $m/z\ 28$. Even though the signal intensity of molecular mass ethylene ($m/z\ 28$) is relatively small ($\sim 3\%$) compared to CO signal, it was subtracted from the CO molecule mass signal.

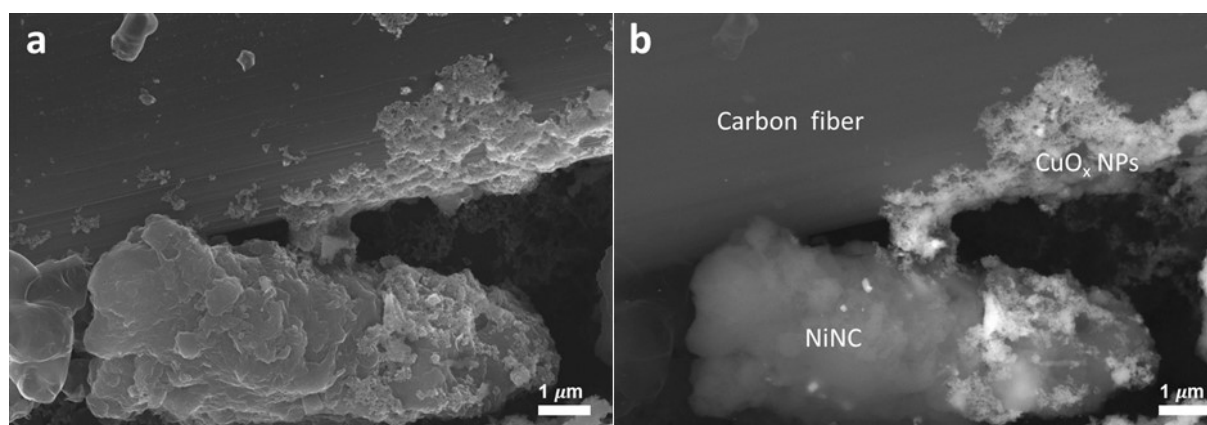


Figure A2.12 SEM images of as-prepared the bifunctional hybrid catalyst. SEM images of CuO_x NPs ($50 \mu\text{g cm}^{-2}$)-NiNC (1:4) tandem catalyst with carbon paper as working electrode (carbon fiber), a) SEI mode; b) COMPO mode.

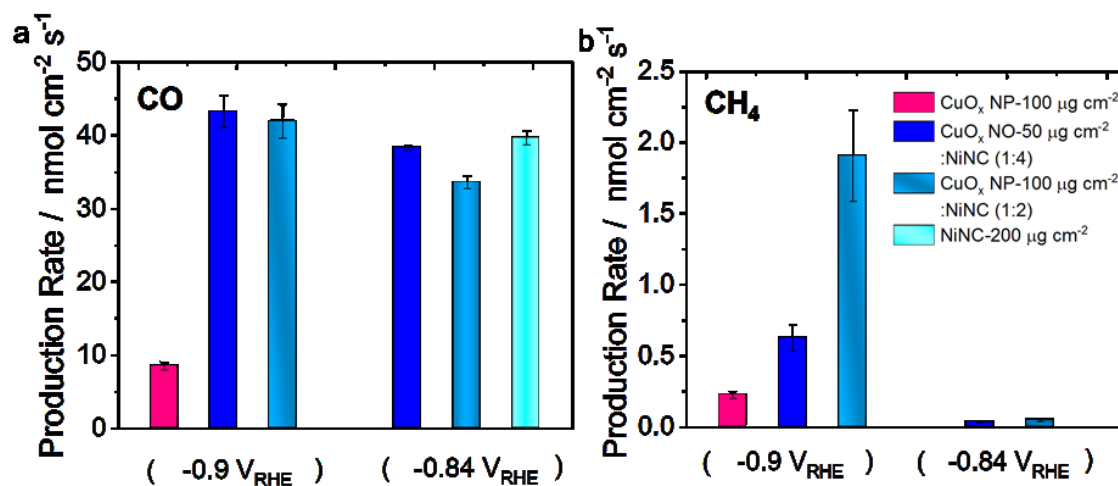


Figure A2.13 Catalytic performance of the tandem CuO_x -NiNC catalysts detected by on-line GC in H-cell. Absolute product formation rates on a) CO and b) CH_4 with different catalyst loading variation at $-0.84 V_{\text{RHE}}$ and $-0.9 V_{\text{RHE}}$. No detectable CH_4 formation on pure NiNC and pure CuO_x NPs with areal loading of $100 \mu\text{g cm}^{-2}$ at $-0.84 V_{\text{RHE}}$.

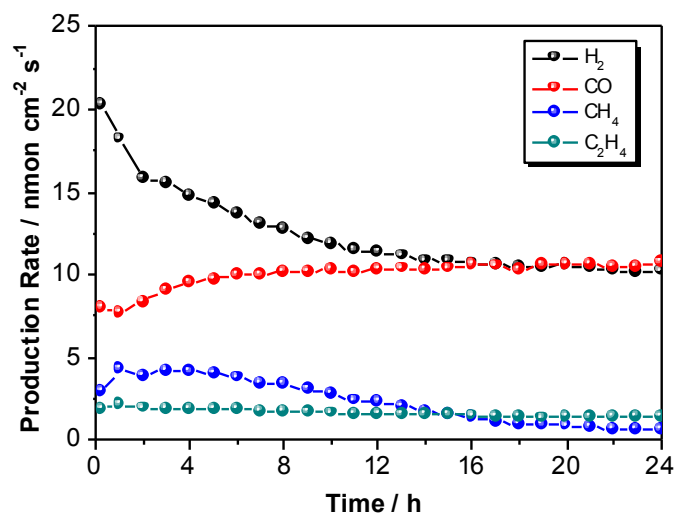


Figure A2.14 The long stability test of tandem CuO_x-Ag (1:3) catalyst at a constant electrode potential of -1.0 V_{RHE} in CO₂-saturated 0.1 M KHCO₃.

Table A2.1 Liquid products of tandem CuO_x-NiNC catalysts during CO₂RR after 90 min at fixed overpotential.

Tandem Catalyst	Acetaldehyde (nmol cm ⁻² s ⁻¹)	Propionaldehyde (nmol cm ⁻² s ⁻¹)	EtOH (nmol cm ⁻² s ⁻¹)	PrOH (nmol cm ⁻² s ⁻¹)	AllylOH (nmol cm ⁻² s ⁻¹)
CuO _x NP-100 ug cm ⁻² : NiNC (1:2) @ -0.9 V _{RHE}	1.96E-4 ± 2.6E-5	1.16E-4 ± 9.4E-6	0.00111 ± 2.8E-5	5.01E-4 ± 3.1E-5	2.12E-4 ± 3.9E-6

A3. Supplementary Information to Chapter 6

Sheet-like Copper Oxides with Stable and Selective Ethylene Production for Direct CO₂ Electroreduction

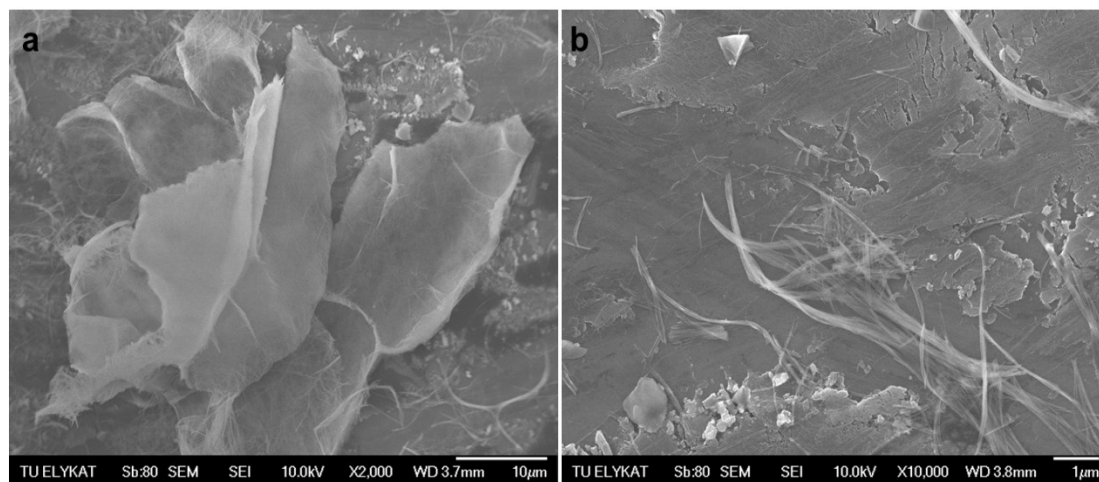


Figure A3.1 SEM images of Cu(OH)₂ intermediate formed during synthesis process.

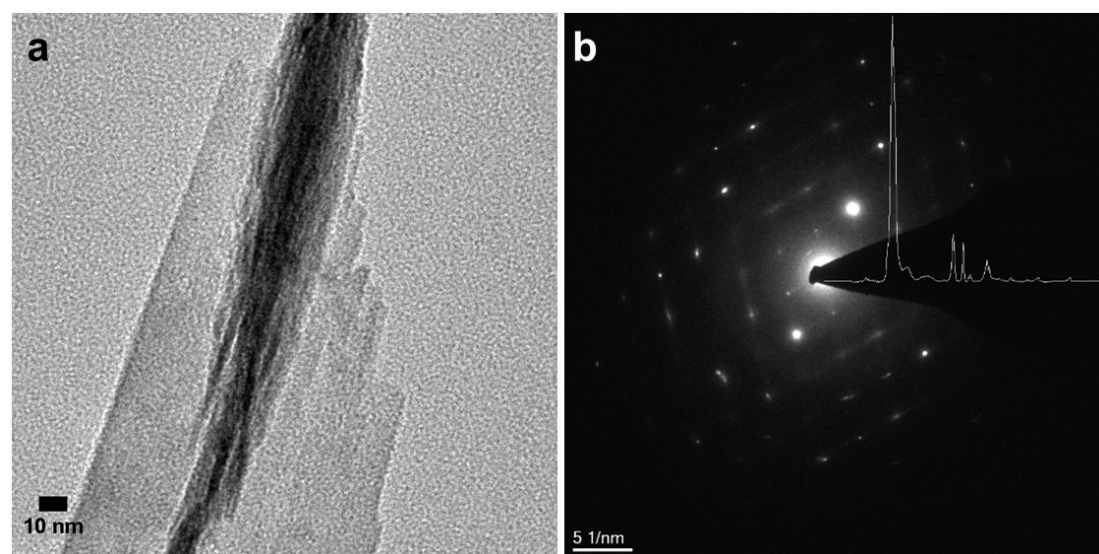


Figure A3.2 a) Cross-section TEM images of as-prepared CuO_x NS and b) corresponding intensity of SAED intensity.

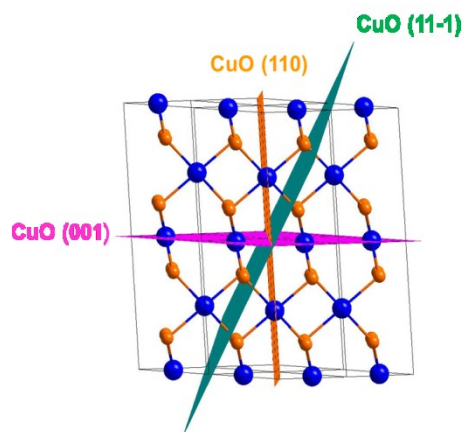


Figure A3.3 Crystal structure of monoclinic CuO with indexing plane.

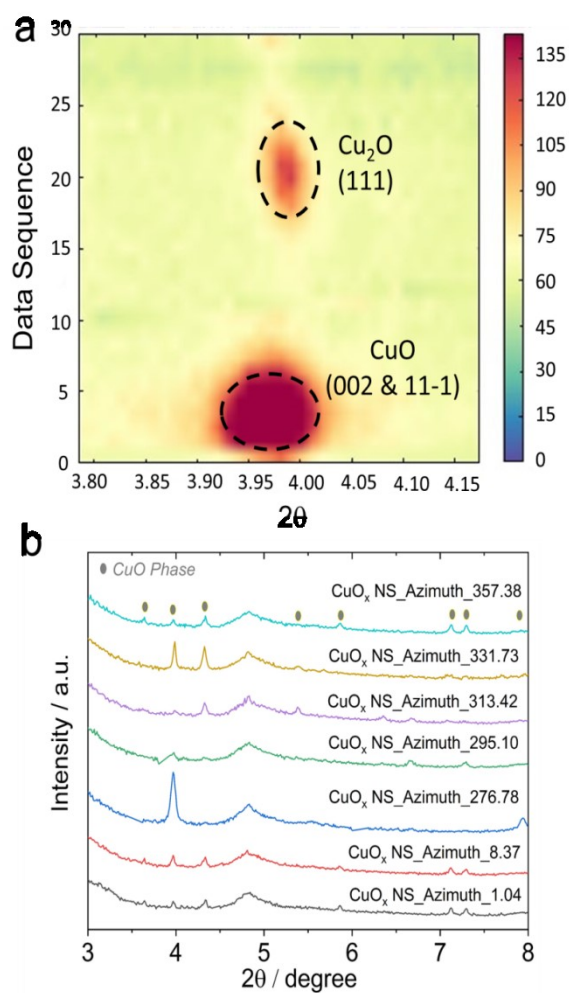


Figure A3.4 a) Partial contour plot of CuO_x NS. b) Azimuthally integrated line profiles of as-prepared CuO_x NS.

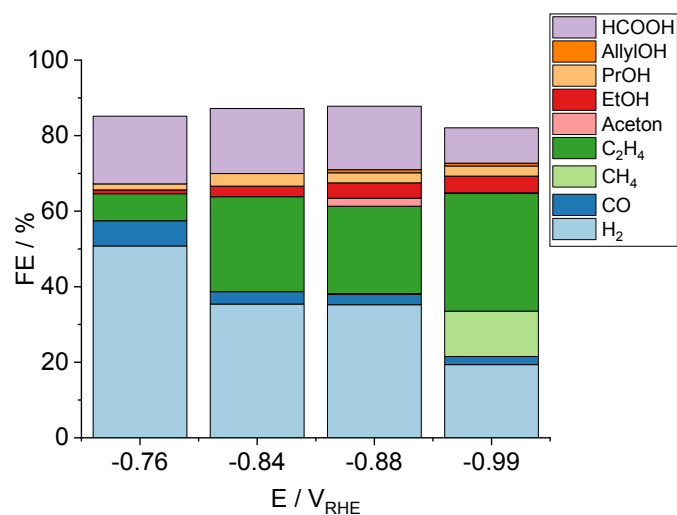


Figure A3.5 Faradaic efficiencies of main products distribution after CO₂RR in H-cell design.

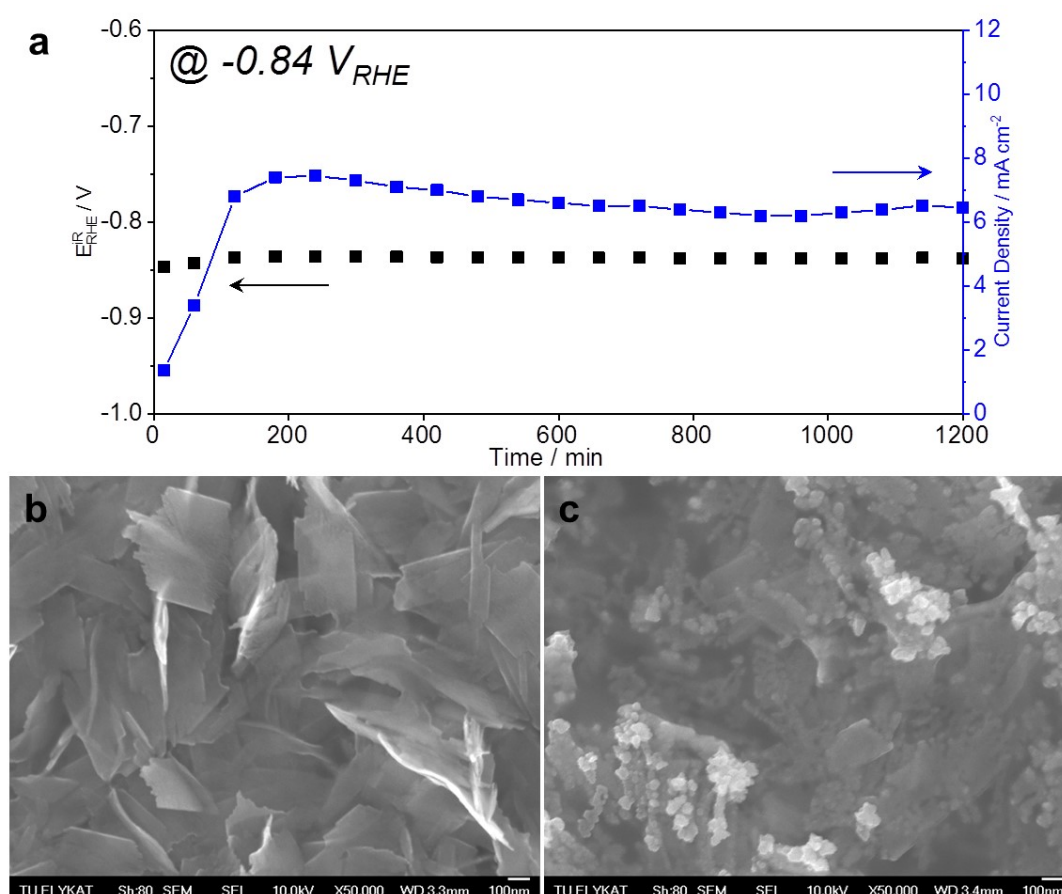


Figure A3.6 a) Chronoamperometric performance stability of the CO₂ reduction reaction on CuO_x NS in CO₂-saturated 0.1M KHCO₃ at $-0.84 V_{RHE}$. SEM image of as-prepared CuO_x catalyst on GC electrode ($100 \mu g cm^{-2}$) before b) and c) after 20-hour electrolysis.

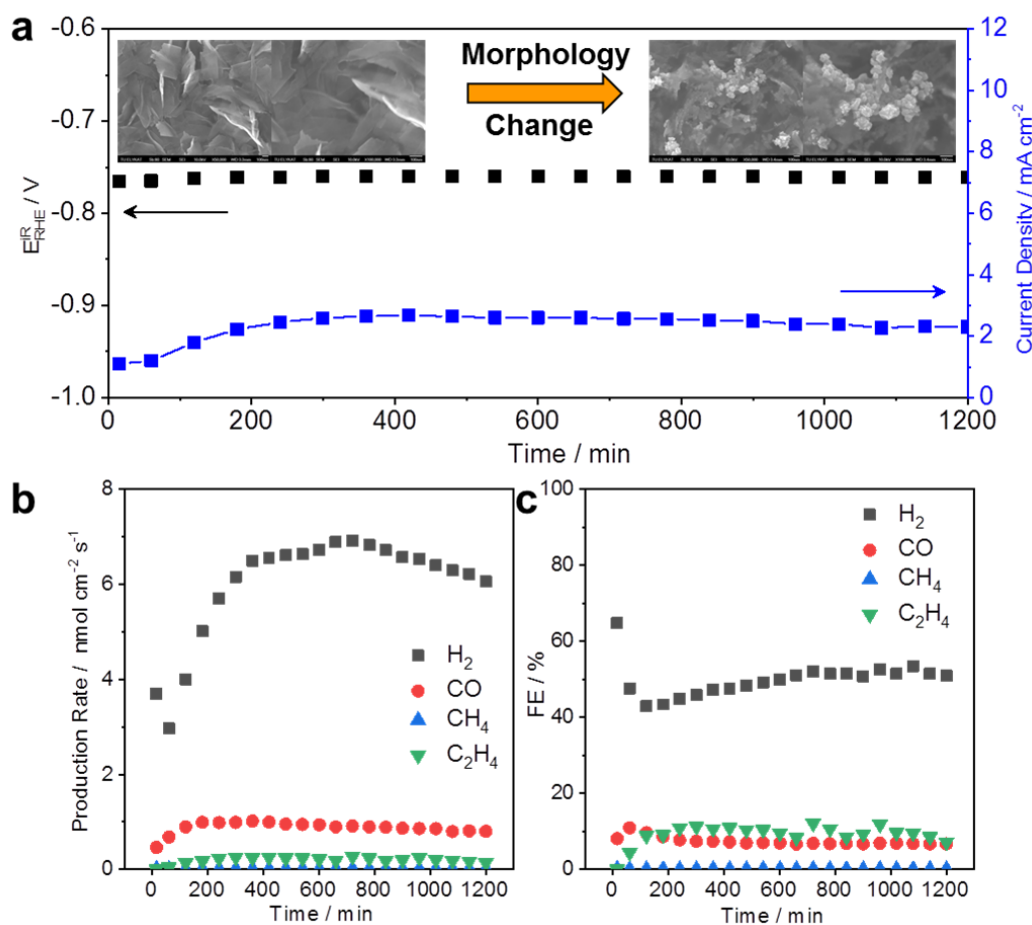


Figure A3.7 a) Chronoamperometric performance stability of the CO_2 reduction reaction on CuO_x NS in CO_2 -saturated 0.1M KHCO_3 at $-0.76 V_{\text{RHE}}$. Insert: SEM image of as-prepared CuO_x catalyst on GC electrode ($100 \mu\text{g cm}^{-2}$) before and after 20-h electrolysis. Production rates b) and Faradaic efficiencies c) of main gaseous products over 1200 min.

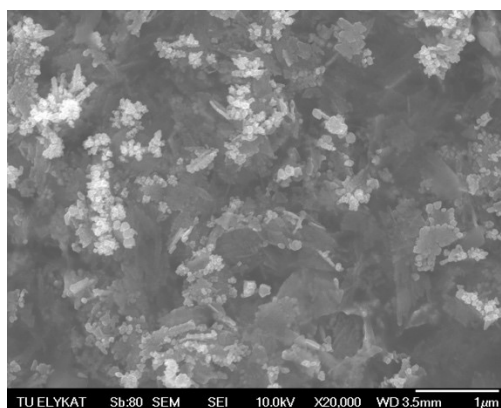


Figure A3.8 SEM image of 1-h Chronoamperometric performance of the CO_2 reduction reaction on CuO_x NS in CO_2 -saturated 0.1M KHCO_3 at $-0.84 V_{\text{RHE}}$.

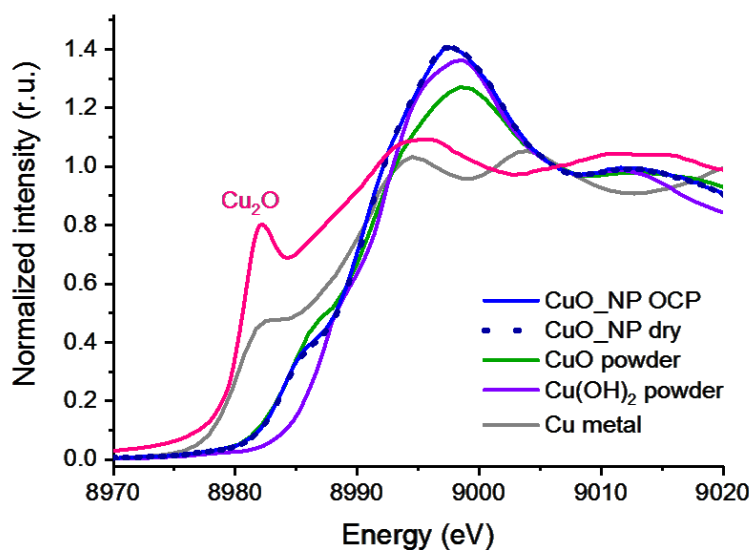


Figure A3.9 Comparison of XANES at the Cu K-edge of references powders CuO, Cu(OH)₂ and the CuO_x NS film in the dry state, and at OCP in 0.1 M KHCO₃ at pH 6.8.

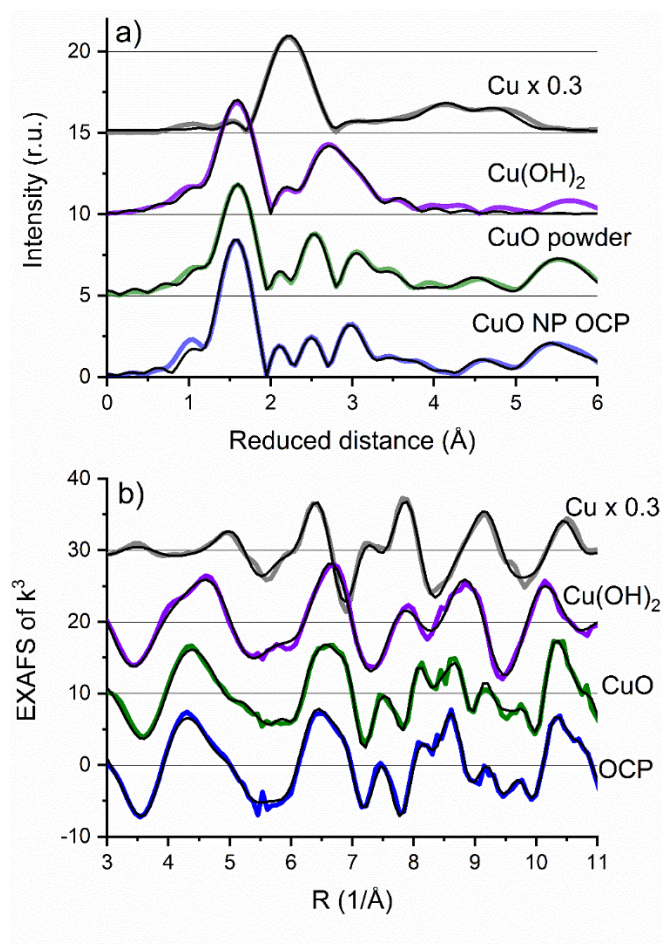


Figure A3.10 a) FT of k^3 weighted EXAFS a) and b) EXAFS at the Cu K-edge of Cu metal foil, Cu(OH)₂ powder, CuO powder, and the CuO_x NS film at OCP in 0.1 M KHCO₃ at pH

6.8. Colored lines represent the experimental data and black lines in the simulations. The distance on the x-axis in a) is reduced by 0.35 \AA relative to the real distance.

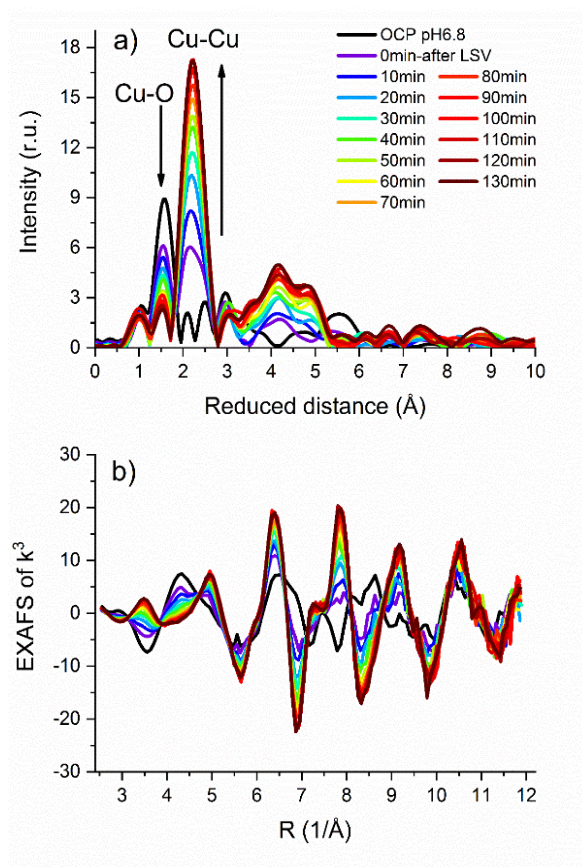


Figure A3.11 a) FT of k^3 weighted EXAFS at the Cu K-edge of the CuO_x NS film at OCP in 0.1 M KHCO_3 at pH 6.8 and during 130 min CO_2RR at $-0.84 V_{\text{RHE}}$. The distance on the x-axis is reduced by 0.35 \AA relative to the real distance. b) EXAFS (k^3 weighted) at the Cu K-edge of the CuO_x NS film at OCP in 0.1 M KHCO_3 at pH 6.8 and during 130 min CO_2RR at $-0.84 V_{\text{RHE}}$.

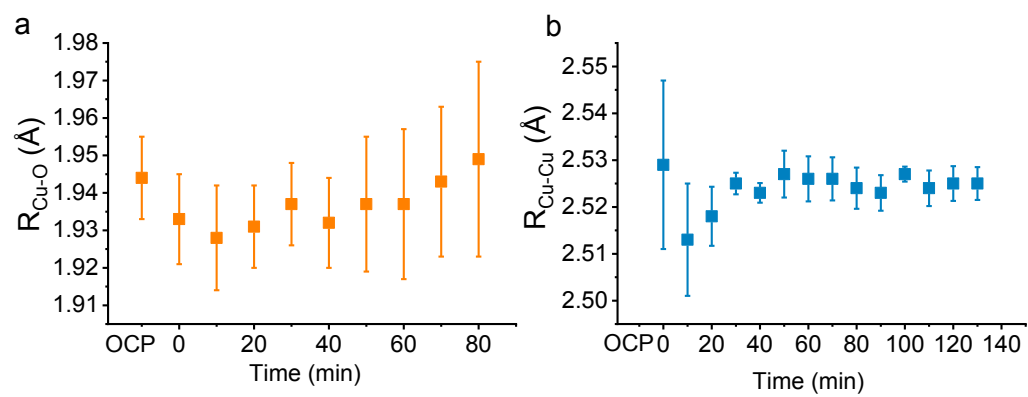


Figure A3.12 EXAFS distances of the first Cu-O coordination sphere and the first intermetallic Cu-Cu shell.

Table A3.1 Cu *K*-edge simulation parameters of the FT-EXAFS oscillations of as-prepared CuO_x NS film. Data range $k=3-11 \text{ \AA}^{-1}$, Amplitude reduction factor $S_0^2=0.8$.

CuO NS film as-prepared					
	Shell	R /\AA	N	σ	R_f
OCP	Cu-O	1.94 ± 0.01	4.2 ± 0.13	0.0431*	11.39
	Cu-Cu	2.69 ± 0.02	2.2 ± 0.22	0.0415*	
	Cu-Cu	2.88 ± 0.02	4.1 ± 0.14	0.0629*	
	Cu-Cu	3.03 ± 0.01	4.1 ± 0.32	0.0536*	
	Cu-Cu	3.14 ± 0.01	2.3 ± 0.32	0.0318*	
	Cu-Cu	3.30 ± 0.01	1.8 ± 0.13	0.0997*	
	0 min	Cu-O	1.93 ± 0.01	2.82 ± 0.21	
Cu-Cu		2.53 ± 0.02	3.9 ± 1	0.0853*	
Cu-Cu		2.74 ± 0.03	5.37 ± 1.9	0.0629*	
Cu-Cu		2.93 ± 0.03	7.17 ± 2.1	0.0536*	
Cu-Cu		3.11 ± 0.03	3.46 ± 0.8	0.0318*	
Cu-Cu		4.43 ± 0.02	4.51 ± 1	0.0885*	
10 min		Cu-O	1.93 ± 0.01	2.25 ± 0.22	0.0431*
	Cu-Cu	2.51 ± 0.01	4.93 ± 0.32	0.0853*	
	Cu-Cu	3.63 ± 0.11	1.84 ± 2.4	0.0906*	
	Cu-Cu	4.41 ± 0.03	6.4 ± 1.3	0.0885*	
	Cu-Cu	4.92 ± 0.02	2.81 ± 0.66	0.0344*	
	Cu-Cu	3.48 ± 0.07	4.12 ± 2.4	0.0997*	
	30 min	Cu-O	1.94 ± 0.01	1.56 ± 0.23	0.0431*
Cu-Cu		2.53 ± 0.002	6.95 ± 0.26	0.0853*	
Cu-Cu		3.63 ± 0.02	5.74 ± 1.6	0.0906*	
Cu-Cu		4.44 ± 0.008	9.91 ± 1.3	0.0885*	
Cu-Cu		4.95 ± 0.01	3.7 ± 0.64	0.0344*	
Cu-Cu		3.47 ± 0.02	5.61 ± 1.7	0.0997*	

Numbers marked with * are fixed according to the information in the cif file.

CuO NS film as-prepared

	Shell	R / Å	N	σ	R _f
50 min	Cu-O	1.94 ± 0.02	0.975 ± 0.22	0.0431*	9.01
	Cu-Cu	2.53 ± 0.01	8.23 ± 0.26	0.0853*	
	Cu-Cu	3.61 ± 0.02	7.72 ± 1.6	0.0906*	
	Cu-Cu	4.44 ± 0.01	11.9 ± 1.3	0.0885*	
	Cu-Cu	4.95 ± 0.01	4.93 ± 0.65	0.0344*	
	Cu-Cu	3.45 ± 0.02	6.98 ± 1.8	0.0997*	
80 min	Cu-O	1.95 ± 0.03	0.656 ± 0.23	0.0431*	8.438
	Cu-Cu	2.52 ± 0.004	9.23 ± 0.26	0.0853*	
	Cu-Cu	3.64 ± 0.02	8.44 ± 1.6	0.0906*	
	Cu-Cu	4.44 ± 0.01	14.4 ± 1.3	0.0885*	
	Cu-Cu	4.96 ± 0.01	5.63 ± 0.64	0.0344*	
	Cu-Cu	3.46 ± 0.02	6.88 ± 1.7	0.0997*	
90 min	Cu-Cu	2.523 ± 0.004	9.74 ± 0.25	0.0853*	12.63
	Cu-Cu	3.58 ± 0.02	2.8 ± 0.7	0.0906*	
	Cu-Cu	4.44 ± 0.008	14.9 ± 1.2	0.0885*	
	Cu-Cu	4.96 ± 0.009	5.95 ± 0.62	0.0344*	
	120 min	Cu-Cu	2.53 ± 0.004	10.1 ± 0.25	
Cu-Cu	3.61 ± 0.01	3.91 ± 0.27	0.0906*		
Cu-Cu	4.44 ± 0.01	14.8 ± 1.2	0.0885*		
Cu-Cu	4.95 ± 0.01	6.54 ± 0.62	0.0344*		

Only when the Cu metal content is $\leq 90\%$ it is reasonable to include CuO distances (marked red)

Reference materials					
	Shell	R / Å	N	σ	R_f
CuO powder	Cu-O	1.95 ± 0.01	4*	0.0614	9.07
	Cu-O	2.74 ± 0.01	2*	0.0997	
	Cu-Cu	2.88 ± 0.02	4*	0.081	
	Cu-Cu	3.02 ± 0.01	4*	0.0717	
	Cu-Cu	3.16 ± 0.02	2*	0.0317	
	Cu-Cu	3.38 ± 0.03	2*	0.99	
	Cu-Cu	3.88 ± 0.03	2*	0.0998	
	Cu-Cu	4.79 ± 0.01	5*	0.0747	
	Cu-Cu	4.97 ± 0.01	4*	0.0333	
Cu(OH)₂ powder	Cu-O	1.97 ± 0.01	2.2 ± 0.18	0.0317*	10.2
	Cu-O	1.89 ± 0.02	2.2 ± 0.17	0.0596*	
	Cu-O	2.89 ± 0.02	2.11 ± 0.27	0.0987*	
	Cu-Cu	2.93 ± 0.03	2.08 ± 0.15	0.0316*	
	Cu-Cu	3.33 ± 0.03	3.68 ± 0.16	0.0987*	
Cu metal	Cu-Cu	2.53 ± 0.001	12 ± 0.24	0.0853*	10.87
	Cu-Cu	3.60 ± 0.01	5.57 ± 0.21	0.0906*	
	Cu-Cu	4.44 ± 0.004	21 ± 1.2	0.0885*	
	Cu-Cu	4.96 ± 0.004	8.65 ± 0.59	0.0344*	

Simulation approach: first I fixed the coordination number N to the expected value (cif file) and calculated the distances R for each shell, and the Debye Waller. Then, the Debye Waller factor was fixed to obtained values above and N was calculated, highly similar, but slightly lower R_f factor (better fit quality).

A4. Supplementary Information to Chapter 7

Achieving high C₂H₄ Evolution at industrial current densities on CuO_x nanosheet derived gas diffusion electrode

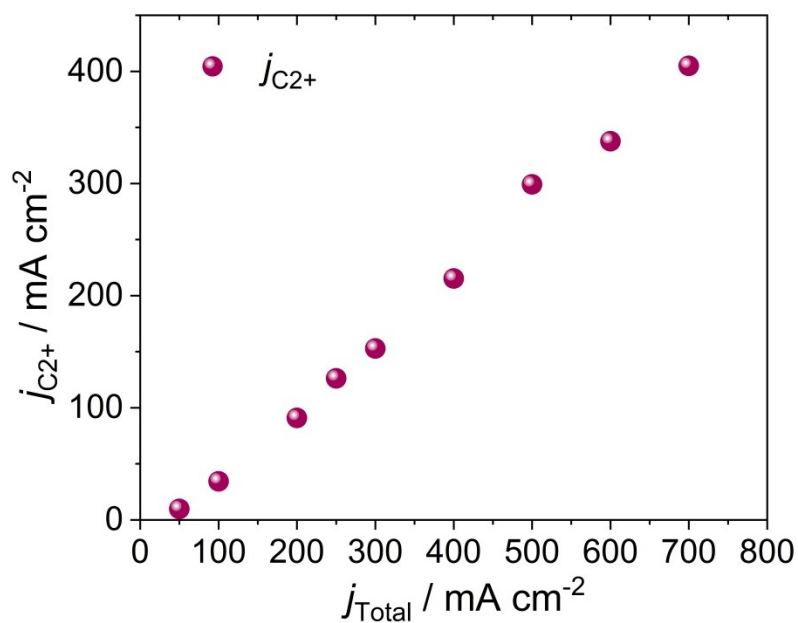


Figure A4.1 The partial current density of C₂₊ products as a function of applied geometric current density for CuO_x NS in 1 M KHCO₃.

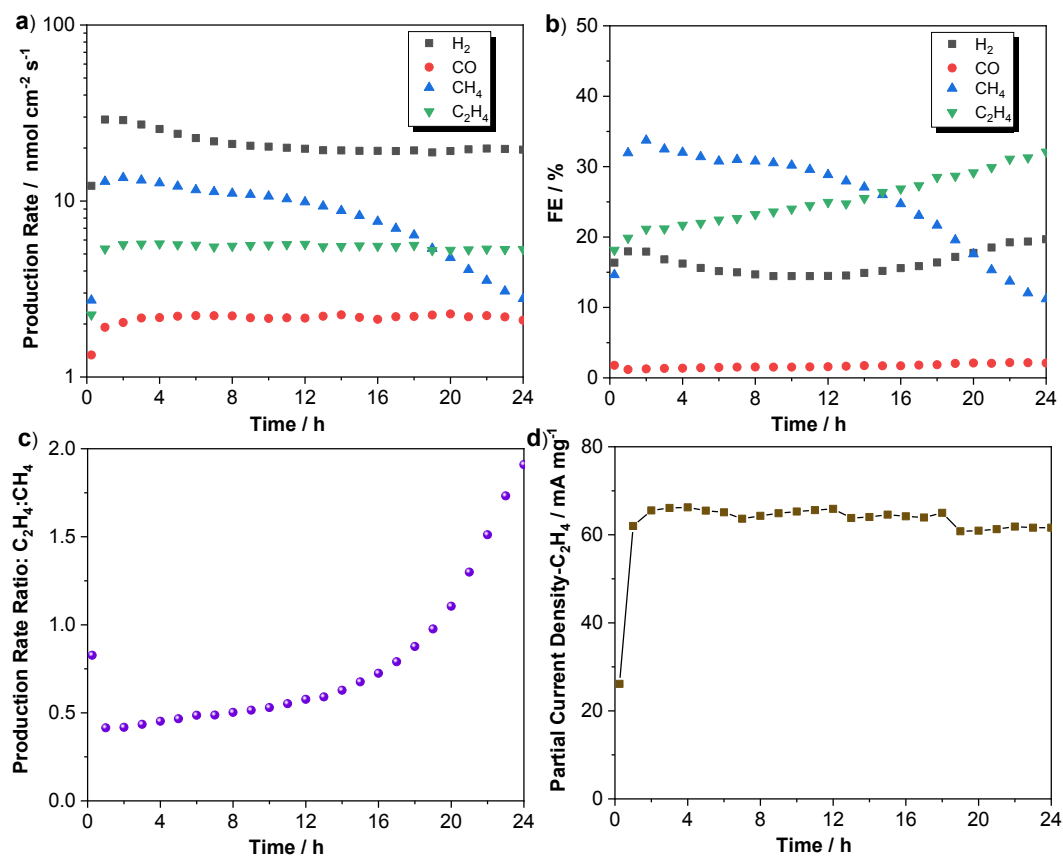


Figure A4.2 Chronoamperometric performance stability of the CO₂ reduction reaction on CuO_x NS in CO₂-saturated 0.1 M KHCO₃ at -1.0 V_{RHE}, performed in an H-cell configuration. a) Absolute product formation rates of major gaseous products over 24 h. b) Faradaic efficiencies of major gaseous products. c) The experimental results of C₂H₄/CH₄ product selectivity over 24 h. d) Partial current density of C₂H₄ with time.

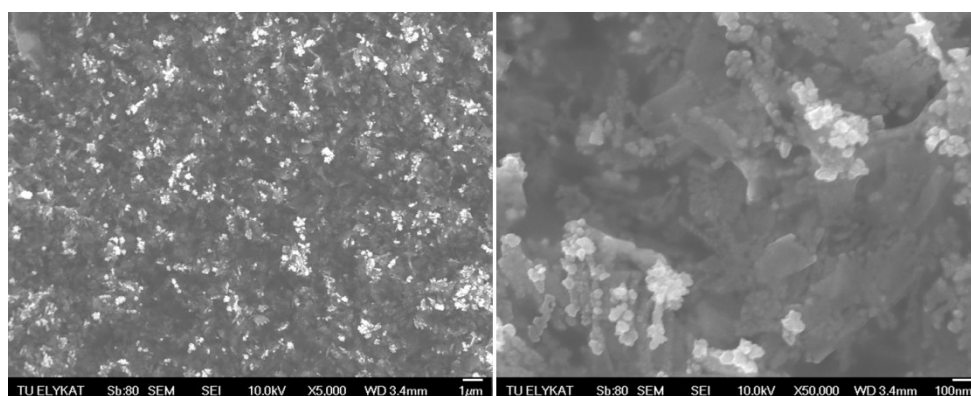


Figure A4.3 SEM image of as-prepared CuO_x catalyst after H-cell test.

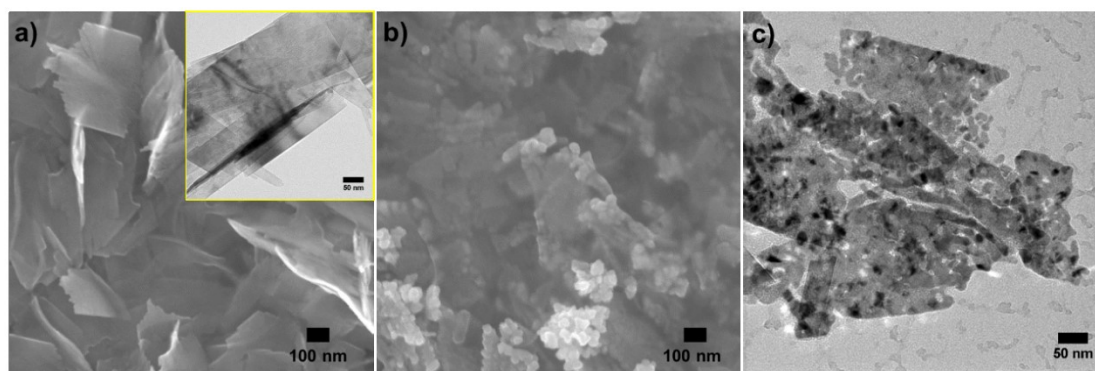


Figure A4.4 Morphology evolution of CuO_x NS. a) SEM image of as-prepared CuO_x NS/glassy carbon electrode. Insert: TEM image of CuO_x NS. b) SEM image of CuO_x NS in CO_2 -saturated 0.1 M KHCO_3 after 1-hour reaction at $-1.0 V_{\text{RHE}}$. c) TEM image of CuO_x NS in N_2 -saturated 0.1 M $\text{Na}_2\text{HPO}_4/\text{NaH}_2\text{PO}_4$ (pH=6.9) after 15 min at $-1.0 V_{\text{RHE}}$.

Table of figures and schemes

Figure 1.1 Total global renewable energy capacity from Hydropower and marine (orange), Wind (green), Solar (violet), Bioenergy (yellow), Geothermal (blue) sources. Data taken from ref⁸. Copyright International Renewable Energy Agency.....	1
Figure 1.2 General scheme of a typical electrolyzer for CO₂RR.....	3
Figure 1.3 Classification of various metal depending on formation of major products in electrochemical CO₂ reduction. a) Periodic table and faradaic efficiency of major product from experimental data by Hori. H₂ (red), CO (blue), formate (yellow), hydrocarbon (green) b) The experimental product classification of H₂, CO, and HCOOH by the $\Delta E_{H^*} - \Delta E_{COOH^*}$ and the ΔE_{H^*}. c) Faradaic efficiency of CO₂ reduction reaction by ΔE_{H^*}. a-c) Modified and reproduced from ref⁵¹ with permission. Copyright 2018, John Wiley and Sons.....	4
Figure 1.4 Possible C1 species for C-C coupling.....	5
Figure 1.5 a) Tuning the product distribution of CO₂ electroreduction on OD-Cu foam catalysts. b) Optimizing C-C coupling on oxide-derived copper. c) Effects of CO* coverage on the selective formation of ethylene. d) Nature and distribution of stable subsurface oxygen in OD-Cu. a) to d) are adapted from ref^{97, 102, 75 and 112}, respectively, with the permission, copyright American Chemical Society.	7
Figure 2.1 Schematic overview of scientific questions and goals dealt with in the course of this work.	9
Figure 3.1 lists the interaction between electrons and samples used for different techniques.....	17
Figure 3.2 Schematic illustration of the Bragg equation.....	18
Figure 3.3 Bohr model of an atom. When energy is absorbed by an atom, electron jumps from its ground state orbital to an orbital with higher energy level. For the stabilizing, the atom may decay back to a lower energy state by emitting a photon, $h\nu$.	21
Figure 3.4 Schematic (a) and photograph (b) of H-type two compartments cell divided by a polymer membrane.	22
Figure 3.5 Geometry defining of the incident beam and scattered beam with scattering vector \vec{q}.	27
Figure 3.6. a) Schematic illustration of the <i>in situ</i> WAXS setup under electrochemical condition using at a synchrotron facility, showing the incident and scattered X-rays, the 2D detector and the grazing incidence cell. The side view (b) and the top view (c) of the test station at the European Synchrotron Radiation Facility (ESRF).	29
Figure 3.7 a) Photograph and dimension of the electrochemistry chips with enlarged big E-chip, in comparison to 1 euro cent. b) Chip design and three-electrode system applied on	

the big E-chip, showing the glassy carbon working electrode in the center, surrounded by the Pt reference electrode (grey) and the Pt counter electrode (light grey). c) Assembling of the liquid E Chem holder with gasket, big/small E-chips and lid. d) Side view of the chip with the corresponding bottom chip and the electrolyte layer between the chips. e) *ex situ* cell with same chip assemble, flow mode and electrochemical connection. f) Gamry potentiostat for the liquid E Chem holder and *ex situ* cell. Images are partly adopted from “Workflow & Training Poseidon Select Version 1.2; Copyright 2017, Protochips, Inc.” with permission from Protochips.30

Figure 3.8 Schematic DEMS setup - custom-made TU Berlin electrochemical capillary DEMS flow cell.33

Figure 3.9 Schematic view and photography of feed gas control system at DEMS setup - saturation of electrolyte in the flow stream.33

Figure 3.10 A typical mass spectrum of ethylene gas directly dissolved in 0.1 M KHCO₃ and measured at DEMS setup.35

Figure 3.11 Photograph of *operando* XAS test station at Bessy.40

Figure 4.1 Physiochemical characterization of as-prepared CuO_x NPs.45

Figure 4.2 Catalytic activity represented by liner sweep voltammograms taken at 5 mV/s in CO₂-saturated 0.1 M KHCO₃ for 4 μg cm⁻², 15 μg cm⁻², 31 μg cm⁻² CuO_x NPs areal densities, catalyst layers were supported on glassy carbon.46

Figure 4.3 Catalyst mass-normalized absolute product formation rates of major gaseous products as a function of applied electrode potentials during CO₂ electroreduction in CO₂-saturated 0.1 M KHCO₃ at CuO_x nanoparticle catalyst areal densities.48

Figure 4.4 Faradaic efficiency for each product as a function of areal density at various applied overpotentials. Faradaic efficiency of CO₂ electrochemical reduction over a) 4 μg cm⁻², b) 15 μg cm⁻², c) 31 μg cm⁻². d) The Faradaic efficiency ratios of C₂H₄/CH₄ versus overpotential for the different areal densities.49

Figure 4.5 a) Chronoamperometric performance stability of the CO₂ reduction reaction on CuO_x NPs in CO₂-saturated 0.1 M KHCO₃ at -1.0 V_{RHE}. b) Partial current densities of CO, CH₄, C₂H₄. c) Absolute product formation rates of gaseous products over time. d) The consumption ratio of *CO for CO, CH₄, C₂H₄, respectively. Catalyst areal density: 31 μg cm⁻².50

Figure 4.6 a) TEM image of CuO_x nanoparticles after the chronoamperometric stability test at -1.0 V_{RHE} from Figure 4.5. b) The mean particle size after 400 min significantly increased compared to Figure 4.1a. Catalyst areal density: 31 μg cm⁻².53

Scheme 4.1 The favored pathway for *CO in low/high areal NP densities condition. In low areal particle density, *CO tend to leave as CO(g); while in high areal NP density, the

desorbed CO(g) molecules are more likely to re-adsorb on the surface of nearby Cu particles.....	52
Figure 5.1 Morphological, structural, elemental and physical characterizations of CuO_x NPs synthesized in this study.	59
Figure 5.2 Catalytic performance detected by on-line GC in H-cell.	63
Figure 5.3 The possible carbon origins in pure feeds and co-feed during our DEMS experiments. In co-feed condition, carbon origins could go through “CO₂-CO₂” combination, “CO-CO” combination and/or crossed “CO₂-CO” combination pathway to C₂H₄.	65
Figure 5.4 Quantitative deconvolution of relative contributions of competing CO-CO dimerization reaction pathways to ethylene using a novel <i>operando</i> DEMS capillary flow cell system. Differential electrochemical mass spectrometry (DEMS) sweep data obtained during CO_x reduction a CuO_x NP catalysts (supported on a flat 0.785 cm² glassy carbon electrode) using CO₂/CO co-feeds, pure CO₂ and pure CO feeds during a cyclic voltammetric scan at 5mV s⁻¹ and electrolyte flow of 5 μL s⁻¹.	67
Figure 5.5 Mechanistic hypotheses of enhanced ethylene production under CO₂/CO reactant co-feeds.	71
Figure 5.6 The realization of enhanced ethylene production using internal CO₂/CO “self co-feeding” using non-metallic/metallic tandem catalyst design.	73
Figure 5.7 The realization of enhanced ethylene/methane production using internal CO₂/CO “self co-feeding” using metallic/metallic tandem catalyst design. a) The catalyst is combining Ag material as a local CO-producer and CuO_x NPs on glassy carbon electrode. b) C₂H₄ and CH₄ production rate with CuO_x-NiNC catalyst for CO₂RR at the various component and fixed overpotentials. Error bars are given as standard error of mean.	74
Figure 6.1 Morphological, structural characterizations of sheet-like CuO_x nanoparticles synthesized in this study.	80
Figure 6.2 Electrochemical Performance of CO₂RR with as-Prepared CuO_x NS in H-cell configuration.	82
Figure 6.3 Catalyst evolution during CO₂RR characterized by <i>operando</i> XAS.	84
Figure 6.4 Catalyst shape evolution detected by <i>in situ</i> WAXS.	86
Figure 6.5 Products formation and onset potential shift along electroreduction of CuO_x NS catalyst.	87
Figure 7.1 Electrochemical characterization in micro Flow-Cell configuration.	92
Figure 7.2 SEM image of CuO_x NS GDE after CO₂ electrolysis.	93
Figure 7.3 a) Gaseous products efficiencies with 300 mA cm⁻² in CO₂ electrolyzer flow cell.	94

Figure 7.4 Quasi <i>in situ</i> demonstration of dendrites growth after reduction of CuO_x NS catalyst in E Chem holder.....	95
Figure 8.1 Graphical summary of topics and issues discussed and investigated in first part of work, including areal density control, mechanistic co-feed study, and tandem catalyst. (Reprinted with permission from The John Wiley and Sons).	98
Figure 8.2 Graphical summary of topics and issues discussed and investigated in second part of this work, including shaped CuO_x nanoparticles synthesis, characterization, H-cell tests, combination of <i>operando</i> studies, and flow cell test at industrial level.	100
Figure A1.1 a) b) Representative TEM images of CuO_x nanoparticles after 7 days in hexane. The inset shows the size distribution of CuO_x nanoparticles.	113
Figure A1.2 a) Diffraction pattern of as-prepared CuO_x NPs. Also indicated are diffraction patterns of metallic Cu (red, PDF#98-000-0172), CuO (blue, PDF#01-078-0428), and Cu₂O (green, PDF#98-000-0186).	113
Figure A1.3 The crystal structures of a) metallic Cu, b) cubic-Cu₂O (cuprite), c) monoclinic-CuO (Tenorite). Color legend: blue spheres, Cu; red sphere, O.	114
Figure A1.4 The total Faradaic efficiencies of gaseous products as a function of areal density at various applied overpotentials. Faradaic efficiencies of CO₂RR and HER over a) 4 μg cm⁻², b) 15 μg cm⁻², c) 31 μg cm⁻².	114
Figure A1.5 The Faradaic efficiencies for all detected products on CuO_x NPs after 400 min with the particle areal density of 31 μg cm⁻² at -1.0V_{RHE}.	115
Figure A1.6 a) Total Faradaic efficiency for gaseous products as a function of areal particle density. b) Trends in C₂H₄/CH₄ production ratio at varying catalyst areal densities at -1.01 V_{RHE} applied electrode potential. Potentials are IR corrected.	115
Figure A1.7 Electrochemical CO₂ reduction activity (left axis of ordinates) and selectivity (right axis of ordinates) of glassy carbon as blank at various overpotentials. The amount of H₂ at -0.66 V_{RHE} is not detectable (under TCD detecting limitation).	116
Figure A2.1 Time-dependent absolute product formation rates on H₂.	117
Figure A2.2 Liquid products analysis after 4-hour measurements in various feeds conditions. Absolute product formation rates of detected liquid products on CuO_x NPs with various CO₂/CO ratios.	118
Figure A2.3 Formate analysis after 4-hour measurements in various feeds conditions.	118
Figure A2.4 The potential-dependent tests of CORR, CO₂RR and co-feed reduction (CO₂: CO 1:1).	119
Figure A2.5 XRD profiles of as-prepared working electrodes tested before and after electrochemical reductions.	120

Figure A2.6 SEM images of as-prepared working electrodes after electrochemical reductions.	121
Figure A2.7 High angle annular dark field (HADDF) images and EDX (Energy dispersive X-ray spectroscopy) line scan of the CuO_x NPs after co-feed (1:1) reduction.....	121
Figure A2.8 Investigation of pure feed reductions of CORR and CO2RR.	122
Figure A2.9 The ratios of reaction between the three mechanisms. The ratio of reaction between the three mechanisms on a) CO-CO, CO₂-CO₂, and b) CO₂-CO, with respective potential range for integration at 0.05 V from cathodic to anodic sweep of potentials.	123
Figure A2.10 Decomposition of the three pathways calculated by the co-feed system of a mixture of carbon isotopes.....	123
Figure A2.11 Differential electrochemical mass spectrometry data obtained on 0.785 cm² large glassy carbon electrode drop-coated with CuO_x NPs catalysts and using pure CO, pure CO₂ and CO₂-CO co-feed.	124
Figure A2.12 SEM images of as-prepared the bifunctional hybrid catalyst. SEM images of CuO_x NPs (50 μg cm⁻²)-NiNC (1:4) tandem catalyst with carbon paper as working electrode a) SEI mode; b) COMPO mode.	125
Figure A2.13 Catalytic performance of the tandem CuO_x-NiNC catalysts detected by on-line GC in H-cell. Absolute product formation rates on a) CO and b) CH₄ with different catalyst loading variation at -0.84 V_{RHE} and -0.9 V_{RHE}.	125
Figure A2.14 The long stability test of tandem CuO_x-Ag (1:3) catalyst at constant electrode potential of -1.0 V_{RHE} in CO₂-saturated 0.1 M KHCO₃.	126
Figure A3.1 SEM images of Cu(OH)₂ intermediate formed during synthesis process.	127
Figure A3.2 a) Cross-section TEM images of as-prepared CuO_x NS and b) corresponding intensity of SAED intensity.	127
Figure A3.3 Crystal structure of monoclinic CuO with indexing plane.	128
Figure A3.4 a) Partial contour plot of CuO_x NS. b) Azimuthally integrated line profiles of as-prepared CuO_x NS.	128
Figure A3.5 Faradaic efficiencies of main products distribution after CO2RR in H-cell design.	129
Figure A3.6 a) Chronoamperometric performance stability of the CO₂ reduction reaction on CuO_x NS in CO₂-saturated 0.1 M KHCO₃ at -0.84 V_{RHE}. SEM image of as-prepared CuO_x catalyst on GC electrode (100 μg cm⁻²) before b) and c) after 20-hour electrolysis.	129

Figure A3.7 a) Chronoamperometric performance stability of the CO₂ reduction reaction on CuO_x NS in CO₂-saturated 0.1 M KHCO₃ at -0.76 V_{RHE}. Production rates b) and Faradaic efficiencies c) of main gaseous products over 1200 min.....	130
Figure A3.8 SEM image of 1-h Chronoamperometric performance of the CO₂ reduction reaction on CuO_x NS in CO₂-saturated 0.1M KHCO₃ at -0.84 V_{RHE}.....	130
Figure A3.9 Comparison of XANES at the Cu K-edge of references powders CuO, Cu(OH)₂ and the CuO_x NS film in the dry state, and at OCP in 0.1 M KHCO₃ at pH 6.8.....	131
Figure A3.10 a) FT of k³ weighted EXAFS a) and b) EXAFS at the Cu K-edge of Cu metal foil, Cu(OH)₂ powder, CuO powder, and the CuO_x NS film at OCP in 0.1 M KHCO₃ at pH 6.8.	131
Figure A3.11. a) FT of k³ weighted EXAFS at the Cu K-edge of the CuO_x NS film at OCP in 0.1 M KHCO₃ at pH 6.8 and during 130 min CO₂RR at -0.84 V_{RHE}. b) EXAFS (k³ weighted) at the Cu K-edge of the CuO_x NS film at OCP in 0.1 M KHCO₃ at pH 6.8 and during 130 min CO₂RR at -0.84 VRHE.	132
Figure A3.12 EXAFS distances of the first Cu-O coordination sphere and the first intermetallic Cu-Cu shell.	133
Figure A4.1 The partial current density of C₂₊ products as a function of applied geometric current density for CuO_x NS in in 1 M KHCO₃.	137
Figure A4.2 Chronoamperometric performance stability of the CO₂ reduction reaction on CuO_x NS in CO₂-saturated 0.1M KHCO₃ at -1.0 V_{RHE}, performed in an H-cell configuration.	138
Figure A4.3 SEM image of as-prepared CuO_x catalyst after H-cell test.	138
Figure A4.4 Morphology evolution of CuO_x NS.....	139

Table of tables

Table 3.1 Overview of different materials used in this work with the corresponding chapters in which their characterization is discussed.	14
Table 3.2 Overview of Methods for physicochemical characterization used in this thesis with reference to the sections in which they are described.....	16
Table 3.3 Summary of the detectable products in the H₂O/CO₂RR electrolysis and the corresponding detection methods.	24
Table 3.4 All main possible fragments of ethylene including CO and CO₂ species.	36
Table 3.5 Resume of the main ethylene fragments used for the DEMS based deconvolution of the contribution of each reaction pathways with relative intensity (r.i.) and fragment assignments (Assgn.) of the three *CO dimerization mechanisms resulting in ethylene formation (C₂H₄, ¹³CH₂CH₂ and ¹³CH₂¹³CH₂). The three mechanisms are denoted as “CO₂-CO₂” if both carbon atoms of ethylene derive from ¹²CO₂, ”CO₂-CO” in case of mixed origin and “CO-CO” if both carbon atoms derive from ¹³CO.	37
Table 5.1 Gas flow control of various feeds and their relevant ratios of dissolved CO_x species according to Henry’s law.	61
Table 5.2 Electrolyte flow control of various feeds and their relevant ratios of dissolved CO_x species in DEMS setup.	61
Table 5.3 Comparison of DEMS-derived kinetic reaction parameters of the three CO dimerization pathways to ethylene depending on the chemical origin of the CO. Cross coupling (CO₂-CO) pathway: The dimerizing CO intermediates derive from CO₂ and CO; (CO₂-CO₂) pathway and (CO-CO) pathway: CO originated only from CO₂ or CO, respectively; i_{MS} (mA cm⁻² s⁻¹) is the respective maximum C₂H₃⁺ ion current, Q_{MS} (As) is the DEMS charge under the deconvoluted C₂H₃⁺ ion current sweeps under CO₂/CO co-feeding in cathodic and anodic scan direction. “Tafel” denotes the experimentally apparent (ion mass current derived) Tafel slopes (V_{RHE}dec⁻¹), while E (in units of V_{RHE}) is the experimental onset potential of ethylene formation.	70
Table A2.1 Liquid products of tandem CuO_x-NiNC catalysts during CO₂RR after 90 min at fixed overpotential.....	126
Table A3.1 Cu K-edge simulation parameters of the FT-EXAFS oscillations of as-prepared CuO_x NS film.	134

List of Abbreviations

CO2RR	(Electrochemical) CO ₂ reduction reaction	HER	Hydrogen reduction reaction
atm	atmospheres	XRD	X-ray diffraction
M-N-C	Metal-Nitrogen-Carbon	OER	Oxygen evolution reaction
OD-Cu	Oxide-derived copper	ICP-OES	Inductively Coupled Plasma Optical Emission Spectrometry
CE	Counter electrode	WE	Working electrode
RE	Reference electrode	NHE	Normal hydrogen electrode
RHE	Reversible hydrogen electrode	LSV	Linear sweep voltammetry
CA	Chronoamperometry	GDE / L	Gas diffusion electrode / layer
DFT	Density functional theory	MEA	Membrane electrode assembly
h	hours	min	minutes
DEMS	Differential electrochemical mass spectrometry	WAXS	Wide-angle X-ray scattering
AW	Acid washing	HT	Heat treating
EDX	Energy dispersive X-ray spectroscopy	PEIS	Potentiostatic electrochemical impedance spectroscopy
TEM	Transmission electron microscopy	HRTEM	High resolution TEM
PTFE	Polytetrafluoroethene	XAS	X-ray absorption spectroscopy
OCP	Open circuit potential	EXAFS	Extended X-ray absorption fine structure
GC	Gas chromatograph / Glassy carbon	HAADF	High-angle annular dark field
PCET	Proton coupled electron transfer	HE-XRD	High-energy XRD
HPLC	High performance liquid chromatograph	MFC	Micro flow cell
SEM	Scanning electron microscopy	RT	Room temperature
iR	Current times resistance (ohmic drop)	FE	Faradaic efficiency
TCD	Thermal conductivity detector	FID	Flame ionization detector

ER	Eley-Rideal	SAED	Selected area electron diffraction
XANES	X-ray absorption near edge spectra	GI-WAXS	Grazing incidence wide-angle X-ray scattering
NPs	Nanoparticles	NS	Nanosheet
GDE	Micro-flow-cell	PTFE	Polytetrafluorethylen
Echem	Electrochemistry		

List of Chemicals

Name	Acronym	Purity/Concentration	Supplier
Ultra-pure water	Milli-Q water	16.8 M Ω cm	-
Methanol	MeOH	anhydrous, 99.9 %	Alfa Aesar
Ethanol	EtOH	100 %	VWR Chemicals
Isopropanol	iPrOH	100 %	VWR Chemicals
n-Propanol	nPrOH	100 %	VWR Chemicals
Nafion	-	5 wt%	Sigma Aldrich
Nafion membrane	-	-	Sigma Aldrich
Selemion membrane	-	-	AGC Eng. Co.
Ketjen EC 600JD	-	-	AzkoNobel
Perchloric acid	HClO ₄	70 % conc., 99.999 % trace metal bases	Sigma Aldrich
Sulfuric acid	H ₂ SO ₄	95.0 %	VWR Chemicals
Hydrochloric acid	HCl	37.0 %	VWR Chemicals
Nitric acid	HNO ₃	69.0 %	Merck
Phosphoric acid	H ₃ PO ₄	85 wt%	Sigma Aldrich
Potassium hydroxide	KOH	99.99%	Sigma Aldrich
Potassium bicarbonate	KHCO ₃	99.5%	Sigma Aldrich
Potassium dibasic phosphate	K ₂ HPO ₄	99.95%	Sigma Aldrich
Potassium monobasic phosphate	KH ₂ PO ₄	99.95%	Sigma Aldrich
Ammonium peroxodisulfate	(NH ₄) ₂ S ₂ O ₈	>98%	Merck
Formic acid	HCOOH	>95%	Sigma Aldrich
Formaldehyde	CH ₂ O	37wt %	Merck
Carbon dioxide	CO ₂	99.999 %	Air Liquide
Hydrogen	H ₂	99.999 %	Air Liquide
Carbon monoxide	CO	99.997 %	Air Liquide
Nitrogen	N ₂	99.999 %	Air Liquide

Oxygen	O ₂	99.998 %	Air Liquide
Argon	Ar	99.999 %	Air Liquide
Helium	He	99.999 %	Air Liquide
Trioctylphosphine oxide	TOPO	90%	Sigma Aldrich
Borane tert-butylamine complex	TBAB	97%	Sigma Aldrich
Oleylamine	OA	90%	Sigma Aldrich
N, N-dimethylformamide	DMF	99%	Sigma Aldrich
Cuprous Bromide	CuBr	99%	Sigma Aldrich
Cupric Acetate	Cu(Ac) ₂	99%	Sigma Aldrich

List of Publications during Ph.D. Study

- Catalyst Particle Density Controls Hydrocarbon Product Selectivity in CO₂ Electroreduction on CuO_x. X. Wang, A. S. Varela, A. Bergmann, S. Kuehl, P. Strasser. *ChemSusChem*, 2017, 10, 4642–4649.
- Mechanistic reaction pathways of enhanced ethylene yields during electroreduction of CO₂–CO co-feeds on Cu and Cu-tandem electrocatalysts X. Wang, J. Araújo, W. Ju, A. Bagger, H. Schmies, S. Kuehl, J. Rossmeisl, P. Strasser. *Nat. Nanotechnol.*, 2019, 14, 1063-1070.
- Sheet-like Copper Oxides with Stable and Selective Ethylene Production for Direct CO₂ Electroreduction from H-cell to Flow Cell. X. Wang, K. Klingan, T. Möller, J. Araújo, S. Jiang, H. Dau, P. Strasser. In Preparation for submission.
- Tracking Copper Oxide Dendrite Catalyst Growth during CO₂ Electroreduction in a Liquid Electrochemical TEM Cell. X. Wang, T. Möller, M. Klingenhof, S. Kuehl, P. Strasser. In Preparation for submission.
- Efficient CO₂ to CO Electrolysis on Solid Ni-N-C Catalysts at Industrial Current Densities, T. Moeller, W. Ju, A. Bagger, X. Wang, F. Luo, T. N. Thanh, A. Varela, J. Rossmeisl, P. Strasser, *Energy and Environmental Science*, 2019, 12,640-647.
- Alloy Nanocatalysts for the Electrochemical Oxygen Reduction (ORR) and the Direct Electrochemical Carbon Dioxide Reduction Reaction (CO₂RR), C. Kim, F. Dionigi, V. Beermann, X. Wang, T. Möller, P. Strasser, *Adv. Mater.* 2018, 1805617.